Drag reduction in a turbulent channel with bars via a spanwise oscillating pressure gradient

By

Gianluca Pironti

A thesis submitted in partial fulfilment of the requirements
for the degree of Doctor of Philosophy

University of Sheffield
Department of Mechanical Engineering

2020

Contents

List of Tables

List of Figures

Abstract

An active technique is employed to control flow separation and reduce drag in a turbulent channel with bars located on each wall. The control is enforced via an oscillating spanwise pressure gradient which creates a statistical periodic flow transverse to the streamwise flow direction.

A maximum total drag reduction of 12% was obtained, due to both pressure and skin-friction drag reductions. The distinctive finding of this study is the simultaneous decrease of both pressure and skin-friction in contrast with vortex generators and jets which increase fluid mixing and skin-friction to reduce pressure drag.

The form drag relation with the pressure around the bar is analyzed and it is found that the pressure drag reduction is due to a decrease of the Reynolds stress and pressure along the dividing streamline delimiting the separation area. The skin-friction drag reduction is caused by the decrease of the shear stress along the cavity.

The power spent for the actuation is computed and compared with drag reduction. An approximate formula, obtained by solving a simplified laminar flow, is developed which relates the power spent with the control parameters.

The mechanism of drag reduction is discovered via an integral form of the streamwise momentum conservation and it is proved that the total drag is reduced because of the effect of the control on the Reynolds stress.

Acknowledgments

I wish to thank my supervisor Dr. Pierre Ricco to introduce me to the research world and to give me the opportunity to begin my PhD. Pierre is what a true scientist should be. His passion and curiosity has been a source of inspiration and admiration for me.

I wish also to thank the people at the Institute of High Performance Computing in Singapore and in particular my supervisor Dr. Vinh-Tan Nguyen for the constant help and suggestions he gave me during my time in Singapore.

I presented part of this work at The European Drag Reduction and Flow control Meeting (EDRFCM) Bad Herrenalb, Germany in March 2019.

I thank my family and my friends in Singapore and Sheffield for supporting me during this long journey and encouraging me to not give up and realize my dream. This work is dedicated to my father for believing in me.

Nomenclature

Δt	Time step
$\int_{V_F} \cdot \, \mathrm{d}V$	Integral on the fluid volume
$\mathbf{i}$, $\mathbf{j}$, $\mathbf{k}$	Unit vectors on x, y and z direction
$\mathbf{U}$	Velocity vector
$\mathbf{n}$	Unit vector normal to the surface
$\mathcal{P}(\%)$	Percentage of Power to control the flow
$\mathcal{P}_{net}(\%)$	Percentage of net power saved
$\mathcal{P}_{l}(\%)$	Percentage of laminar power spent
$\mathcal{R}(\%)$	Percentage of drag reduction
$\mathcal{R}C_f(\%)$	Percentage variation of friction drag
$\mathcal{R}C_{ca}(\%)$	Percentage variation of friction drag at the bar cavity
$\mathcal{R}C_{cr}(\%)$	Percentage variation of friction drag at the bar crest
$\mathcal{R}C_p(\%)$	Percentage variation of pressure drag
E_x	Energy to drive the flow along x
E_z	Energy to drive the flow along z
P_x	Energy to drive the flow along z
P_z	Energy to drive the flow along z

Π_x	Streamwise pressure gradient
Π_z	Spanwise pressure gradient
A, T	Amplitude and period of Π_z
$C_{f,ca}$, $C_{f,cr}$	Skin-friction coefficient at the cavity and crest of the bar
C_p, C_f	Time averaged pressure and skin-friction coefficients
$C_p(t)$, $C_f(t)$	Pressure drag and skin-friction coefficients
L_x, L_y, L_z	Sizes of the computational domain along x, y and z
N_{bars}	Number of bars on one wall
p	Pressure
t	Time
u, v, w	Velocity components along the streamwise, vertical and normal directions
U_b	Streamwise bulk velocity
u_t, v_t, w_t	turbulent velocity fluctuations along the streamwise, vertical and normal directions
V_F	Fluid volume
W_b	Spanwise bulk velocity
x, y, z	Coordinates on streamwise, normal and spanwise direction
Δp_i	Difference of pressures at vertical sides of the bars

Chapter 1

Introduction

Reducing turbulent drag is a topic of practical interest because of economical and environmental reasons. Modern transportation systems as aircrafts or trains move at fast velocities and experience huge resistances which need to be overcome. An enormous quantity of fuel is required therefore decreasing the drag would cause economical savings and decrease pollutant emissions. Walsh et al. (1989) estimated that a 10% reduction of skin-friction drag of commercial airplanes could generate savings for 250 million of dollars per year. Offshore platforms supply gas or oil through many kilometers long pipelines and requires a considerable amount of pumping power. A several percent of drag reduction would imply lower amount of energy necessary to move the fluid and a better efficiency of the system.

A fluid can be considered incompressible when any pressure variation results in negligible density modifications. This occurs when characteristic velocities are small compared to the speed of propagation of the sound and the global drag is composed of a viscous and a pressure contribution. Skin-friction is the direct consequence of the viscosity and the shear stress that slows down the fluid nearby a solid wall. Pressure drag is mainly related to the shape of a body and due to the component of the pressure force along the main direction of the flow. The relative importance of the two contributions depends on the specific problem analyzed. For instance, a golf ball is mostly affected by pressure drag while for a wing, at low angles of attack, skin-friction represents the highest percentage of the whole resistance.

Control methods can be classified as active and passive, depending on whether energy is supplied or not to the physical system. Active controllers can be deactivated when their action is no longer required, but a weight penalty is introduced due to the actuators used. Active methods are also prone to damage and often require expensive maintenance. A clear advantage of active controllers is the large beneficial flow modifications that can be achieved. Passive methods often involve a geometrical modification of the surface, have the clear benefit of not requiring external power supply, but the small wall alterations may necessitate regular repairment.

Developing a system which, at the same time, guarantees a reasonable amount of drag reduction and low costs for production, maintenance and energy consumption is of paramount importance to achieve economical advantages.

1.1 Turbulent skin-friction reduction methods

A flow is turbulent when the inertial forces are several order of magnitude higher than viscous forces and large amounts of fluid are constantly mixed in a random fashion. Random fluctuations happen and the fields can only be analyzed from a statistical point of view. Conversely, a laminar flow takes place when the effect of viscosity is greater than inertial effects and the fluid moves in laminae in an ordered manner.

Skin-friction is due to the integral of the shear stress along the solid surface of a body immersed in a fluid. The shear stress experienced by a body in a laminar flow is much smaller than the one in a turbulent flow due to the Reynolds stresses and their effect on the averaged velocity field. Therefore, any technique to control friction drag should nullify (laminarization) or at least reduce the Reynolds stresses.

1.1.1 Active methods

Spanwise wall oscillation

Jung et al. (1992) were the first to study the effect of an oscillating spanwise flow field $w(t) = A\sin(2\pi/T\ t)$ on the turbulent flow in a channel. They either injected a transverse mass flow rate or oscillated a wall in the spanwise direction reporting the effects on the friction coefficient, Reynolds stresses and turbulence intensities. A maximum drag reduction of 40% for a period $T^+ \approx 100$ was obtained accompanied by a reduction of the streamwise Reynolds stress $\overline{uv}$ without increasing the spanwise

Reynolds stress $\overline{vw}$ which remained negligible.

Baron and Quadrio (1996) defined the performance of the oscillating wall via an energy balance where the power to move the wall was taken into account. They also proposed that drag reduction occurs because of a displacement between the low speed streaks and streamwise vortices. Quadrio and Ricco (2004) analyzed the dependence of drag reduction and power required for the oscillation on the period and amplitude obtaining a maximum net power of 7.3% with $T^+ \approx 100$ and $A^+ = 4.5$.

Choi et al. (2002) performed a parametric study of a channel and a pipe with oscillating walls. They identified a parameter related to the stokes layer and friction Reynolds number related with drag reduction rates. Quadrio and Ricco (2004) proposed a linear correlation between drag reduction and the scaling parameter defined in Choi et al. (2002). This quantity fitted satisfactorily data around the optimal period $T+ \approx 100$ but failed in the range $T^+ > 150$. Choi and Graham (1998) performed experiments of a turbulent pipe rotating around its axis obtaining a maximum drag reduction of 25 % for a period of 50-100 viscous units. They claimed that curves obtained by plotting the percentage of drag decrease against a non dimensional velocity $W = A^+/T^+$ were universal for the Reynolds numbers considered. Inspired by the work of Orlandi and Fatica (1997), Quadrio and Sibilla (2000) conducted a direct numerical simulation of an oscillating pipe getting a drag reduction comparable (40%) to the spanwise oscillating wall for a unitary non-dimensional velocity of the wall. A low $(5 - 7\%)$ net power saved was achieved when $T^+ = 100 - 150$ and the unitary velocity was small. They deduced that the rotation influenced the turbulent structures in the near wall and buffer regions while maintaining nearly unchanged the streamwise vortices.

Standing and travelling waves

Du et al. (2002) compared the effect of a spanwise oscillating forcing $F_z = I\ e^{-y/\Delta}\sin(2\pi/Tt)$ with the one of a spanwise travelling wave $F_z = I\ e^{-y/\Delta}\sin(\frac{2\pi}{\lambda_z}z - \frac{2\pi}{T}t)$. The drag reduction percentages for both were similar (30%) despite the travelling wave showed a disappearance of streaks in the near wall region. The maximum drag reduction for the travelling wave occurred for a smaller period $(T^+ = 50)$ than the one of the oscillating forcing. Drag reduction increased for small control amplitudes causing an improvement in terms of the power spent. The parameter $I \times T^+ \times \Delta$ has been identified as responsible for the drag reduction and the best performance was obtained for $I \times T^+ \times \Delta$=1.

Viotti et al. (2009) imposed a spanwise velocity $w(x) = Asin(2\pi/\lambda_x \ x)$ on a turbulent channel flow converting the time forcing of Jung et al. (1992) into a space one. The idea was suggested by the observation that a constant convection velocity $U_c \approx 10$ exists up to $y^+ = 15$ such as the temporal evolution of the spanwise velocity can be expressed as $w(t) = w(\frac{x}{U_c})$. A maximum drag reduction 12% higher than Jung et al. (1992) was obtained for $\lambda^+ \approx 1200$ in agreement with the value of the wave length computed via $\lambda^+ = U_c T^+$. This technique performed more effectively than the oscillating wall with a 23% of maximum power saved for $A^+ = 6$.

Quadrio et al. (2009) introduced a generalization of both the oscillating wall and the standing wave technique using a wall moving in the spanwise direction following the travelling wave $A\sin(k_x x - \omega t)$. A strong drag reduction occurred when the phase speed $c = \omega/k_x$ was of the same order of the convective velocity. A maximum drag reduction of 48% was obtained when $\omega \approx 0.25$ and $k_x = 1.75$. The drag increased up to 23% for $k_x = 4.5$,$\omega = 2.25$ and $c = 0.35$-0.6. The most astonishing result of this study was that the drag decreased in the same range where the power spent was minimal guaranteeing a maximum net power saving of 18%.

Quadrio and Ricco (2011) studied the relationship between travelling waves similar to the ones in Quadrio et al. (2009) (a cosine expression was used) and the related laminar problem. After analyzing a laminar related problem they defined the laminar thickness δ_l^+ of a generalized stokes layer and the laminar power spent $\mathscr{P}_{req,l}$ for the actuation. They found that δ_l^+ and $\mathscr{P}_{req,l}$ approximate well their turbulent counterparts, and proved that drag reduction was related to δ_l^+ when the wave speed U_t^+ and the convection velocity U_w^+ were of different orders of magnitude and $\left|\frac{\lambda_x^+}{U_t^+ - U_w^+}\right| \ll 120$.

Rotating discs

Keefe (1997) suggested that rotating discs on solid walls would be effective to reduce drag due to their ability to produce normal vorticity and control indirectly streamwise and spanwise velocities in the near wall region.

Ricco and Hahn (2013) simulated a turbulent channel flow with rotating discs. The skin-friction reduction was possible for diameters D was greater than a threshold related to the tangential velocity W at the disks edge. A maximum drag reduction of 23% occurred for $D = 5.07$ and $W = 0.39$. Cylindrical flow structures appeared in between disks and accounted for most of the drag component due to disks flow. The lowest disks boundary layer thickness giving the drag reduction was $\delta^+ = 6$. A maximum of 10% of net energy saved was attained for $D = 5.07$ and $W = 0.26$.

Wise and Ricco (2014) performed direct numerical simulations of a turbulent channel flow with oscillating discs on the wall surface. For a fixed tip velocity W, The period T which gave the best friction reduction was higher for larger disks. The authors found a relation between the drag reduction percentage and the parameter $W^2T^{0.3}$ by means of a laminar flow generated by an infinite disk rotating in a fluid at rest.

Wise et al. (2014) studied the effect of five different dispositions of oscillating disks on the skin-friction. Drag depended linearly on the percentage of wall equipped with disks for the hexagonal disposition and the case with tip velocity $W = 0.13$. They discovered that the drag reduction followed the equation $DR = C_w \times C_\Theta \times C \times DR_{sw}$, where C_w, C_Θ, C are parameters which take into account the waveform, the orientation of the forcing and the percentage of area covered by disks and DR_{sw} is the percentage of drag reduction of the standing waves (Viotti et al., 2009). A linear scaling relating the power to control the flow to the coverage percentage was found. Rings actuators were also considered in order to reduce the amount of power spent for the control and a maximum drag reduction of 20% was achieved when the ratio between the internal and external disks radius was 0.6.

1.1.2 Passive methods

Riblets

Research about riblets arises from the discovery that the fastest sharks species share riblets shaped denticles on their skin. The idea of exploiting this feature to design surfaces with lower turbulent friction drag was introduced by Walsh who launched a campaign of experimental tests at the Langley research center in the 1970s. Walsh and Weinstein (1979) investigated the capability of rectangular, triangular and blade riblets to influence turbulent production in boundary layers around a plate. All riblets had an height of 25 viscous units and were confined in a region where bursts cycles occurred.

During 1980s Walsh and his colleagues performed an in depth analysis about how different geometrical factors impacts on the riblet performance. Walsh (1982) discovered that drag reduction curves scaled almost perfectly with height for triangular riblets when $h^+ < 15$. Conferring a notch to the riblet tip and using a non-symmetric v-groove enlarged the range of heights and spacings where drag reduction occurred. These combined effects made possible to obtain reductions of skin-friction at different flow conditions. Walsh (1983) found out that drag curves of different riblets collapsed if plotted against the spacing and height expressed in wall units obtaining a drag reduction of 8% for $h^+ = 10$ and $s^+ = 15$. Hage et al. (2001) studied the performance of different riblets at an angle of yaw. A trapezoidal valley with a peak angle of 45 degree maintained unaltered the riblets performance to a maximum yaw angle of 10 degrees for any spacing s^+.

The mechanism behind riblets drag reduction capability has been a constant source of debate. Walsh (1983) suggested that riblets reduce turbulent drag because they restrict low speed streaks of dimension $10 < d^+ < 30$ which originate turbulence. Choi et al. (1993) claimed that riblets decrease drag because they lift the longitudinal vortices reducing the their contact with the wall therefore impeding the process of drag production. Hage et al. (2000) claimed that riblets impede the turbulent flow motion along the spanwise direction diminishing the mixing between high and low speed streams inside the turbulent boundary layer.

One disappointing aspect of straight riblets is the low drag reduction obtainable in comparison with to the one of active devices. Viotti et al. (2009) suggested the possibility of achieving the benefits of their oscillating wall by giving to riblets a spanwise sinusoidal profile. Peet et al. (2008) performed large eddy simulations of wave triangular riblets for two different values of the wavelength claiming that $\lambda_x^* = 6\delta^*$ increased drag reduction by 50% of the value of conventional triangular riblets. Grüneberger et al. (2012) studied experimentally and numerically trapezoidal grooved riblets varying the amplitude and the wavelength: they did not obtain drag reduction as Peet et al. (2008) but similar values to the ones of straight riblets.

Some authors tried to develop an hybrid between riblets and other drag reduction methods. Choi et al. (1989) studied experimentally high spaced ”U grooved” riblets covered with a polymer layer. They showed that this combination resulted in lower friction drag than the one produced by each mechanism considered separately, however a small reduction of 3.5% was attained.

Riblets features Drag reduction curves are created by plotting the percentage of drag reduction against the spacing s^+. Fig. 1.1a shows that a linear region, the ‘viscous regime’, exists for $s^+ < 15$. A further increase of s^+ reduces more the drag until a global minimum is attained for $s^+ \approx 15 - 20$, then the drag rises quickly until a behavior consistent with a wall roughness is exhibited.

Riblets modify the structure of the near wall region where velocities are of the order of the friction velocity $u_\tau^* = \sqrt{\frac{\tau_w^*}{\rho^*}}$, where τ_w^* and ρ^* are the wall shear stress and density respectively. For a smooth channel or a plate in turbulent flow a viscous sublayer (see fig. 1.1b) exists up to $y^+ \approx 5$, the flow field is almost laminar and the mean velocity obeys to the relation $u^+ = y^+$. For $y^+ > 30$ the mean velocity follows the log-law of equation $u^+ = \frac{1}{\kappa} \ln y^+ + B$ and this is defined as log-law region. An intermediate buffer layer exists in between the viscous sublayer and the log-law regions. The y^+ range where the log-law is applicable increases with the Reynolds number $U^* L^* / \nu^*$, where U^* is a characteristic velocity (the velocity at the center of the channel or the asymptotic velocity for a boundary layer), L^* is a length scale equal to the half height of the channel or the boundary layer thickness, and ν^* is the kinematic viscosity.

The classical theory of turbulence establishes that a non-smooth wall changes the factor B in the log law maintaining the same value of the Karman constant κ. If the protuberances are not completely immersed in the viscous sublayer (k-roughness) an higher drag than the smooth wall will be accompanied by a downward shift of the logarithmic profile (Leonardi et al., 2003) otherwise (riblets) drag reduction occurs and an higher B is obtained (Choi, 1989).

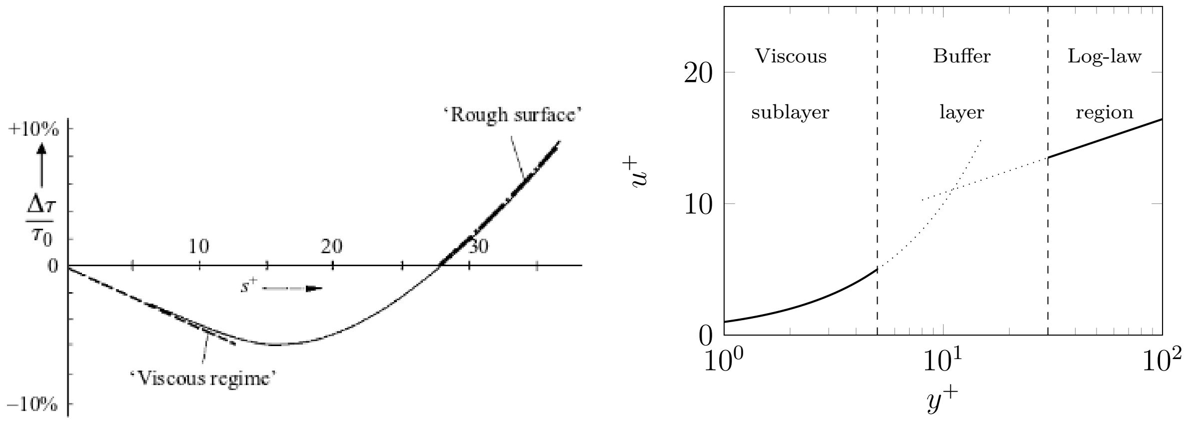

Figure 1.1: Left: Drag reduction percentage as function of the spacing s^+, adapted from Bechert et al. (1997). Right: velocity u^+ in the near wall region. The y^+ axis has a logarithmic scale.

A generic two-dimensional riblet surface can be defined as the set of points $(y_r(z), z)$ where $y_r(z)$ is the non dimensional y coordinate of the riblet at a certain spanwise location z. Fig. 1.2 shows that there is no a unique y location where the mean streamwise velocity profile approaches to zero because for any z_0 there is a $y = y_r(z_0)$ satisfying this condition. However, above a certain height the streamwise velocity does not depend anymore on z indicating the existence of a virtual origin y_{virt} in the viscous sublayer such as:

- The log law can be expressed by $u^+ = 1/\kappa \ln(y^+ + y^+_{virt}) + B + \Delta B$
- The drag calculated at the plane $y = y_{virt}$ is equal to that at the riblet surface

Many authors defined different virtual origins supposing a certain functional dependence for the mean velocity (Choi, 1989; Hooshmand et al., 1983). Choi et al. (1993) suggested it can be obtained by knowing the normal coordinates of the maximum turbulent kinetic energy production which seems to influence a translation of the logarithmic curve. The most accepted idea is the 'protrusion height' introduced by Bechert and Bertenwerfer (1989) and successively extended by Luchini et al. (1991). Luchini and his colleagues defined the virtual origin as the difference between a longitudinal and transverse protrusion heights $\Delta h = h_{||} - h_{\perp}$. Bechert et al. (1997) presented a theory (elaborated by Luchini) where they related drag reduction with Δh through the equation:

$$\frac{\Delta C_f}{C_f} = \frac{0.785\Delta h^+}{1.25 + 2C_f^{-1/2}} \tag{1.1}$$

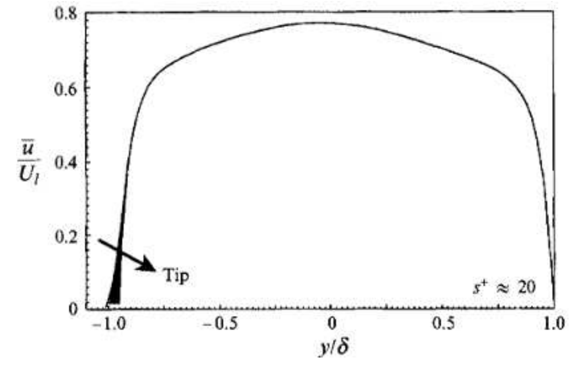

Figure 1.2: Mean streamwise velocity profile for triangular riblets, adapted from Choi et al. (1993)

1.2 Separation control methods and form drag reduction

Flow separation occurs when the flow streamlines are not able to follow the contour of a solid surface and depart significantly from it. The problem is of interest as flows around large vehicles, buildings, heat sinks and airplanes landing gears experience fluid separation.

In those engineering applications, separation causes a large increase in pressure drag to be overcome by an undesirable power expenditure; thus contributing to escalation of pressing environmental issues, such as large fuel consumption, and excessive noise and pollutant emissions. The development of flow control techniques that aim to reduce the pressure drag due to flow separation is therefore an extremely active area of academic and industrial research.

1.2.1 Active methods

Suction and blowing

The suction of fluid from a slit on the surface was the first active technique used to control flow separation (Chang, 2014). Typically, the amount of control is quantified via a mass flow rate C_m (Nuber and Needham, 1948) or a momentum C_μ coefficients (Chng et al., 2009).

Nuber and Needham (1948) found a 25% increase of the maximum lift coefficient for a NACA 64_1A212 airfoil by applying suction along the upper surface near the leading edge with a coefficient $C_m = 1.8 \times 10^{-3}$. Seifert and Pack (2002) applied steady and oscillating suction and blowing near to the separation point of a Glauert-Goldschmied airfoil. Oscillating suction and blowing effectively reduced the pressure drag for $C_\mu < 0.1\%$. Separation drag was suppressed by steady suction or blowing using $C_\mu = 0.8\%$ and $C_\mu = 2\%$ respectively, with suction having the best performance. Greenblatt et al. (2006) removed the fluid around a modified Glauert profile upper surface and form drag was reduced by increasing C_μ, showing a strong dependence on the Reynolds number. The separation bubble was suppressed for $C_\mu = 2\%$.

Some authors applied blowing over the separation line of supersonic airfoils (Bradley and Wray, 1974; Meyer and Seginer, 1994; Wong and Kontis, 2007) or backward facing step (Chun et al., 1999), reducing effectively the reattachment length.

Smith and Glezer (1997) introduced synthetic jets actuators as devices composed of a cavity with a diaphragm moved by an actuator which periodically blowed and sucked fluid from an opening at the top. Amitay and Glezer (2006) showed a delay of stall for an airfoil with up to a 15 degrees angle of attack using an actuation with a frequency 10 times higher than the airfoil characteristic one. They obtained an increase of lift with a maximum 45% decrease of the form drag at 5 degrees incidence.

Critical aspects of these active methods are the minimization of the pumping power and skin-friction penalty (Gad-el Hak et al., 1998), the electrical power to move the diaphragm, the thrust decrease due to the air drawn from the aircraft engines advised for the control (Chng et al., 2009).

Plasma actuators

Plasma actuators are devices composed of two metal electrodes separated by a dielectric material and traversed by an alternating current: the fluid is ionized by creating a volume force equivalent to a streamwise pressure gradient (Corke et al., 2002).

Post and Corke (2004) investigated the ability of plasma actuators to reattach the flow over a $NACA66_3 - 018$ airfoil at post-stall incidence. The actuators, applied at the leading edge of the airfoil and at the maximum chamber location, created a two-dimensional steady flow field that energized the boundary layer around the body. The lift L increased with the forcing magnitude up to a peak value corresponding to the fluid reattachment, while the drag D reduced proportionally to the actuation intensity, causing a maximum increase of 400% of the aerodynamic efficiency L/D. Post and Corke (2006) controlled the dynamic stall and separation on a NACA0015 airfoil oscillating around its axis by employing three types of plasma actuators that all reattached the flow. The steady actuator increased the lift, except at high angles of attack, while the unsteady actuator raised the lift only during the pitch-down phases.

Huang et al. (2006) employed a plasma actuator to control separation on a blade cascade. The actuator was located at two positions upstream of the separation point and led to a reduction of the reattachment length, similar to that obtained with vortex generators in the same configuration.

The main drawbacks of plasma actuators are the energy used for their activation, which causes a low efficiency at high Reynolds numbers (Neretti, 2016).

1.2.2 Passive methods

Vortex generators

Vortex generators are passive devices in the form of geometrical modifications, usually placed upstream of the region of separation. They are able to create streamwise vortices that enhance the turbulent mixing and allow the flow to sustain adverse pressure gradients, thereby reducing the tendency of the flow to separate. Calarese and Crisler (1985) conducted experiments on a replica of an C-130 airplane with arrays of vortex generators placed along the fuselage circumference. Vortex generators at the most upstream position were most effective at an incidence of 4 degrees, leading a 7% reduction of the total aircraft drag. Bragg and Gregorek (1987) applied three kind of vortex generators on a canard wing to alleviate the effect of boundary layer separation caused by dirt deposit. All vortex generators were able to increase the lift.

Classical vortex generators create parasite drag even when no separation occurs, and therefore research has focused on developing devices that are small enough to be completely submerged in the boundary layer. Lin et al. (1991) proved that wishbone vortex generators with an height of 20% of the boundary-layer thickness were effective in reducing the reattachment length in a descending ramp. They created a pair of counter-rotating vortices that enhanced mixing in the area with the lowest momentum. Lin et al. (1994) experimentally studied how delta and trapezoidal submerged vortex generators influenced the flow on a three-section airfoil with a flap. At low incidence (8 degrees) vortex generators placed at a quarter of the flap chord. The flap separation was controlled effectively as proved by a reduction of 60% on the wake thickness. At the same angle of attack they increased the lift by 11% and generated a drag reduction of 38% with an improvement of 80% on the aerodynamic efficiency. The main shortcoming of submerged vortex generators is that, because of their size, they are prone to damage.

1.3 Choice of the problem

In the present study, square bars are chosen because the pressure drag and the skin-friction drag are completely separated around these obstacles. The pressure drag is produced by the difference in the integrated pressures in front and behind the bars and the skin-friction drag is the result of the integrated wall-shear stress on the top of the bar and over the channel walls. The contribution of the oscillating pressure gradient to the global drag reduction can therefore be precisely quantified by the reductions of the pressure drag and the skin-friction drag.

1.4 Objective and structure of the thesis

The aim of this work is to study the effectiveness of a spanwise oscillating pressure gradient to control the fluid separation. The objective is to reduce the total drag caused by the flow separation around square bars lying on the opposite walls of a channel.

Spanwise oscillating walls and pressure gradients have been used extensively for turbulent skin-friction drag reduction (Jung et al., 1992; Trujillo et al., 1997; Quadrio and Ricco, 2004) but the study by Jukes and Choi (2012) is the only one that focused on the effect of spanwise forcing on flow separation. They were able to reattach the flow on a 20-degree inclined ramp by using spanwise jets.

Chapter §2 describes the numerical procedures for the simulations and introduces the average operators. Chapter §3 shows some preliminary simulations of a turbulent channel flow and of the uncontrolled channel flow with bars to validate and evaluate the reliability of the numerical procedures. Chapter §4 shows the solution of a laminar flow instrumental to predict the power spent for the control. Chapter §5 presents the results of of the turbulent channel flow with bars, the parameters quantifying the performance of the control, the effect of the actuation on the statistics and the drag reduction mechanism.

Chapter 2

Methodology

Two different codes were employed in this research. The former (Incompact3d) is an high order finite difference solver with an immersed boundary method to simulate the presence of obstacles inside the computational domain. The latter (Nek5000) is a spectral element code able to deal with complex geometries thanks to the creation of a grid fitted to the body surface. We chose to use two different numerical approaches because we wanted to evaluate the strengths and weaknesses of both in order to achieve our goal, i.e. simulating accurately the flow in a channel with bars and obtaining reliable values for all the quantities of interest.

2.1 Incompact3d

2.1.1 Time advancement scheme

Incompact3d employs a fractional step or splitting up method (FSM) (Temam, 2001; Chorin, 1968) to advance Navier Stokes equations in time. The method belongs to the class of projection methods: first an equation for an auxiliary velocity field $\breve{\mathbf{U}}$ is solved and then the Helmholtz decomposition is used to project $\breve{\mathbf{U}}$ into the divergence free velocity field $\mathbf{U}$. Here, we use a completely explicit FSM (Laizet and Lamballais, 2009) favorable in terms of number of computations required to obtain the solution. $\breve{\mathbf{U}}$ is calculated using the second order Adam-Bashforth method

$$\frac{\breve{\mathbf{U}} - \mathbf{U}^k}{\Delta t} = \frac{3}{2}\mathbf{F}^k - \frac{1}{2}\mathbf{F}^{k-1}, \tag{2.1}$$

where $\mathbf{F}$ represents the sum of advective and diffusive terms of NS equations, i.e. $\mathbf{F} = -\mathbf{U} \cdot \nabla \mathbf{U} + 1/Re \nabla^2 \mathbf{U}$. The advective term is expressed in the 'skew symmetric formulation'

$$-\mathbf{U} \cdot \nabla \mathbf{U} = -\frac{1}{2}[\nabla \cdot (\mathbf{U} \otimes \mathbf{U}) + (\mathbf{U} \cdot \nabla)\mathbf{U})]. \tag{2.2}$$

The divergence free constraint is guaranteed in the second step when the scalar ϕ at the new time level $k+1$ (ϕ^{k+1}) is obtained by solving the Poisson equation in the Fourier space

$$\nabla^2 \phi^{k+1} = \frac{\nabla \cdot \breve{\mathbf{U}}}{\Delta t}. \tag{2.3}$$

We point out that the fractional step used in this work is different from the one in the book of Orlandi (2012) where the pressure gradient at time t_k is considered in the first step (2.1) and a Poisson equation for the pressure correction is solved. The method used here is more similar to the one introduced by Kim and Moin (1985), the main difference being that here we use an explicit time advancement.
The velocity vector $\breve{\mathbf{U}}$ is not divergence free and verifies the physical boundary conditions is projected into the velocity at the $k+1$ th time level $\mathbf{U}^{k+1}$ thanks to

$$\mathbf{U}^{k+1} = \breve{\mathbf{U}} - \Delta t \nabla \phi^{k+1}. \tag{2.4}$$

2.1.2 Pressure field

The fractional step method eliminates the pressure field from the Navier-Stokes equations via a projection operator, therefore a procedure to recover its distribution is required. Temam (1991) claimed that an approximation of the original Navier Stokes equations is necessary to determine the pressure and he cited the scheme of Kim and Moin (1985) as a valid method. Shen (1991) showed that Kim-Moin expression for the pressure can be obtained by substituting the expression of $\breve{\mathbf{U}}$ obtained from the projection into the first predictor step and requiring consistence with the time discretized Navier-Stokes equations (see appendix A). The substitution of $\breve{\mathbf{U}}$ from (2.4) in (2.1) gives

$$\frac{\mathbf{U}^{k+1}-\mathbf{U}^{k}}{\Delta t}=\frac{3}{2}\mathbf{F}^{k}-\frac{1}{2}\mathbf{F}^{k-1}-\nabla\phi^{k+1}. \tag{2.5}$$

In order to find an approximation for the pressure we consider the following expansions

$$\frac{\mathbf{U}^{k+1}-\mathbf{U}^{k}}{\Delta t}=\left.\frac{\partial\mathbf{U}}{\partial t}\right|^{k+1/2}+O(\Delta t^2),\quad \frac{3}{2}\mathbf{F}^{k}-\frac{1}{2}\mathbf{F}^{k-1}=\mathbf{F}^{k+1/2}+O(\Delta t^2). \tag{2.6}$$

The substitution of (2.6) into (2.5) gives

$$\left.\frac{\partial\mathbf{U}}{\partial t}\right|^{k+1/2}=\mathbf{F}^{k+1/2}-\nabla\phi^{k+1}+O(\Delta t^2). \tag{2.7}$$

The momentum equation at time $t_{k+1/2}$ reads

$$\left.\frac{\partial\mathbf{U}}{\partial t}\right|^{k+1/2}=\mathbf{F}^{k+1/2}-\nabla p^{k+1/2}. \tag{2.8}$$

By comparing (2.8) and (2.7) we obtain $p^{k+1/2}=\phi^{k+1}+O(\Delta t^2)$. Our aim is to obtain the pressure at time t_{k+1} and not at the intermediate time level $k+1/2$ hence by considering that $p^{k+1}=p^{k+1/2}+O(\Delta t)$ we find

$$p^{k+1}=\phi^{k+1}+O(\Delta t^2)+O(\Delta t)=\phi^{k+1}+O(\Delta t). \tag{2.9}$$

Therefore the pressure approximation is first order in time.

Streamwise pressure gradient for a channel flow

In a channel flow periodic boundary conditions along the streamwise and spanwise directions are employed for the velocity. It follows from eq. (2.4) that ϕ^{k+1} is periodic in the streamwise direction. As the flow is decelerated by the action of the drag force at the solid walls it is necessary to include an opposite force to move the fluid, introduced via a streamwise pressure gradient Π_x^{k+1}. By replacing (2.4) with the equation

$$\mathbf{U}^{num}=\breve{\mathbf{U}}-\Delta t\nabla\phi^{k+1}, \tag{2.10}$$

it is possible to introduce an additional step to the scheme

$$\mathbf{U}^{k+1}=\mathbf{U}^{num}-\ \Delta t\ \Pi_x^{k+1}\,\mathbf{i}, \tag{2.11}$$

where $\mathbf{i}$ is the unit vector along x.

If a simulation is performed at 'constant pressure gradient' then Π_x^{k+1} is fixed at any time step. For a simulation with a 'constant mass flow' with time a further procedure is necessary. By averaging on the fluid volume the x component of (2.11) we obtain

$$\Pi_x^{k+1} = -\frac{U_b - U_b^{num}}{\Delta t}, \tag{2.12}$$

where U_b and U_b^{num} are the physical ($U_b = 1/V_F \int_{V_F} u \, \mathrm{d}V$) and numerical bulk velocity ($U_b = 1/V_F \int_{V_F} u^{num} \, \mathrm{d}V$) obtained at the end of the fractional step. As shown in section 2.1.2, the pressure is first order accurate in time and reads

$$p^{k+1} = \phi^{k+1} + \Pi_x^{k+1} \, x + p_{ref} + O(\Delta t), \tag{2.13}$$

where $\Pi_x^{k+1} \, x + p_{ref}$ is obtained by integrating Π_x^{k+1} along x and p_{ref} is a constant reference pressure.

Spanwise pressure gradient

In this work a spanwise pressure gradient Π_z^{k+1} is used as a control mean in addition to the streamwise pressure gradient Π_x^{k+1}. In place of eq. (2.11) we use the equation

$$\mathbf{U}^{k+1} = \mathbf{U}^{num} - \Delta t \, \Pi_x^{k+1} \, \mathbf{i} - \Delta t \, \Pi_z^{k+1} \, \mathbf{k}, \tag{2.14}$$

where $\mathbf{k}$ is the unit vector along z and the pressure field p^{k+1} is

$$p^{k+1} = \phi^{k+1} + \Pi_x^{k+1} \, x + \Pi_z^{k+1} \, z + p_{ref} + O(\Delta t). \tag{2.15}$$

2.1.3 Space differentiation scheme

The knowledge of convective and diffusive terms in $\mathbf{F}^k$ and $\mathbf{F}^{k-1}$ is required to compute the auxiliary velocity $\breve{\mathbf{U}}$. This is accomplished by calculating the first and second derivatives for the advective an diffusive term respectively.

Incompact3d employs compact finite differences (Lele, 1992) for the calculation of the space derivatives. An inversion of a tridiagonal system is necessary to find the derivative of a function at the mesh points. The scheme for the first derivative of a quantity q is

$$\xi q^{'}_{j-1} + q^{'}_j + \xi q^{'}_{j+1} = g_j \ (q_{j-2}, q_{j-1}, q_{j+1}, q_{j+2}), \qquad j = 1, .., n, \tag{2.16}$$

where q_j and $q^{'}_j$ are the known value of q and its unknown derivative at point j, ξ is a coefficient related to the accuracy of the scheme, g_j is a known function and depends linearly on the $q_{j-2}, q_{j-1}, q_{j+1}, q_{j+2}$ and n is the total number of points.

The first ($j = 1$) and last equation ($j = n$) of the system (2.16) requires the values of q and q' external to the computational domain (q_{-1}, q_0, q_{n+1}, q_{n+2}, q'_0, q'_{n+1}) therefore a set of boundary conditions is necessary. For instance, equation (2.16) at $j = 1$ reads

$$\xi q^{'}_0 + q^{'}_1 + \xi q^{'}_2 = g_1 \ (q_{-1}, q_0, q_2, q_3). \tag{2.17}$$

If q is periodic the boundary conditions are

$$q_{-1} = q_{n-1}, \ \ q_0 = q_n, \ \ q^{'}_0 = q^{'}_n. \tag{2.18}$$

For homogeneous Neumann ($q'_1 = 0$) and Dirichlet ($q_1 = 0$) the second order schemes

$$q'_1 = \frac{q_2 - q_0}{2\Delta y} + O(\Delta y^2), \quad q'_1 = \frac{q_3 - q_{-1}}{4\Delta y} + O(\Delta y^2), \tag{2.19a}$$

$$q_1 = \frac{q_3 + q_{-1}}{2} + O(\Delta y^2) \quad q_1 = \frac{q_2 + q_0}{2} + O(\Delta y^2) \tag{2.19b}$$

$$q'_2 + q'_0 = \frac{q_3 - q_{-1}}{2\Delta y} + O(\Delta y^2), \tag{2.19c}$$

gives

$$q_0 = q_2, \quad q_{-1} = q_3, \quad q^{'}_0 = -q^{'}_2, \tag{2.20a}$$

$$q_0 = -q_2, \quad q_{-1} = -q_3, \quad q^{'}_0 = q^{'}_2. \tag{2.20b}$$

For a generic Dirichlet conditions eq. 2.17 at $j = 1$ and $j = 2$ is substituted by the two schemes

$$q^{'}_1 + 2q^{'}_2 = g' \ (q_1, q_2, q_3), \ \ \frac{1}{4}q^{'}_1 + q^{'}_2 + \frac{1}{4}q^{'}_3 = g'' \ (q_1, q_3), \tag{2.21}$$

where g' and g'' are linear functions of their arguments. Similar considerations are valid for the second derivative q''

$$\eta q^{''}_{j-1} + q^{''}_j + \eta q^{''}_{j+1} = h_j \ (q_{j-3}, q_{j-2}, q_{j-1}, q_j, q_{j+1}, q_{j+2}, q_{j+3}), \qquad j = 1, .., n. \tag{2.22}$$

2.1.4 The immersed boundary method

The immersed boundary method (IBM) was developed by Peskin (1972) to study the blood flow inside an human heart. Many IBM methods have been employed to study fluid dynamics problems with complex geometries and an excellent review of the different approaches can be found in Mittal and Iaccarino (2005). Incompact3d employs a direct IBM (Mohd-Yusof, 1997) which imposes the no-slip condition accurately and efficiently for flows with high Reynolds number.

Direct immersed boundary method

The Navier-Stokes equations are modified with a formal forcing term $\mathbf{f}$ vanishing only in the fluid region

$$\frac{\partial \mathbf{U}}{\partial t} + (\mathbf{U} \cdot \nabla)\mathbf{U} = -\nabla p + \frac{1}{Re}\nabla^2 \mathbf{U} + \mathbf{f}. \tag{2.23}$$

By discretizing the previous equation in time we find

$$\frac{\mathbf{U}^{k+1} - \mathbf{U}^k}{\Delta t} = \frac{3}{2}\mathbf{F}^k - \frac{1}{2}\mathbf{F}^{k-1} - \nabla p^{k+1} + \mathbf{f}^{k+1}. \tag{2.24}$$

The velocity boundary conditions at wall are imposed via $\mathbf{U}^{k+1} = \mathbf{U}_0$, where $\mathbf{U}_0$ is the velocity at the immersed body. From eq. (2.24) we find that $\mathbf{f}^{k+1}$ at the body is

$$\mathbf{f}_B^{k+1} = \frac{\mathbf{U}_0 - \mathbf{U}^k}{\Delta t} - \frac{3}{2}\mathbf{F}^k + \frac{1}{2}\mathbf{F}^{k-1} + \nabla p^{k+1}. \tag{2.25}$$

A mask function χ equal to zero in the fluid and one inside the immersed body must be introduced to have $\mathbf{f} = 0$ in the fluid region

$$\mathbf{f}^{k+1} = \chi \left(\frac{\mathbf{U}_0 - \mathbf{U}^k}{\Delta t} - \frac{3}{2}\mathbf{F}^k + \frac{1}{2}\mathbf{F}^{k-1} + \nabla p^{k+1} \right). \tag{2.26}$$

It is important to emphasize that the forcing $\mathbf{f}^{k+1}$ is not computed via eq. (2.26) but the condition $\mathbf{U}^{k+1} = \mathbf{U}_0$ is directly enforced at the body points if they coincide with grid nodes otherwise an interpolation procedure is required.

IBM with $\mathring{\mathbf{U}} = \mathbf{0}$ When a solid body is placed inside the computational domain the basic fractional step method has to be modified in order to guarantee $\mathbf{U}^{k+1} = \mathbf{U}_0 = \mathbf{0}$. In the region fulfilled with the fluid step (2.1) becomes

$$\frac{\mathring{\mathbf{U}} - \mathbf{U}^k}{\Delta t} = \frac{3}{2}\mathbf{F}^k - \frac{1}{2}\mathbf{F}^{k-1} - \nabla p^k \qquad \forall \mathbf{x} \in V_F \tag{2.27}$$

The boundary condition $\mathring{\mathbf{U}}_B = \mathbf{0}$ is imposed inside the body and the following step applies to the domain including both the fluid and the body

$$\frac{\breve{\mathbf{U}} - \mathring{\mathbf{U}}}{\Delta t} = \nabla p^k \qquad \forall \mathbf{x} \in V_F \cup V_B \tag{2.28}$$

In the fluid region V_F the equation

$$\frac{\mathbf{U}^{k+1} - \mathbf{U}^k}{\Delta t} = \frac{3}{2}\mathbf{F}^k - \frac{1}{2}\mathbf{F}^{k-1} - \nabla p^{k+1} \qquad \forall \mathbf{x} \in V_F \tag{2.29}$$

is recovered while in the immersed body the scheme reads

$$\begin{aligned} \mathbf{U}_B^{k+1} =& \breve{\mathbf{U}}_B - \Delta t \nabla p^{k+1} = \mathbf{U}_B^* + \Delta t \nabla p_B^k - \Delta t \nabla p_B^{k+1} = \\ =& - \Delta t^2 \left(\nabla \frac{\partial}{\partial t} p_B^k \right) = O(\Delta t^2). \end{aligned} \qquad \forall \mathbf{x} \in V_B. \tag{2.30}$$

Therefore the no-slip condition is satisfied approximately.

Alternate direct forcing IBM The previous IBM introduces a discontinuity in the velocity gradients at the immersed body which creates oscillations when a spectral code is used (Goldstein et al., 1993). This phenomenon was not observed for second order codes and affects Incompact3d which is based on a compact finite difference scheme (Lamballais and Silvestrini; Parnaudeau et al., 2004). Gautier et al. (2014) modified Incompact3d interpolating the velocity $\mathbf{U}^k$ inside the immersed body before calculating the convective and diffusive terms stored in $\mathbf{F}^k$.

Fig. 2.1a shows the procedure to find the x location of a body point which does not lie on the mesh. Given a y, z plane, the codes creates a mask function $\chi_x(x, y, z)$ in the same manner as χ but with a space step which is a fraction of Δx. The x coordinate of the boundary is approximated by the position of the middle point of the interval whose extremes have χ_x values of 0 (fluid) and 1 (solid). The same principle is applied along the other two directions creating $\chi_y(x, y, z)$ and $\chi_z(x, y, z)$ functions. Fig. 2.1b shows that four points (squares) are used for the polynomial representation in each fluid side including the surface location where the no slip condition applies. The first point in a fluid region (circle) is not considered in the interpolation because is often too close to the body surface node and this can generate a divergent polynomial.

The interpolation is repeated three times (the number of space coordinates) for each velocity component furnishing three different velocity values for every point inside the body.

The main disadvantage of this procedure is the need of at least four points in the fluid side for every one dimensional reconstruction and this increases significantly the resolution necessary to analyze cases where small immersed bodies are involved.

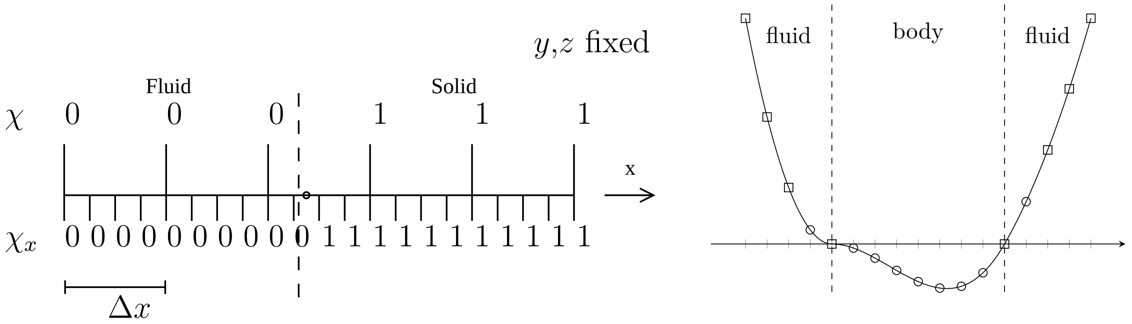

Figure 2.1: Left: Method to find the body interface. Dashed line indicates the exact position of the boundary, the circle represents the approximate position. Right: Lagrangian polynomial interpolation.

Mass flow rate requirements with IBM

Global mass conservation, obtained by integrating the continuity equation $\nabla \cdot \mathbf{u} = 0$ on the fluid volume V_F, is satisfied via

$$U_b = \frac{1}{V_F} \int_{V_F} u^{k+1} \, \mathrm{d}V = \text{const} \tag{2.31}$$

By averaging the x component of (2.11) on V_F we get

$$\frac{1}{V_F} \int_{V_F} u^{k+1} \, \mathrm{d}V = \frac{1}{V_F} \int_{V_F} u^{num} \, \mathrm{d}V - \Delta t \Pi_x^{k+1} = U_b = \text{const}, \tag{2.32}$$

where Π_x is a function of time. From (2.32) is follows that the streamwise pressure gradient is

$$\Pi_x^{k+1} = \frac{1}{\Delta t} \left(\frac{1}{V_F} \int_{V_F} u^{num} \, \mathrm{d}V - U_b \right). \tag{2.33}$$

The value Π_x^{k+1} given by (2.33) should be considered just in the fluid region V_F otherwise a non-zero velocity would be created at the body wall.

2.2 Nek5000

2.2.1 Time advancement scheme

Nek5000 advances the Navier Stokes equations in time via an implicit and explicit scheme for the diffusive and the advective terms respectively. Two types of time advancements are available: an operator integration factor splitting (OIFS) (Maday et al., 1990) and an extrapolation scheme (EXT) with backward differentiation (BDF).

OIFS

This scheme permits simulations with relatively high time steps:

$$\frac{3\mathbf{U}^{k+1} - 4\breve{\mathbf{U}} + \mathring{\mathbf{U}}}{2\Delta t} = -\nabla p^{k+1} + \frac{1}{Re}\nabla^2 \mathbf{U}^{k+1}, \tag{2.34}$$

where $\breve{\mathbf{U}}$ and $\mathring{\mathbf{U}}$ satisfy the advection problems

$$\begin{cases} \frac{\partial \breve{\mathbf{U}}}{\partial t} + \mathbf{U} \cdot \nabla \breve{\mathbf{U}} = \mathbf{0} \\ \breve{\mathbf{U}}(\mathbf{x}, 0) = \mathbf{U}^k \end{cases} \quad \begin{cases} \frac{\partial \mathring{\mathbf{U}}}{\partial t} + \mathbf{U} \cdot \nabla \mathring{\mathbf{U}} = \mathbf{0} \\ \mathring{\mathbf{U}}(\mathbf{x}, 0) = \mathbf{U}^{k-1} \end{cases} \tag{2.35}$$

solved in $[0, \Delta t]$ via a fourth order Runge Kutta method (RK4). Equation (2.34) does not suffer stability problems but eqs (2.35) are integrated using RK4 repeatedly with a time step which is a fraction of Δt (Maday et al., 1990).

EXT

The unsteady term at t_{k+1} is discretized using a backward finite difference scheme and the advective term a t_{k+1} is extrapolated using velocities at previous time steps $\mathbf{U}^k$ and $\mathbf{U}^{k-1}$

$$\frac{3\mathbf{U}^{k+1} - 4\mathbf{U}^k + \mathbf{U}^{k-1}}{2\Delta t} = -\nabla p^{k+1} + \frac{1}{Re}\nabla^2 \mathbf{U}^{k+1} - 2\mathbf{U}^k \cdot \nabla \mathbf{U}^k + \mathbf{U}^{k-1} \cdot \nabla \mathbf{U}^{k-1}. \tag{2.36}$$

After space discretization both schemes (2.36) and (2.34) can be written as

$$\mathbf{H}\mathbf{U}_D^{k+1} - \mathbf{D}^T \left(\mathbf{P}^{k+1} - \mathbf{P}^k\right) = \mathbf{B}\mathbf{F}^{k+1} + \mathbf{D}^T \mathbf{P}^k \tag{2.37}$$

where $\mathbf{L}$ is the matrix representing the Laplace operator, $\mathbf{H} = \frac{3}{2\Delta t}\mathbf{B} - \frac{1}{Re}\mathbf{L}$ is an Helmholtz operator, $\mathbf{B}$ the mass matrix, $\mathbf{D}^T$ the matrix related to the gradient, $\mathbf{U}_D$ and $\mathbf{P}$ the vectors containing velocity and pressure unknowns at the grid points. This equation can be split in two steps noticing that

$$\frac{2}{3}\Delta t\, \mathbf{H}\mathbf{B}^{-1} = \mathbf{I} - \frac{2}{3}\frac{\Delta t}{Re}\mathbf{L}\mathbf{B}^{-1} = \mathbf{I} + O(\Delta t), \quad \left(\mathbf{P}^{k+1} - \mathbf{P}^{k}\right) = O(\Delta t), \tag{2.38}$$

where $\mathbf{I}$ is the identity matrix. Eq. (2.39) can be written as

$$\mathbf{H}\mathbf{U}_D^{k+1} - \frac{2}{3}\Delta t\, \mathbf{H}\mathbf{B}^{-1}\mathbf{D}^T\left(\mathbf{P}^{k+1} - \mathbf{P}^{k}\right) = \mathbf{B}\mathbf{F}^{k+1} + \mathbf{D}^T\mathbf{P}^k, \tag{2.39}$$

because the error introduced by 2.38 is of the same order ($O(\Delta t^2)$) of the one due to time discretization. Eq. (2.39) can be split into

$$\begin{cases} \mathbf{H}\, \breve{\mathbf{U}}_D = \mathbf{B}\mathbf{F}^{k+1} + \mathbf{D}^T\mathbf{P}^k \\ \mathbf{U}_D^{k+1} = \breve{\mathbf{U}}_D + \frac{2}{3}\Delta t\, \mathbf{B}^{-1}\mathbf{D}^T\delta\mathbf{P}, \quad \mathbf{P}^{k+1} = \mathbf{P}^k + \delta\mathbf{P} \end{cases} \tag{2.40}$$

In the first step $\breve{\mathbf{U}}_D$, which is not divergence free, is found. $\breve{\mathbf{U}}_D$ is corrected subsequently via $\delta\mathbf{P}$ to obtain the final vector $\mathbf{U}_D^{k+1}$.

2.2.2 Pressure correction equation

The last step in eq. (2.40) requires the knowledge of the pressure correction $\delta\mathbf{P}$. The continuity equation reads $\mathbf{D}\mathbf{U}_D^{k+1} = \mathbf{0}$ with $\mathbf{D}$ the matrix representing the divergence operator. The pressure correction is obtained applying $\mathbf{D}$ to (2.40):

$$\frac{2}{3}\Delta t\, \mathbf{D}\mathbf{B}^{-1}\mathbf{D}^T\delta\mathbf{P} = -\mathbf{D}\breve{\mathbf{U}}_D. \tag{2.41}$$

$\breve{\mathbf{U}}_D$ is found from the first eq. of (2.40), $\delta\mathbf{P}$ is obtained solving (2.41), $\mathbf{U}_D^{k+1}$ and $\mathbf{P}^{k+1}$ are computed using the second of eq. (2.40).

2.2.3 Spectral element discretization

The Navier Stokes equations are discretized in space via the spectral element method (SEM) which is an high order weighted residual technique applied to the weak form of equation (2.34) or (2.36). The fluid domain is split into hexahedral elements V_e. A test function Q, velocity components and pressure are expanded in V_e via the Lagrange polynomials

$$\begin{cases} u(\mathbf{x}^e(\xi,\eta,\zeta))\big|_{V_e} = \sum_{k=1}^{l_x}\sum_{j=0}^{l_y}\sum_{i=0}^{l_z} u^e_{i,j,k}(t)F_i(\xi)G_j(\eta)H_k(\zeta), \\ v(\mathbf{x}^e(\xi,\eta,\zeta))\big|_{V_e} = \sum_{k=1}^{l_x}\sum_{j=0}^{l_y}\sum_{i=0}^{l_z} v^e_{i,j,k}(t)F_i(\xi)G_j(\eta)H_k(\zeta), \\ w(\mathbf{x}^e(\xi,\eta,\zeta))\big|_{V_e} = \sum_{k=1}^{l_x}\sum_{j=0}^{l_y}\sum_{i=0}^{l_z} w^e_{i,j,k}(t)F_i(\xi)G_j(\eta)H_k(\zeta), \\ p(\mathbf{x}^e(\xi,\eta,\zeta))\big|_{V_e} = \sum_{k=1}^{l_x}\sum_{j=0}^{l_y}\sum_{i=0}^{l_z} p^e_{i,j,k}(t)F_i(\xi)G_j(\eta)H_k(\zeta), \\ Q(\mathbf{x}^e(\xi,\eta,\zeta))\big|_{V_e} = \sum_{k=1}^{l_x}\sum_{j=0}^{l_y}\sum_{i=0}^{l_z} Q^e_{i,j,k}(t)F_i(\xi)G_j(\eta)H_k(\zeta), \end{cases} \tag{2.42}$$

where $\mathbf{x}^e = (x^e, y^e, z^e)$ is the coordinate map from the space $[-1,1]^3$ of the $l_x l_y l_z = l_x^3$ Gauss-Lobatto-Legendre (GLL) points (ξ_i, η_j, ζ_k) into the physical domain V_e see fig. 2.2. The GLL points are more clustered near the edges of the elements, this points distribution is responsible for the spectral accuracy of the method. The functions F_i, G_j, H_k are such as $F_i(\xi_l) = \delta^{(kr)}_{i,l}$, $G_j(\eta_l) = \delta^{(kr)}_{j,l}$ and $H_k(\zeta_l) = \delta^{(kr)}_{k,l}$ where $\delta^{(kr)}$ is the kronecker delta. The contribution of a spectral element is obtained by multiplying (2.34) or (2.36) for Q, integrating on V_e and using eqs (2.42). The discretised system of the fluid domain $V_F = \sum_{e=1}^{N_e} V_e$ is obtained by adding all the contribution of all the spectral elements. At the end it is possible to write the system (2.39) where velocity and pressure values at grid points are unknown (Deville et al., 2002).

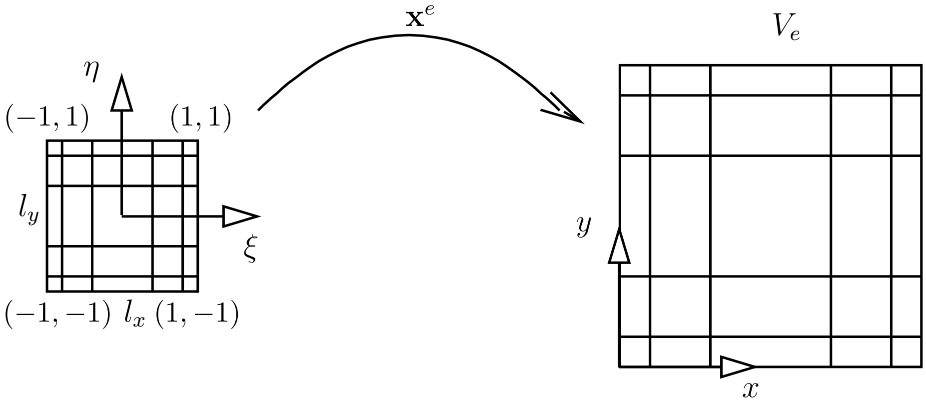

Figure 2.2: Mapping from the (GLL) points (ξ_i, η_j) to the mesh points inside the spectral element. The edges of the element are discretized using $l_x = l_y$ GLL points. Note that a two dimensional spectral element is showed for simplicity

2.3 Averaging operators

The average of a quantity q along an homogeneous direction z is denoted as

$$\langle q \rangle (x, y, t) = \frac{1}{L_z} \int_0^{L_z} q(x, y, z, t) \mathrm{d}z. \tag{2.43}$$

Note that eq. (2.43) can be applied multiple times if a flow presents multiple homogeneous directions. The time ensemble average is defined as

$$\widehat{q}\,(x, y, z, \tau) = \frac{1}{N} \sum_{l=0}^{N-1} q\,(x, y, z, t + l\,T)\,, \qquad 0 \leq \tau < T, \tag{2.44}$$

where N is the number of periods.

The time average is

$$\overline{q}(x, y, z) = \frac{1}{t_f - t_i} \int_{t_i}^{t_f} q(x, y, z, t) \mathrm{d}t, \tag{2.45}$$

where t_i and t_f are the initial and final times used for averaging. Note that in the controlled case fields are statistically periodic and the interval for the time average is an integer multiple of the the period T, i.e $t_f - t_i = NT$.

Chapter 3

Testing and discussion

The two codes presented in the previous chapter are tested to find strengths and weaknesses of each numerical approach. Incompact3d is validated by simulating a turbulent channel flow and comparing the results with those obtained by Kim et al. (1987). A channel flow was chosen because it has been studied extensively and the computation of its statistics is an easily accomplished task. Afterward a turbulent channel and a channel with a constriction were studied to evaluate the suitability of the IBM to compute the pressure field. A correct prediction of the pressure is crucial for the control of a separated flow where pressure drag is the main component of the global resistance. Lastly Incompact3d and Nek5000 were both used to simulate the flow that we want to control in this work, i.e. a channel with transverse bars, and determine the more appropriate approach to compute the drag in this configuration.

3.1 Channel flow

A channel flow is a problem where the fluid moves in between two horizontal flat solid surfaces. In this thesis, we indicate dimensional quantities with an asterisk. The boundary conditions are periodic along the streamwise and spanwise direction and the no-slip condition applies at the walls. The Cartesian coordinates are x^* , y^* and z^* along the the streamwise, vertical and spanwise direction respectively. The size of the computational domain is $L_x^* = 4\pi\delta^*$, $L_y^* = 2\delta^*$, $L_z^* = 2\pi\delta^*$.

Lengths are scaled using δ^* and velocities are scaled with the midline velocity U_p^* for a laminar Poiseuille flow $u^* = U_p^*/{\delta^*}^2(2\delta^* y^* - {y^*}^2)$ with bulk velocity $U_b^* =$

$1/L_y^* \int_0^{L_y^*} u^* \mathrm{d}y^* = 2/3U_p^*$. The simulation starts from this Poiseuille flow plus a perturbation of zero mean to trigger the turbulence. The time t^* is scaled as $t = t^* U_p^*/\delta^*$. The Reynolds number is $Re_p = U_p^* \delta^*/\nu^* = 4200$, where ν^* is the kinematic viscosity.

3.1.1 Resolution $192 \times 129 \times 192$, time step $\Delta t = 5.0 \times 10^{-3}$

The time step is $\Delta t = 5.0 \times 10^{-3}$ or $\Delta t^+ = 3.8 \times 10^{-2}$ in wall units. A third order Runge Kutta scheme was used to advance the equations in time and a mesh stretched along y with $192 \times 129 \times 192$ points was employed. The grid spacings in wall units along x and z are $\Delta x^+ = 12$ and $\Delta z^+ = 6$ respectively. The simulation is run on the POLARIS cluster of The University of Leeds employing 64 mpi processes.

Transient analysis

Any turbulent flow field experiences a transient before reaching a statistical steady state therefore the simulation must run for sufficient time before conducting any statistical analysis. Fig. 3.1 shows quantities averaged on x and z at the location y_{pe} corresponding to the peak of $\langle \overline{u_t u_t} \rangle (y)$ against the current time step t. All the curves begin to oscillate around their mean values after a transient which lasts approximately 250 Poiseuille time units.

Time average convergence

Statistics are obtained by time averaging any quantity of interest: a theoretical infinite time averaging window ($(t_f - t_i) \rightarrow +\infty$) would be necessary. However, only a limited time window can be considered assuming that the resulting statistics obtained approximate well the true statistics.

In fig. 3.2 the time convergence of the simulation is evaluated by plotting the skin-friction drag coefficient defined as

$$c_f = \frac{\tau_w^*}{\frac{1}{2}\rho^* U_b^{*2}}, \tag{3.1}$$

where τ_w^* is the wall shear-stress. The coefficient c_f is well converged for $t_f - t_i > 50$ when its oscillations are completely enclosed by the two lines indicating variations of

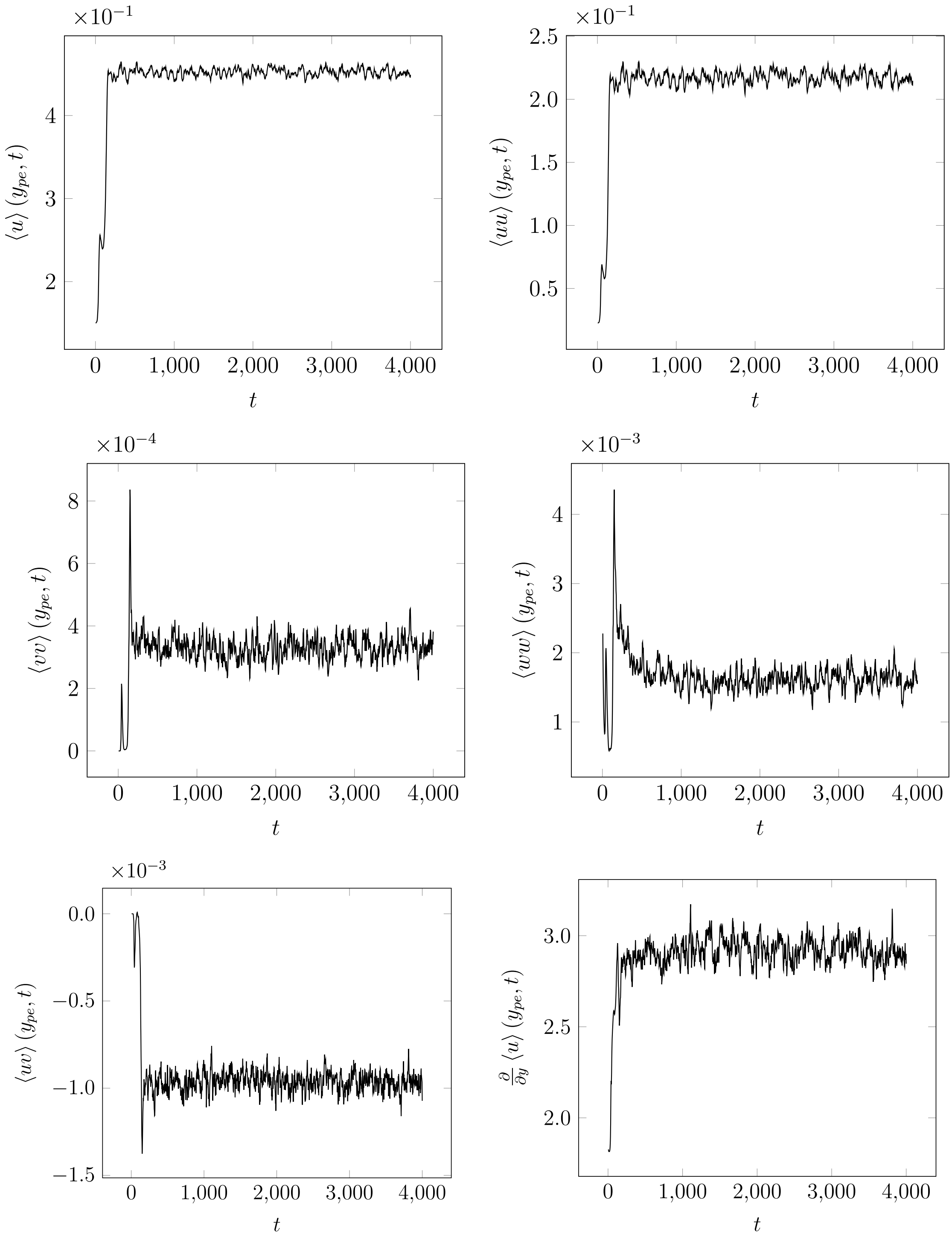

Figure 3.1: Plane averaged quantities at $y_{pe} = 8.05{\times}10^{-2}$, the location of the maximum root mean square value of the streamwise turbulent velocity. t indicates the current time.

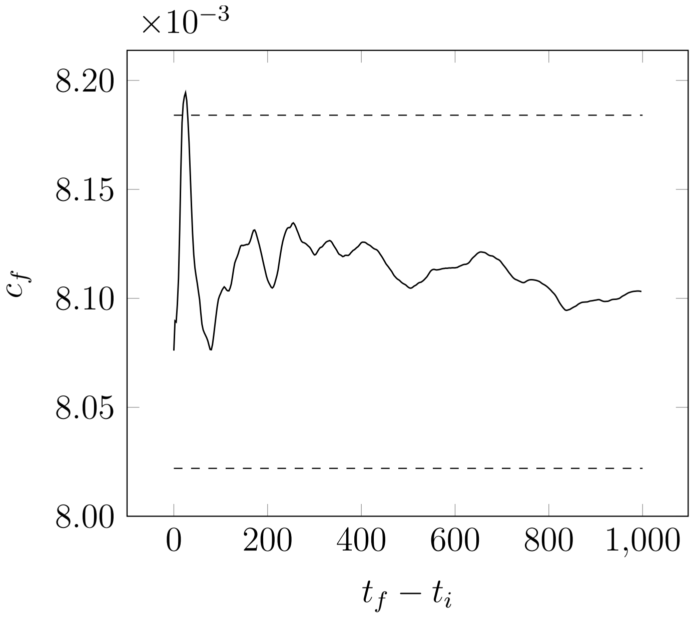

Figure 3.2: Skin-friction coefficient as function of the time window $t_f - t_i$ used for time-averaging. The dashed lines stem for skin-friction values $(100 \pm 1)\%\, c_f$, where c_f is the value obtained for $t_f - t_i = 1000$.

±1% on the nominal value $c_f = 8.10 \times 10^{-3}$ which agrees well with the one found by Kim et al. (1987).

The total shear stress normalized by the wall shear stress is useful to evaluate if the flow is developed because it has the analytical expression

$$\frac{\tau^*}{\tau^*_w} = \frac{\tau^*}{\rho^* {u^*_\tau}^2} = \left[\frac{1}{Re_p} \left(\frac{\mathrm{d}\left\langle \overline{u} \right\rangle}{\mathrm{d}y} \right)_{y=0} - \left\langle \overline{u_t v_t} \right\rangle \right] \left(\frac{U^*_p}{u^*_\tau} \right)^2 = 1 - y. \tag{3.2}$$

Fig. 3.3a shows that the τ^*/τ^*_w obtained agrees perfectly with (3.2) confirming that the flow is statistically developed.

Fig. 3.3b presents $\langle \overline{uu} \rangle$, $\langle \overline{vv} \rangle$, $\langle \overline{ww} \rangle$, $\langle \overline{uv} \rangle$ normalized by u_τ for an increasing interval used for the time average showing that variances and the Reynolds stress reach the time convergence after a time interval $t_f - t_i = 250$.

Statistical results

Statistics are compared with those obtained by Kim et al. (1987) and Moser et al. (1999). Fig 3.4a shows that the mean velocity in wall units computed by the Kim and his colleagues is lower than the one of Moser and Incompact3d outside the viscous sublayer ($y^+ > 5$). Fig. 3.4b shows that velocity variances and Reynolds stress obtained with Incompact3d agrees with the ones of Moser DNS while Kim results

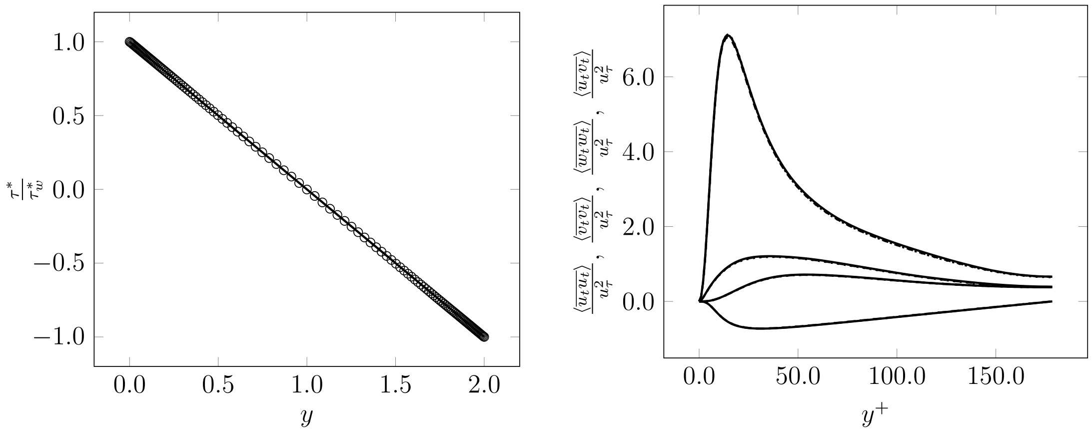

Figure 3.3: Left:Total shear stress normalized by the wall shear stress against y. The solid line indicates the theoretical value $1-y$ while circles represent results from DNS. Right: Velocity variances and Reynolds stress obtained by averaging along a time interval of 250 (solid), 500 (dashed) and 1000 (dotted) time units.

show some differences with our results.

Turbulent kinetic energy equation

In this section, the turbulent kinetic energy equation expressed in two different ways is analyzed. The two equations can be found in the books of Pope (2000) and Hinze (1975). The first equation written in non-dimensional form is

$$-\frac{1}{2}\frac{\mathrm{d}}{\mathrm{d}y}\left\langle\overline{v_t({u_t}^2+{v_t}^2+{w_t}^2)}\right\rangle-\langle\overline{u_t v_t}\rangle\,\frac{\mathrm{d}\,\langle\overline{u}\rangle}{\mathrm{d}y}+\frac{1}{Re_p}\frac{\mathrm{d}^2\,\langle\mathcal{K}\rangle}{\mathrm{d}y^2}-\frac{\mathrm{d}}{\mathrm{d}y}\,\langle\overline{p_t v_t}\rangle-\widetilde{\varepsilon}=0, \quad (3.3)$$

where the subscript t indicates the turbulent fluctuations, $\mathcal{K}=\frac{1}{2}\overline{({u_t}^2+{v_t}^2+{w_t}^2)}$ is the turbulent kinetic energy and the pseudo-dissipation $\widetilde{\varepsilon}$ is defined as

$$\begin{aligned}\widetilde{\varepsilon}=&\frac{1}{Re_p}\Big[\Big\langle\ \overline{\Big(\frac{\partial u_t}{\partial x}\Big)^2}+\overline{\Big(\frac{\partial u_t}{\partial y}\Big)^2}+\overline{\Big(\frac{\partial u_t}{\partial z}\Big)^2}+\overline{\Big(\frac{\partial v_t}{\partial x}\Big)^2}+\\&+\overline{\Big(\frac{\partial v_t}{\partial y}\Big)^2}+\overline{\Big(\frac{\partial v_t}{\partial z}\Big)^2}+\overline{\Big(\frac{\partial w_t}{\partial x}\Big)^2}+\overline{\Big(\frac{\partial w_t}{\partial y}\Big)^2}+\overline{\Big(\frac{\partial w_t}{\partial z}\Big)^2}\ \Big\rangle\Big]\end{aligned} \quad (3.4)$$

The terms of (3.3) are turbulent convection, production,viscous diffusion, turbulent pressure transport and pseudo dissipation respectively. Figure 3.5a shows the terms of (3.3) obtained using three time average windows $t_f-t_i=250,500,1000$. The three profiles almost overlap over the y^+ range considered except in the interval $25<y^+<75$ where the production shows some variation with t_f-t_i, therefore an acceptable time convergence is achieved.

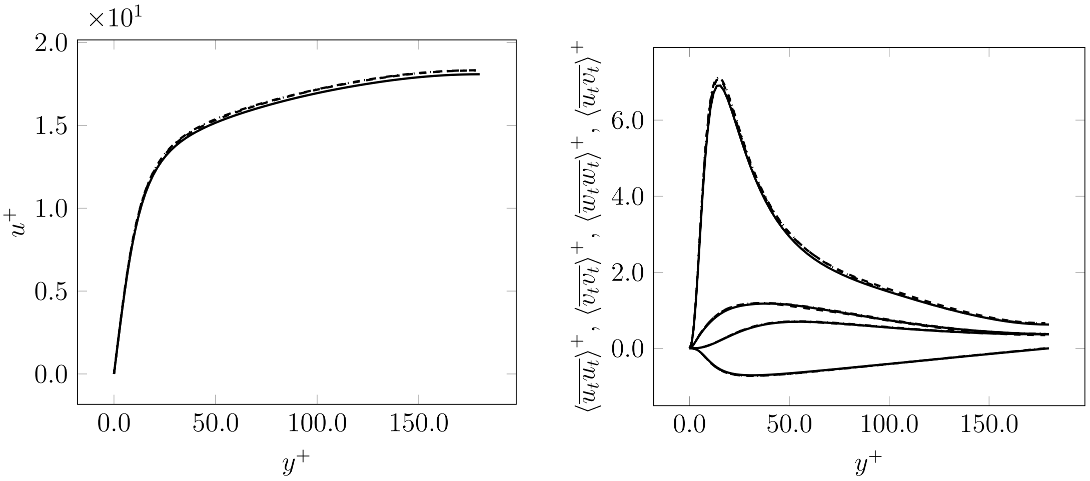

Figure 3.4: Left: Mean velocity in plus units. Right: Comparison between velocity variances. Solid, dashed and dash-dot curves indicate the results of Kim et al. (1987), Moser et al. (1999) and Incompact3d respectively.

Fig. 3.5b compares the energy terms calculated via Incompact3d (solid line) and their counterparts presented by Mansour et al. (1988) (circles). A good agreement between the two results is obtained.

The second version of the equation for the turbulent kinetic energy budget differs from the first one in the presence of the two terms dissipation ε and work of turbulent viscous shear ($WTVS$) which subtracted are equal to the difference of the pseudo dissipation $\widetilde{\varepsilon}$ and viscous diffusion:

$$-\frac{1}{2}\frac{\mathrm{d}}{\mathrm{d}y}\left\langle\overline{v_t({u_t}^2+{v_t}^2+{w_t}^2)}\right\rangle-\langle\overline{u_t v_t}\rangle\frac{\mathrm{d}\langle\overline{u}\rangle}{\mathrm{d}y}+WTVS-\frac{\mathrm{d}}{\mathrm{d}y}\langle\overline{p_t v_t}\rangle-\varepsilon=0, \tag{3.5}$$

where the dissipation and $WTVS$ are expressed as

$$\begin{aligned}\varepsilon=&\frac{1}{Re_p}\Big[\Big\langle\overline{2\Big(\frac{\partial u_t}{\partial x}\Big)^2}+\overline{2\Big(\frac{\partial v_t}{\partial y}\Big)^2}+\overline{2\Big(\frac{\partial w_t}{\partial z}\Big)^2}+\\&+\overline{\Big(\frac{\partial u_t}{\partial y}+\frac{\partial v_t}{\partial x}\Big)^2}+\overline{\Big(\frac{\partial u_t}{\partial z}+\frac{\partial w_t}{\partial x}\Big)^2}+\overline{\Big(\frac{\partial v_t}{\partial z}+\frac{\partial w_t}{\partial y}\Big)^2}\Big\rangle\Big],\end{aligned} \tag{3.6}$$

$$WTVS=\frac{1}{Re_p}\frac{\mathrm{d}}{\mathrm{d}y}\left[\left\langle\overline{u_t\left(\frac{\partial u_t}{\partial y}+\frac{\partial v_t}{\partial x}\right)+2v_t\left(\frac{\partial v_t}{\partial y}\right)+w_t\left(\frac{\partial v_t}{\partial z}+\frac{\partial w_t}{\partial y}\right)}\right\rangle\right]. \tag{3.7}$$

In 3.6 the difference between $WTVS$ and ε is compared to that of the corresponding terms of Pope's equation to check the correctness of the energy calculation: both curves overlap except a small difference at the first two points along y due to the use of a lower order scheme for gradients at wall.

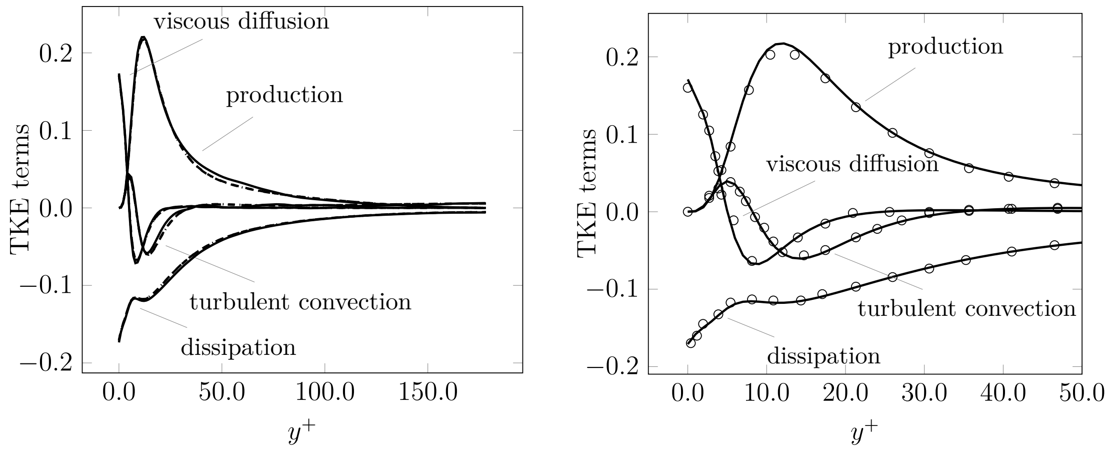

Figure 3.5: Left: Turbulent kinetic energy terms convergence. Solid, dashed and dash-dot lines corresponds to an interval $t_f - t_i$ of 250, 500 and 1000 time units respectively. Right: Comparison between the terms of (3.3) showed by Mansour et al. (1988) (circles) and Incompact3d (solid lines).

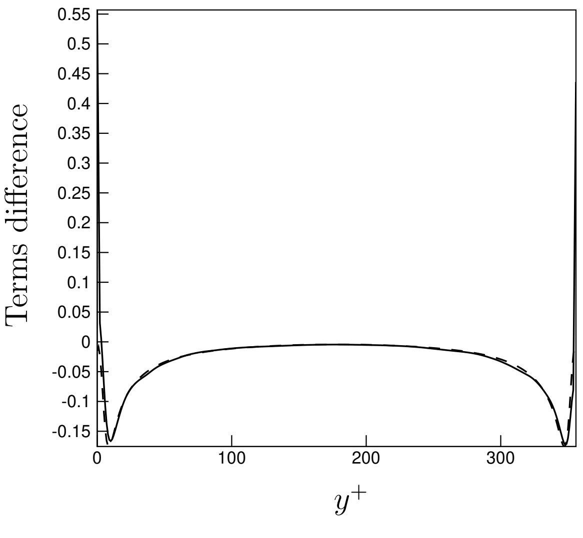

Figure 3.6: Comparison between corresponding terms of the two equations: $WTVS-\varepsilon$ (solid), $\frac{1}{Re_p}\frac{\mathrm{d}^2\langle\mathcal{K}\rangle}{\mathrm{d}y^2} - \widetilde{\varepsilon}$ (dashed).

3.1.2 Resolution $230 \times 129 \times 460$, time step $\Delta t = 2.5 \times 10^{-3}$

We performed a further simulation by increasing the streamwise and spanwise resolution and using an halved time step $\Delta t = 2.5 \times 10^{-3}$ because of the stability constraints due to the explicit time advancement of Incompact3d.

Fig. 3.7 shows the history of x and z averaged quantities of interest. The gradient of the streamwise velocity at wall is showed in fig. 3.7b to check if the simulation reached a developed turbulent state. The gradient begins to oscillate around a value of 3.0 after a brief transient which lasts approximately 250 time units or 100000 time steps.

Fig. 3.8 represents the value of Re_τ computed by considering an increasing number of fields to average in time. The computation of the time average begins from the $200,000$ time step corresponding to 500 time units. The friction Reynolds number approaches a value $Re_\tau = 178.5$ slightly higher than the one (178.2) of the less resolved case studied in section 3.1.1.

Fig. 3.9a, 3.9b,3.10a show comparisons of streamwise mean velocity, turbulent velocities correlations and the terms of energy equation for the two cases at different resolutions. The results agrees indicating that the resolution used in section 3.1.1 is sufficient to resolve the space scales of the flow.

3.2 Pressure verification with IBM

We mainly focus on pressure drag reduction hence it is crucial to evaluate the accuracy of the computed pressure. We consider a smooth turbulent channel and a channel with a bump as test cases: in both problems solid walls are modeled using the $\mathring{\mathbf{U}} = \mathbf{0}$ IBM strategy.

3.2.1 Channel flow

The geometry of the channel is depicted in fig. 3.11. The sizes of the computational domain along the streamwise, the vertical and the spanwise direction are $L_x^* = 8\delta^*$, $L_y^* = 2.4\delta^*$ and $L_z^* = \pi\delta^*$ respectively. For this simulation we have $Re_p = 4200$ and $\Delta t = 5.0 \times 10^{-4}$.

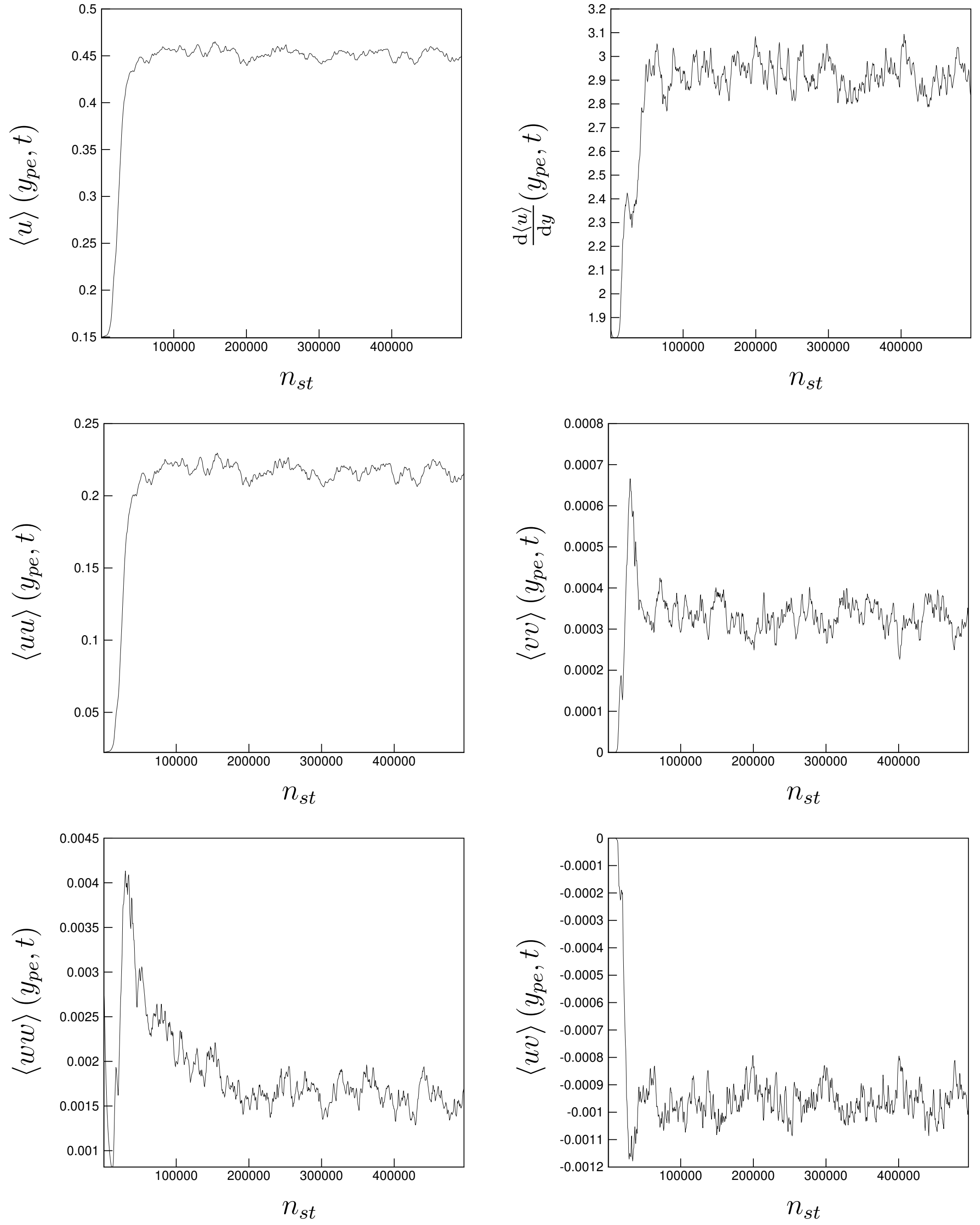

Figure 3.7: Plane averaged quantities at $y_{pe} = 8.05 \times 10^{-2}$, the location of the maximum root mean square value of the streamwise turbulent velocity. n_{st} indicates the number time steps corresponding to the current time t.

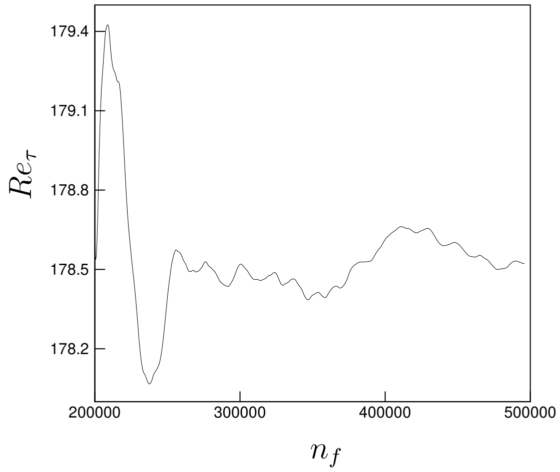

Figure 3.8: Re_τ dependence on time. n_f indicates the number of the iteration corresponding to t_f, the final instant used for calculating time average.

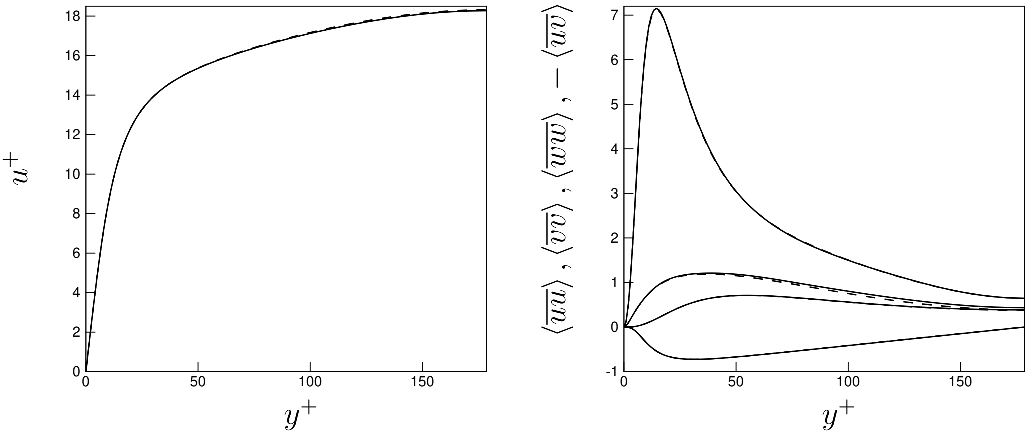

Figure 3.9: Left: Streamwise mean velocity comparison between the results obtained with the higher (solid) and the lower (dashed) resolution simulations. Right: variances comparisons between results obtained with the higher (solid) and the lower (dashed) resolution simulations

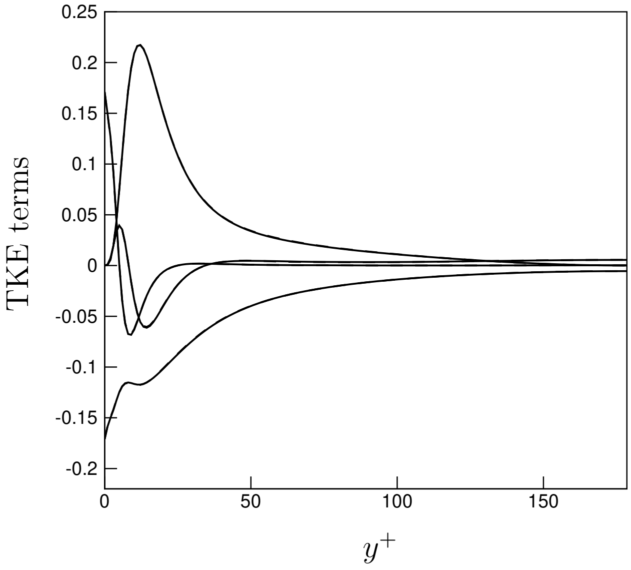

Figure 3.10: Left: Energy terms comparison between two different resolution cases

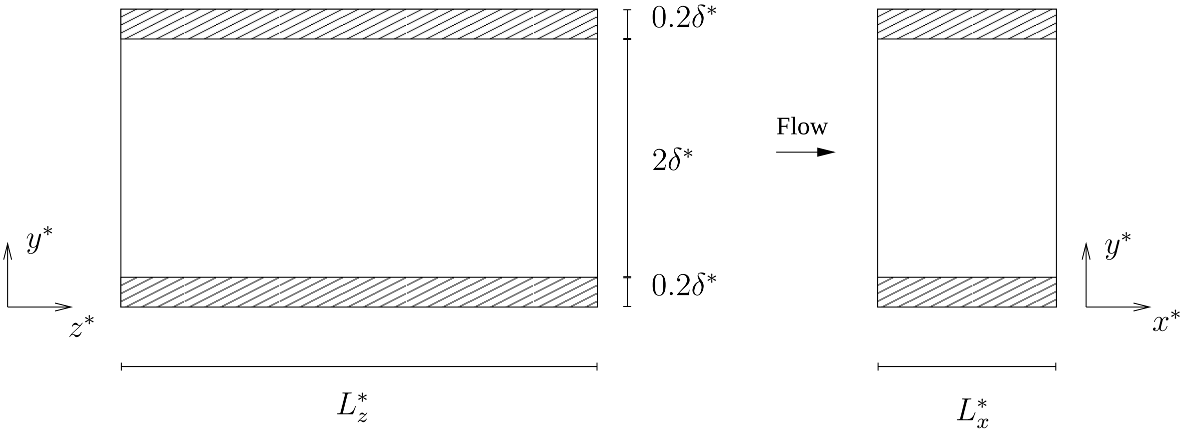

Figure 3.11: Geometrical configuration of the smooth turbulent channel. x^*, y^* and z^* are the streamwise, normal and spanwise coordinates.

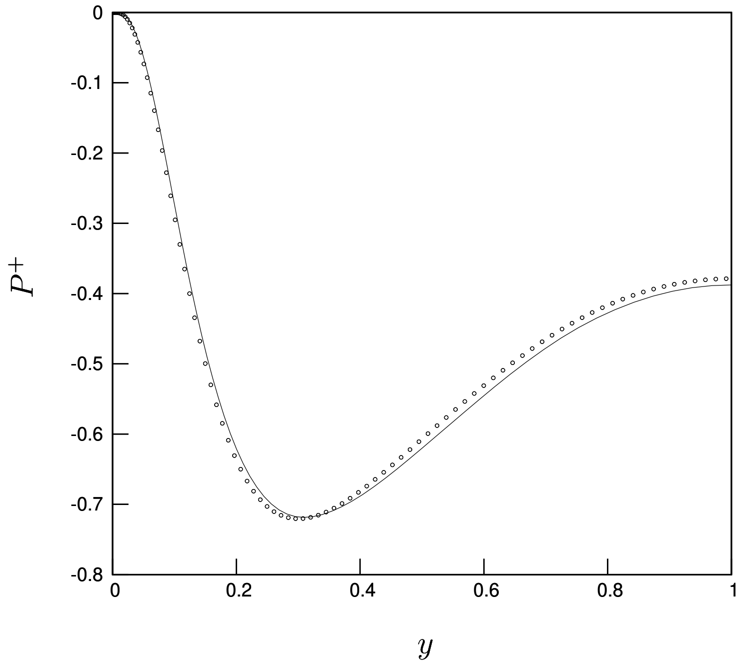

Figure 3.12: Comparison between Incompact3d (solid line) result with IBM and Lee and Moser (2015) (circles). The normal coordinate y has origin at the wall surface where the reference pressure is set to a value which ensures a null pressure.

Fig. 3.12 shows the computed pressure field in viscous units compares well with the result presented by Lee and Moser (2015).

3.2.2 Channel with hills

We simulate a turbulent channel flow with a constriction as depicted in fig. 3.13a. The size of the computational domain along the streamwise, vertical and spanwise directions are $L_x^* = 9.0h^*$, $L_y^* = 3.036h^*$ and $L_z^* = 4.5h^*$ respectively, where h^* is the height of the obstacle.

The pressure obtained via Incompact3d is compared to the result of Breuer et al. (2009) in fig. 3.13b. A good agreement is shown in the two regions $0 \leq x \leq 3.5$ and $8.0 \leq x \leq 9.0$ while a small discrepancy appears in the remaining part of the x range resulting in an overestimation of the pressure peak. This difference is probably due to the different type of numerical methods used for the two simulations furthermore our results were obtained using the $\mathbf{U}^* = \mathbf{0}$ IBM without any interpolation or smoothing.

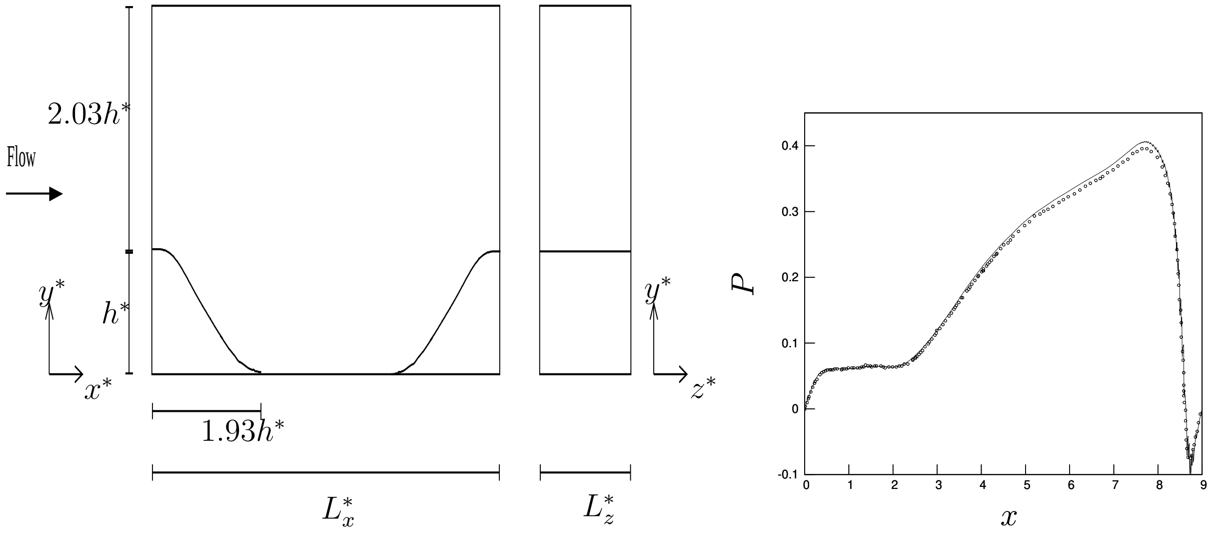

Figure 3.13: Left: Configuration of the channel with hills. The cartesian coordinates along the streamwise, vertical and spanwise directions are x^*, y^* and z^*. Right: Comparison between Incompact3d (solid line) result with IBM and Breuer et al. (2009) (circles).

3.3 Channel with square bars

A simulation of a turbulent channel with bars lying on the walls (refer to fig. 3.14) is performed. This problem is challenging because of shear stress and pressure singularities the fluid experiences nearby concave corners (Moffatt, 1964; Burda et al., 2012). Traditional resolution studies evaluate quantities of interest using different grids to ascertain the obtained solution is grid independent. Unfortunately, no numerical method is able to compute infinite values and refining the grid would not give acceptable results. The analysis of Moffatt (1964) shows that pressure and shear stress near a corner are proportional to $1/r^{\alpha}$ (where r is the distance from the corner and $0 < \alpha < 1$) and integrable. The drag in a separated flows involves integrals along the wall therefore an integrable shear stress and pressure implies finite values for drag.

Firstly, we present the drag coefficient obtained using the $\mathring{\mathbf{U}} = \mathbf{0}$ IBM as the Lagrange IBM caused a numerical instability even for very small time steps. Secondly, we use the code Nek5000 to simulate the same flow and we compare the drag coefficients obtained with SEM with the ones obtained via the IBM.

3.3.1 Flow configuration

We study the turbulent channel flow depicted in figure 3.14, where two identical square bars are located on the opposite walls. The boundary conditions are periodic over the streamwise and spanwise directions, while the no-slip condition is imposed on the solid walls. Dimensional quantities are indicated with an asterisk.

The Cartesian coordinates are x^*, y^* and z^* along the the streamwise, vertical and spanwise direction respectively, where x^* is defined from the upstream start of the computational domain and y^* is defined from the bottom channel wall. The initial condition is of zero velocity in the two strips between the square bars, $0 < y^* < h^*$ and $2\delta^* + h^* < y^* < 2(\delta^* + h^*)$ and a laminar Poiseuille flow plus a random three dimensional perturbation velocity field of zero mean in $h^* < y^* < 2\delta^* + h^*$. The midline velocity of this Poiseuille flow is U_p^* while the bulk velocity is $2/3U_p^*$.

All the variables are scaled using half of the distance between the bar crests δ^* and U_p^*. The Reynolds number is $Re_p = U_p^*\delta^*/\nu^* = 4200$ where ν^* is the kinematic viscosity of the fluid. The simulations are performed at a constant mass flow rate. The components of the velocity vector along x^*, y^* and z^* are indicated by u^*, v^* and w^* respectively. The pressure p^* is scaled using the density ρ^* as $p = p^*/(\rho^* U_p^{*2})$, and is defined as $p(x, y, z, t) = \phi(x, y, z, t) + \Pi_x(t)\, x + \Pi_z(t)\, z$, where ϕ is a periodic function of x and z, Π_x is the streamwise mean pressure gradient, and Π_z is the oscillating spanwise pressure gradient.

The dimensions of the computational domain are $L_x = 8$, $L_y = 2.4$ and $L_z = \pi$, where the subscripts denote the Cartesian coordinates. We point out that an analysis about the dependence of the results on the lengths of the computational domain L_x and L_z is not conducted because we intend to model an infinitely long channel with periodic arrangement of the bars. This is a limitation of this study because, even if the geometry is periodic in the main flow direction, the real turbulent flow might be different due to Floquet-type instabilities. Each square bar has size $h = 0.2$ along the x and y directions and the center of each bar is located at $x = 4$. The time t^* is scaled as $t = t^* U_p^*/\delta^*$.

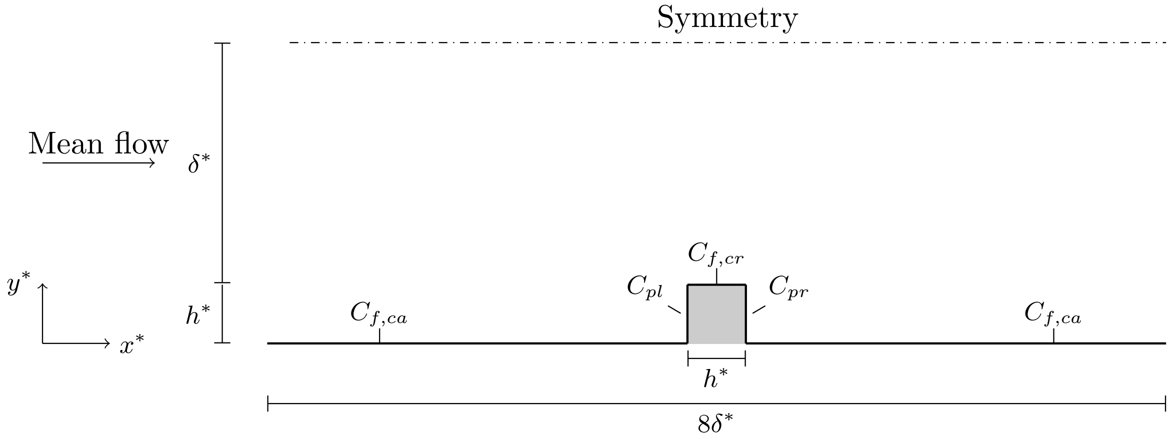

Figure 3.14: Sketch of the system configuration. The bar is indicated by the grey square and a drag coefficient is assigned to every surface. Only the bottom half of the domain is shown. The dash-dotted line represents the symmetry plane at $y^* = \delta^* + h^*$. The height of the bar is $h^* = 0.2\delta^*$.

3.3.2 Drag components

For a separated flow the drag is composed of a pressure drag P_d^* and a skin-friction drag F^*, defined as

$$P_d^* = \int_{S^*} p^* \, \mathbf{n} \cdot \mathbf{i} \, \mathrm{d}S, \qquad F^* = -\int_{S^*} \mu^* \frac{\partial u^*}{\partial \mathbf{n}^*}\Big|_w \mathrm{d}S, \tag{3.8}$$

where $\mathbf{n}$ is the normal unit vector pointing outside the fluid domain, $\mathbf{i}$ is the unit vector along x direction and S^* is the wall surface.

Only for the vertical surfaces of the bar $\mathbf{n} \cdot \mathbf{i} \neq 0$, and therefore the pressure drag is

$$P_d^* = \int_{S_l^*} p^* \, \mathbf{n} \cdot \mathbf{i} \, \mathrm{d}S + \int_{S_r^*} p^* \, \mathbf{n} \cdot \mathbf{i} \, \mathrm{d}S = \int_{S_l^*} p^* \, \mathrm{d}S - \int_{S_r^*} p^* \, \mathrm{d}S, \tag{3.9}$$

where S_l^* and S_r^* are the left and right vertical surfaces of the bar of area $h^* L_z^*$ and the minus is due to the orientation of $\mathbf{n}$. Equation (3.9) can be written by isolating the contributions of the pressure on the left and right vertical surfaces of the bar

$$P_d^* = P_l^* + P_r^* \tag{3.10a}$$

$$P_l^* = \int_{S_l^*} p^* \, \mathbf{n} \cdot \mathbf{i} \, \mathrm{d}S = \int_{S_l^*} p^* \, \mathrm{d}S, \quad P_r^* = \int_{S_r^*} p^* \, \mathbf{n} \cdot \mathbf{i} \, \mathrm{d}S = -\int_{S_r^*} p^* \, \mathrm{d}S. \tag{3.10b}$$

We point out that P_l^* and P_r^* defined (3.10) are not pressure drag components as the pressure drag is due to the difference of the integrals in (3.9) and there is not pressure drag on the left or right vertical surfaces of the bar. P_l^* and P_r^* are rather the mathematical fluxes of the field $p^*\mathbf{i}$ along the vertical surfaces of the bar and their sum gives the pressure drag P_d^*.

The skin-friction drag is

$$F^* = F_{ca}^* + F_{cr}^* = \int_{S_{ca}^*} \mu^* \frac{\partial \overline{u^*}}{\partial y^*}\bigg|_0 \mathrm{d}S + \int_{S_{cr}^*} \mu^* \frac{\partial \overline{u^*}}{\partial y^*}\bigg|_{h^*} \mathrm{d}S, \tag{3.11}$$

where S_{ca}^* and S_{cr}^* are the cavity and crest surfaces, respectively. Note P_l^*, P_r^*, F_{ca}^* and F_{cr}^* include contributions from the bottom and top walls.

We define a cavity (C_{ca}), a crest (C_{cr}) drag coefficients and the left (C_{pl}) and right (C_{pr}) coefficients of the flux of $p^*\mathbf{i}$ by dividing F_{ca}^*, F_{cr}^*, P_l^* and P_r^* by $\rho^* U_p^{*2} L_x^* L_z^*$, respectively. The skin-friction coefficient is composed by the crest and the cavity drag coefficients, i.e. $C_f = C_{f,cr} + C_{f,ca}$ and the pressure drag coefficient is given by $C_p = C_{pl} + C_{pr}$.

3.3.3 Comparison between Incompact3d and Nek5000

Fig. 3.15a represents $\mathcal{UB}(\%) = 100\left|1 + \frac{C_p(t)+C_f(t)}{\Pi_x(t)L_y}\right|$ against time obtained via Incompact3d and Nek5000. The percentage of unbalance $\mathcal{UB}(\%)$ is zero at any time t if the conservation of momentum in the streamwise direction is verified exactly (refer to appendix B). High values of $\mathcal{UB}(\%)$ indicate that the streamwise pressure gradient and the sum of pressure and skin-friction drag give two different values for the total drag creating a dilemma about the choice of the appropriate method to measure it. $\mathcal{UB}(\%)$ obtained with Incompact3d is greater than 1% for most of the time, while nek5000 is superior because it maintains the level $\mathcal{UB}(\%)$ lower than 0.2%.

Tables 3.1 and 3.2 show the variations of the drag coefficients as a function of the grid resolution for Incompact3d and Nek5000 respectively. Incompact3d predicts a value of $C_{f,cr}$ about one third lower (-3.18×10^{-5}) than the one obtained using the other code (-1.10×10^{-4}).

From these tests, we conclude that Nek5000 satisfies satisfactorily the drag balance (B.7a) giving an unambiguous value for the total drag and furnishes more reliable values of $C_{f,cr}$ and than the ones obtained via Incompact3d. Because of these reasons, we choose the SEM to analyze the turbulent channel with bars controlled by a spanwise oscillating pressure gradient in chapter 5.

$n_x \times n_y \times n_z$	$-\Pi_x\, L_y(\times 10^{-2})$	$C_{f,cr}(\times 10^{-5})$	$C_{f,ca}(\times 10^{-3})$	$C_p(\times 10^{-3})$
$1600 \times 241 \times 96$	1.04	−3.18	1.96	8.20
$3200 \times 241 \times 96$	1.04	−3.19	2.01	8.13
$1600 \times 481 \times 96$	1.04	−2.97	1.99	8.43

Table 3.1: Resolution checks for the drag components obtained with Incompact3d. $-\Pi_x\, L_y$ is the total drag coefficient calculated measuring the mean streamwise pressure gradient Π_x.

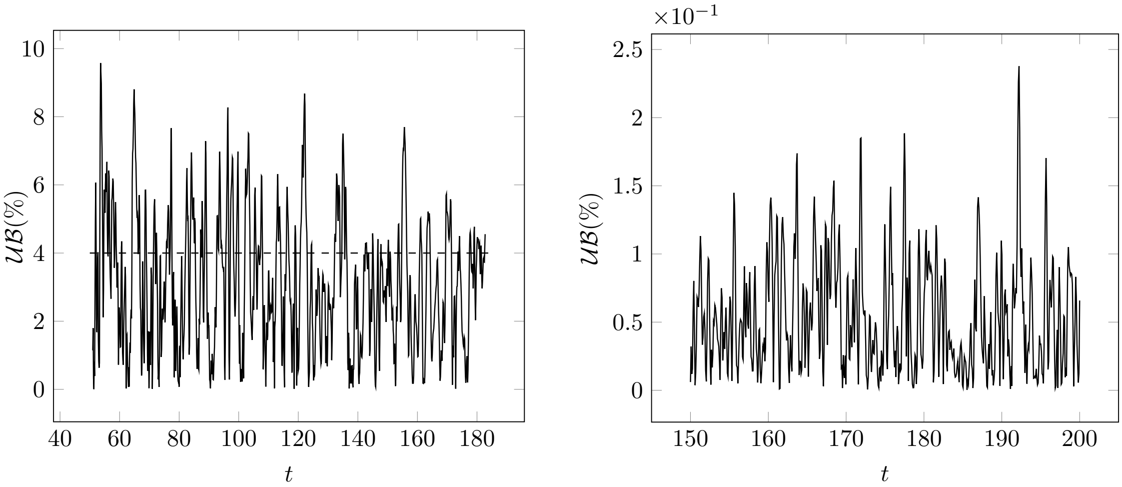

Figure 3.15: Left: percentage of drag unbalance $\mathcal{UB}(\%) = 100\left|1 + \frac{C_p(t)+C_f(t)}{\Pi_x(t)L_y}\right|$ as function of time t for Incompact3d (left) and Nek5000 (right). Dashed line indicates $\mathcal{UB}(\%) = 4\%$.

l_x	$-\Pi_x\, L_y(\times 10^{-2})$	$C_{f,cr}(\times 10^{-4})$	$C_{f,ca}(\times 10^{-3})$	$C_p(\times 10^{-3})$
6	1.00	−1.10	2.01	8.11
8	0.99	−1.12	1.99	8.08
10	1.01	−1.11	2.00	8.22

Table 3.2: Resolution checks for the drag components with Nek5000. $-\Pi_x\, L_y$ is the total drag coefficient computed by measuring the mean streamwise pressure gradient Π_x.

Chapter 4

Laminar flow

Previous studies (Ricco and Quadrio, 2008; Quadrio and Ricco, 2011; Ricco and Hahn, 2013) showed that useful information about turbulence control can be extracted from laminar solutions. Our aim is to control the flow around square bars lying at the walls of a channel and, therefore we apply the same strategy for this separation problem. We consider the phase and z averaged spanwise momentum equation for the turbulent flow

$$\begin{aligned}\frac{\partial \langle \widehat{w} \rangle}{\partial \tau} + \frac{\partial \langle \widehat{uw} \rangle}{\partial x} + \frac{\partial \langle \widehat{vw} \rangle}{\partial y} =& - \frac{1}{L_z} \left[\widehat{p}(x,y,L_z,\tau) - \widehat{p}(x,y,0,\tau) \right] + \\ & + \frac{1}{Re_p} \left(\frac{\partial^2 \langle \widehat{w} \rangle}{\partial x^2} + \frac{\partial^2 \langle \widehat{w} \rangle}{\partial y^2} \right),\end{aligned} \tag{4.1}$$

where

$$- \frac{1}{L_z} \left[\widehat{p}(x,y,L_z,\tau) - \widehat{p}(x,y,0,\tau) \right] = - \frac{\partial \langle \widehat{p} \rangle}{\partial z} = - \frac{1}{L_z} \int_0^{L_z} \frac{\partial \widehat{p}}{\partial z} \mathrm{d}z. \tag{4.2}$$

Substituting the pressure $p = \phi + \Pi_x \, x + \Pi_z \, z$, the Reynolds decomposition $w = \langle \widehat{w} \rangle + w_t$ and the z-averaged continuity equation

$$\frac{\partial \langle \widehat{u} \rangle}{\partial x} + \frac{\partial \langle \widehat{v} \rangle}{\partial y} = 0 \tag{4.3}$$

into (4.1) leads to

$$\frac{\partial \langle \widehat{w} \rangle}{\partial \tau} = \frac{1}{Re_p} \left(\frac{\partial^2 \langle \widehat{w} \rangle}{\partial x^2} + \frac{\partial^2 \langle \widehat{w} \rangle}{\partial y^2} \right) - \Pi_z - \langle \widehat{u} \rangle \frac{\partial \langle \widehat{w} \rangle}{\partial x} - \langle \widehat{v} \rangle \frac{\partial \langle \widehat{w} \rangle}{\partial y} - \frac{\partial \langle \widehat{u_t w_t} \rangle}{\partial x} - \frac{\partial \langle \widehat{v_t w_t} \rangle}{\partial y}. \tag{4.4}$$

Equation (4.4) is the relationship governing the spanwise motion of the turbulent flow. The laminar auxiliary problem can be found by neglecting the Reynolds stress $\partial\left\langle\widehat{u_t w_t}\right\rangle/\partial x$ and $\partial\left\langle\widehat{v_t w_t}\right\rangle/\partial y$ and using $\langle\overline{u}\rangle(x,y)$ and $\langle\overline{v}\rangle(x,y)$ of the turbulent uncontrolled flow in place of $\langle\widehat{u}\rangle$ and $\langle\widehat{v}\rangle$ for the controlled flow

$$\frac{\partial w_l}{\partial \tau}=\frac{1}{Re_p}\left(\frac{\partial^2 w_l}{\partial x^2}+\frac{\partial^2 w_l}{\partial y^2}\right)-\Pi_z-\left(\langle\overline{u}\rangle\frac{\partial w_l}{\partial x}+\langle\overline{v}\rangle\frac{\partial w_l}{\partial y}\right). \tag{4.5}$$

It should be recognized that the limitations of this procedure are that the Reynolds stress are not negligible in the turbulent flow (refer to figure 5.11 in section 5.7) and that the uncontrolled velocities $\langle\overline{u}\rangle(x,y)$ and $\langle\overline{v}\rangle(x,y)$ are different from their controlled counterparts.

4.1 Modes equations

We assume that w_l is a periodic function of τ and thus Fourier series expansions can be employed. The quantities Π_z and w_l are expressed as

$$w_l=\sum_{n=-\infty}^{+\infty}\frac{1}{2}\,\widehat{w}_n(x,y)\,e^{in\omega_T\tau},\qquad \Pi_z=A\cos(\omega_T\tau)=\frac{1}{2}A\left(e^{i\omega_T\tau}+e^{-i\omega_T\tau}\right), \tag{4.6}$$

where $\omega_T=2\pi/T$. The substitution of (4.6) into (4.5) leads to

$$\begin{aligned}\sum_{n=-\infty}^{+\infty}\frac{1}{2}\,(i\,n\,\omega_T)\,\widehat{w}_n-\frac{1}{Re_p}\left(\frac{\partial^2\widehat{w}_n}{\partial x^2}+\frac{\partial^2\widehat{w}_n}{\partial y^2}\right)+\langle\overline{u}\rangle\frac{\partial\widehat{w}_n}{\partial x}+\langle\overline{v}\rangle\frac{\partial\widehat{w}_n}{\partial y}e^{i\,n\,\omega_T\,\tau}=\\ -\frac{1}{2}\,A\left(e^{i\,\omega_T\,\tau}+e^{-i\,\omega_T\,\tau}\right).\end{aligned} \tag{4.7}$$

Each mode $\widehat{w}_n$ satisfies:

$$i\,n\,\omega_T\widehat{w}_n=\frac{1}{Re_p}\left(\frac{\partial^2\widehat{w}_n}{\partial x^2}+\frac{\partial^2\widehat{w}_n}{\partial y^2}\right)-\langle\overline{u}\rangle\frac{\partial\widehat{w}_n}{\partial x}-\langle\overline{v}\rangle\frac{\partial\widehat{w}_n}{\partial y}\qquad n\neq\pm1 \tag{4.8a}$$

and

$$(\pm i\,\omega_T)\,\widehat{w}_{\pm1}=\frac{1}{Re_p}\left(\frac{\partial^2\widehat{w}_{\pm1}}{\partial x^2}+\frac{\partial^2\widehat{w}_{\pm1}}{\partial y^2}\right)-\langle\overline{u}\rangle\frac{\partial\widehat{w}_{\pm1}}{\partial x}-\langle\overline{v}\rangle\frac{\partial\widehat{w}_{\pm1}}{\partial y}-A. \tag{4.8b}$$

The boundary conditions for (4.8b) are

$$\widehat{w}_{\pm1}(0,y)=\widehat{w}_{\pm1}(h,y)=0,\qquad 0\le y\le h, \tag{4.9a}$$

$$\widehat{w}_{\pm 1}(x,h) = \widehat{w}_{\pm 1}(x,0) = 0, \qquad h \le x \le L_x, \tag{4.9b}$$

$$\widehat{w}_{\pm 1}(h,y) = 0, \qquad 0 \le y \le h, \tag{4.9c}$$

$$\frac{\partial \widehat{w}_{\pm 1}}{\partial y}(x,1+h) = 0, \qquad 0 \le x \le L_x, \tag{4.9d}$$

$$\widehat{w}_{\pm 1}(0,y) = \widehat{w}_{\pm 1}(L_x,y), \qquad 0 \le y \le 1+h, \tag{4.9e}$$

condition (4.9a), (4.9b), (4.9c) are no-slip conditions at the walls, condition (4.9d) expresses the symmetry along the centerline and (4.9e) denotes the periodicity along x.

The only non-null modes are those for which $n = \pm 1$ and from (4.6) it follows that

$$w_l(x,y,\tau) = \frac{1}{2}\left(\widehat{w}_1\, e^{i\,\omega_T\,\tau} + \widehat{w}_{-1}\, e^{-i\,\omega_T\,\tau}\right). \tag{4.10}$$

The spanwise velocity $w_l(x,y,\tau)$ is real and thus $\widehat{w}_1 = \widehat{w}_{-1}^{cc}$ because of the Hermitian property (cc indicates the complex conjugate).

In order to eliminate the non-homogeneous term $-A$ from (4.8b), we introduce $\widetilde{w}_1(x,y) = \widehat{w}_1(x,y) - Ai/\omega_T$, which transforms (4.8b) into

$$\frac{\partial^2 \widetilde{w}}{\partial x^2} + \frac{\partial^2 \widetilde{w}}{\partial y^2} - i\,\omega_T\, Re_p \widetilde{w} - Re_p\left(\langle \overline{u} \rangle \frac{\partial \widetilde{w}}{\partial x} + \langle \overline{v} \rangle \frac{\partial \widetilde{w}}{\partial y}\right) = 0. \tag{4.11}$$

The boundary conditions for eq. (4.11) are

$$\widetilde{w}(0,y) = \widetilde{w}(h,y) = -\frac{A}{\omega_T}\, i, \qquad 0 \le y \le h, \tag{4.12a}$$

$$\widetilde{w}(x,h) = \widetilde{w}(x,0) = -\frac{A}{\omega_T}\, i, \qquad h \le x \le L_x, \tag{4.12b}$$

$$\widetilde{w}(h,y) = -\frac{A}{\omega_T}\, i, \qquad 0 \le y \le h, \tag{4.12c}$$

$$\frac{\partial \widetilde{w}}{\partial y}(x,1+h) = 0, \qquad 0 \le x \le L_x, \tag{4.12d}$$

$$\widetilde{w}(0,y) = \widetilde{w}(L_x,y), \qquad 0 \le y \le 1+h. \tag{4.12e}$$

4.2 Numerical solution procedure

Eq. (4.11) is discretized by using centered finite differences

$$\widetilde{w}_{a,b} = C_{a,b}\, \widetilde{w}_{a,b-1} + D_{a,b}\, \widetilde{w}_{a-1,b} + F_{a,b}\, \widetilde{w}_{a+1,b} + G_{a,b}\, \widetilde{w}_{a,b+1}, \tag{4.13}$$

where $C_{a,b}$,$D_{a,b}$,$F_{a,b}$ and $G_{a,b}$ depend on the streamwise and normal velocities because of advective terms in equation (4.5)

$$C_{a,b} = \frac{\frac{1}{\Delta y^2} + \frac{Re_p}{2\Delta y}\, v_{a,b}}{i\,\omega_T\, Re_p + \frac{2}{\Delta x^2} + \frac{2}{\Delta y^2}}, \qquad D_{a,b} = \frac{\frac{1}{\Delta x^2} + \frac{Re_p}{2\Delta x}\, u_{a,b}}{i\,\omega_T\, Re_p + \frac{2}{\Delta x^2} + \frac{2}{\Delta y^2}}, \tag{4.14a}$$

$$F_{a,b} = \frac{\frac{1}{\Delta x^2} - \frac{Re_p}{2\Delta x}\, u_{a,b}}{i\,\omega_T\, Re_p + \frac{2}{\Delta x^2} + \frac{2}{\Delta y^2}}, \qquad G_{a,b} = \frac{\frac{1}{\Delta y^2} - \frac{Re_p}{2\Delta y}\, v_{a,b}}{i\,\omega_T\, Re_p + \frac{2}{\Delta x^2} + \frac{2}{\Delta y^2}}, \tag{4.14b}$$

where a, b subscripts are the indices of the grid points, Δx and Δy are the finite increments along x and y. The boundary conditions (4.12a)-(4.12e) are written as

$$\widetilde{w}_{1,b} = \widetilde{w}_{l,b} = -\frac{A}{\omega}\, i, \qquad 1 \le b \le m, \tag{4.15a}$$

$$\widetilde{w}_{a,m} = \widetilde{w}_{a,1} = -\frac{A}{\omega}\, i, \qquad l \le a \le n_x, \tag{4.15b}$$

$$\widetilde{w}_{l,b} = -\frac{A}{\omega}\, i, \qquad 1 \le b \le m, \tag{4.15c}$$

$$\widetilde{w}_{a,n_y+1} = \widetilde{w}_{a,n_y-1}, \qquad 1 \le a \le n_x, \tag{4.15d}$$

$$\widetilde{w}_{0,b} = \widetilde{w}_{n_x-1,b}, \qquad 1 \le b \le n_y \qquad \widetilde{w}_{n_x,b} = \widetilde{w}_{1,b} \qquad 1 \le b \le n_y, \tag{4.15e}$$

Fig. (4.1) shows the points in the computational domain marked with different symbols. The scheme (4.13) is applied to the interior points indicated by filled circles while no equations are written for points corresponding to the bar, the vertical line at $i = n_x$ and the wall (cross symbol). The equation (4.13) is modified near boundaries to take into account the boundary conditions (4.15a)-(4.15e)

- $\widetilde{w}_{0,b} = \widetilde{w}_{n_x-1,b}$ (squares)

$$\begin{aligned} \widetilde{w}_{1,b} =& C_{1,b}\, \widetilde{w}_{1,b-1} + D_{1,b}\, \widetilde{w}_{n_x-1,b} + F_{1,b}\, \widetilde{w}_{2,b} + G_{1,b}\, \widetilde{w}_{1,b+1}, \\ & m+1 \le \; b \le n_y - 1 \end{aligned} \tag{4.16}$$

- $\widetilde{w}_{a,n_y+1} = \widetilde{w}_{a,ny-1}$ (triangles)

$$\begin{aligned} \widetilde{w}_{a,n_y} =& C_{a,n_y}\, \widetilde{w}_{a,n_y-1} + D_{a,n_y}\, \widetilde{w}_{a-1,n_y} + F_{a,n_y}\, \widetilde{w}_{a+1,n_y} + G_{a,n_y}\, \widetilde{w}_{a,ny-1} \\ & 2 \le a \le n_x - 2 \end{aligned} \tag{4.17}$$

- $\widetilde{w}_{n_x,b} = \widetilde{w}_{1,b}$ (empty circles)

$$\begin{aligned}\widetilde{w}_{n_x-1,b} =& C_{n_x-1,b}\,\widetilde{w}_{n_x-1,b-1} + D_{n_x-1,b}\,\widetilde{w}_{n_x-2,b} + F_{n_x-1,b}\,\widetilde{w}_{1,b} + \\ & G_{n_x-1,b}\,\widetilde{w}_{n_x-1,b+1} \qquad 3 \leq\ b \leq n_y - 1\end{aligned} \tag{4.18}$$

The points identified by the indices $(1, n_y)$, $(n_x - 1, 2)$ and $(n_x - 1, n_y)$ are not marked because two boundary conditions apply for them

- point $(1, n_y)$ $\quad (\widetilde{w}_{1,n_y+1} = \widetilde{w}_{1,n_y-1},\ \widetilde{w}_{0,n_y} = \widetilde{w}_{n_x-1,n_y})$

$$\widetilde{w}_{1,n_y} = C_{1,n_y}\,\widetilde{w}_{1,n_y-1} + D_{1,n_y}\,\widetilde{w}_{n_x-1,n_y} + F_{1,n_y}\,\widetilde{w}_{2,n_y} + G_{1,n_y}\,\widetilde{w}_{1,n_y-1} \tag{4.19}$$

- point $(n_x - 1, 2)$ $\quad \widetilde{w}_{n_x-1,1} = -\frac{A}{\omega_T}\,i, \widetilde{w}_{n_x,2} = \widetilde{w}_{1,2}$

$$\widetilde{W}_{n_x-1,2} = -C_{n_x-1,2}\,\frac{A}{\omega_T} + D_{n_x-1,2}\,\widetilde{w}_{n_x-2,2} + F_{n_x-1,2}\,\widetilde{w}_{1,2} + G_{n_x-1,2}\,\widetilde{w}_{n_x-1,3} \tag{4.20}$$

- point $(n_x - 1, n_y)$ $\quad \widetilde{w}_{n_x-1,n_y+1} = \widetilde{w}_{n_x-1,n_y-1},\ \widetilde{w}_{n_x,n_y} = \widetilde{w}_{1,n_y}$

$$\begin{aligned}\widetilde{w}_{n_x-1,n_y} =& C_{n_x-1,n_y}\,\widetilde{w}_{n_x-1,n_y-1} + D_{n_x-1,n_y}\,\widetilde{w}_{n_x-2,n_y} + F_{n_x-1,n_y}\,\widetilde{w}_{1,n_y} + \\ & G_{n_x-1,n_y}\,\widetilde{w}_{n_x-1,n_y-1}\end{aligned} \tag{4.21}$$

The system obtained is solved via a successive over-relaxation (SOR) method

$$\widetilde{w}^{new}_{a,b} = \widetilde{w}_{a,b} + \alpha\, r_{a,b}, \tag{4.22}$$

where the residual is defined as

$$r_{a,b} = C_{a,b}\,\widetilde{w}_{a,b-1} + D_{a,b}\,\widetilde{w}_{a-1,b} + F_{a,b}\,\widetilde{w}_{a+1,b} + G_{a,b}\,\widetilde{w}_{a,b+1} - \widetilde{w}_{a,b} \tag{4.23}$$

The convergence of the algorithm is evaluated by considering, at each iteration, the residual norm $\|r\| = \sqrt{\sum_{a=1}^{n_x-1}\sum_{b=1}^{n_y} r_{a,b}\, r^{cc}_{a,b}}$, where cc indicates the complex conjugate.

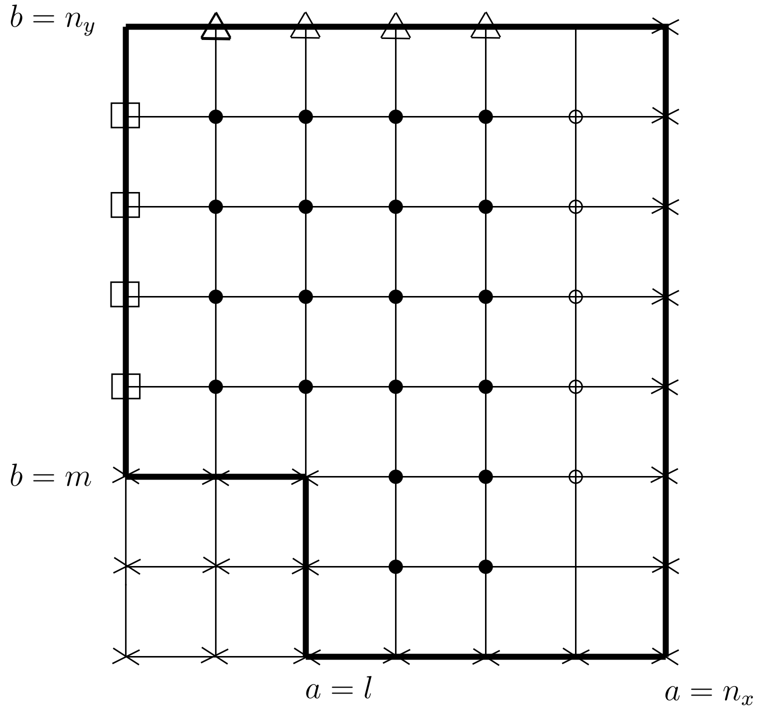

Figure 4.1: Sketch of the computation domain for the laminar equation. The indices l and m indicated the position of the bar on the x and y axis respectively.

4.3 Laminar power

The laminar power spent is defined as

$$\mathcal{P}_l = -\frac{1}{T}\int_0^T \Pi_z(\tau)\; W_{bl}(\tau)\; \mathrm{d}\tau, \tag{4.24}$$

where the laminar bulk velocity is $W_{bl} = 1/V_F \int_{V_F} w_l(x,y,\tau)\,\mathrm{d}V$. It can be simplified by using (4.10),

$$W_{bl} = \frac{1}{2V_F}\int_{V_F} \left(\widehat{w}_1\, e^{i\,\omega_T\,\tau} + \widehat{w}_1^{cc}\, e^{-i\,\omega_T\,\tau}\right)\,\mathrm{d}V = \frac{1}{2}\left(\widehat{w}_b e^{i\,\omega_T\,\tau} + \widehat{w}_b^{cc} e^{-i\,\omega_T\,\tau}\right), \tag{4.25}$$

where $\widehat{w}_b = 1/V_F \int_{V_F} \widehat{w}_1\,\mathrm{d}V$. Substituting the second of (4.6) and (4.25) into (4.24) leads to

$$\mathcal{P}_l = -\frac{A}{4}\left(\widehat{w}_b + \widehat{w}_b^{cc}\right) \tag{4.26}$$

By introducing $\widehat{w}_b = A\widehat{w}_{u,b}$, where $\widehat{w}_{u,b}$ is the value of $\widehat{w}_b$ obtained by using $A = 1$, (4.26) can be written in terms of $\widehat{w}_u$ as

$$\mathcal{P}_l = -\frac{A^2}{4}\left(\widehat{w}_{u,b} + \widehat{w}^{cc}_{u,b}\right) = A^2 P_{lu}, \tag{4.27}$$

where P_{lu} is the laminar power obtained for $A = 1$. The laminar power can also be expressed as the percentage of the power employed for driving the uncontrolled turbulent flow along x,

$$\mathcal{P}_l(\%) = -\frac{100\mathcal{P}_l}{\Pi_x U_b} = \frac{25A^2}{\Pi_x U_b}\left(\widehat{w}_{u,b} + \widehat{w}^{cc}_{u,b}\right). \tag{4.28}$$

4.4 Laminar results

We solve the complete equation (4.11) taking into account or neglecting the last term in parenthesis on the left hand side. We compare the solution in these two cases to quantify the effect of the advective terms on w_l, find the locations where they are important and determine whether they have an impact on the laminar power spent $\mathcal{P}_l$.

Figure 4.2 shows the absolute values of the difference of the real parts (top) and the difference of the imaginary parts (bottom) of the two solutions obtained including or not the advective terms respectively. The contours show that the difference of the solutions approaches a null value outside a boundary-layer surrounding the cavity and the bar. This shows that the effect of the advective terms is felt by the fluid only locally near the wall.

For a smooth channel, it is possible to find an analytical expression relating the power $\mathcal{P}_l$ to the forcing parameters A and T (Ricco and Quadrio, 2008). We herein use the analytical expression for $\mathcal{P}_l$ in the smooth channel case to obtain an empirical relationship linking the power $\mathcal{P}_l$ spent for oscillating the flow over the bars to the period of oscillation T. In the smooth channel case, the viscous term and the spatial advection terms are null. The viscous term is zero because of periodicity along x which makes the flow homogeneous in the streamwise direction. Therefore, the laminar flow satisfies

$$\begin{cases} \frac{\mathrm{d}^2\widetilde{w}}{\mathrm{d}y^2} - i\omega_T Re_p \widetilde{w} = 0, \\ \widetilde{w}(0) = \widetilde{w}(2) = -\frac{A}{\omega_T} i. \end{cases} \tag{4.29}$$

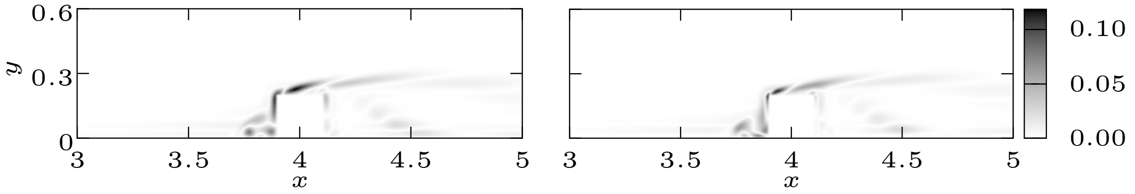

Figure 4.2: Absolute value of the difference between the solution $\widehat{w}_{\pm 1}$ of (4.8b) obtained with the advective terms and the one obtained without them for $A = 1$ and $T = 2.3$. The contour on the left is absolute value of the difference between the respective real parts while the last contour represents the absolute value of the difference of the imaginary parts.

By imposing the boundary conditions on the general solution $\widetilde{w} = C_1 e^{\xi y} + C_2 e^{-\xi y}$ and using $\widehat{w}_1 = \widetilde{w} + Ai/\omega_T$ we get

$$\widehat{w} = \frac{Ai}{\omega_T}\left[1 - \frac{e^{\xi(y-2)} + e^{-\xi y}}{1 + e^{-2\xi}}\right], \tag{4.30}$$

where $\xi = \sqrt{i\omega_T Re_p}$. The integrated velocity $\widehat{w}_b$ for the smooth channel is therefore

$$\widehat{w}_b = \frac{1}{2}\int_0^2 \widehat{w}\mathrm{d}y = \int_0^1 \widehat{w}\mathrm{d}y = \frac{A}{\omega_T} i\left[1 - \frac{1 - e^{-2\xi}}{\xi(1 + e^{-2\xi})}\right]. \tag{4.31}$$

By noting that $\widehat{w}_b + \widehat{w}_b^{cc}$ is twice the real part of $\widehat{w}_b$ we obtain

$$\widehat{w}_b + \widehat{w}_b^{cc} = 2\mathfrak{Re}(\widehat{w}_b) = -\frac{2A}{\omega_T}\mathfrak{Re}\left(\frac{i}{\xi}\frac{1 - e^{-2\xi}}{1 + e^{-2\xi}}\right) = -\frac{\sqrt{2}A}{\omega_T^{3/2}\sqrt{Re_p}}\mathfrak{Re}\left[(i+1)\frac{1 - e^{-2\xi}}{1 + e^{-2\xi}}\right], \tag{4.32}$$

where $\mathfrak{Re}$ indicates the real part. When $2\sqrt{\omega_T Re_p} \gg 1$ equation (4.32) can be approximated by

$$\widehat{w}_b + \widehat{w}_b^{cc} \approx -\frac{\sqrt{2}A}{\omega_T^{3/2}\sqrt{Re_p}}\mathfrak{Re}\,(i+1) = -\frac{\sqrt{2}A}{\omega_T^{3/2}\sqrt{Re_p}}. \tag{4.33}$$

The laminar power spent for a smooth channel can be obtained by substituting (4.33) into (4.26),

$$\mathcal{P}_{chan} = \frac{\sqrt{2}A^2}{4\sqrt{Re_p}}\omega_T^{-3/2} = \frac{A^2}{8\pi^{3/2}\sqrt{Re_p}}T^{3/2}. \tag{4.34}$$

Equation (4.34) suggests that expression FA^2T^γ could be an approximation to $\mathcal{P}_l$. Fitting FA^2T^γ with the laminar data points gives

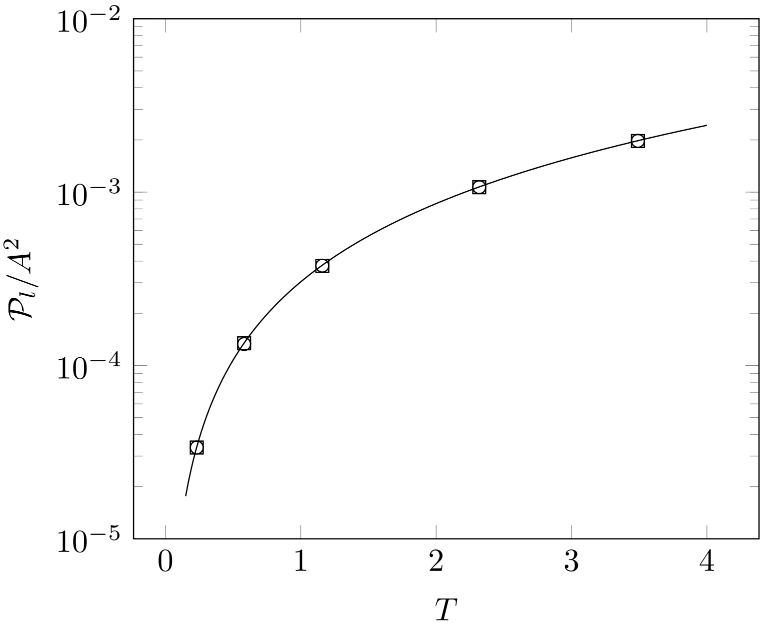

Figure 4.3: $\mathcal{P}_l/A^2$ as a function of T for (4.11) without (circles) and with (squares) the mean advective terms. The solid line represents the function $\mathcal{P}_l/A^2 = 3.03 \times 10^{-4} T^{1.5}$. The ordinate axis is in logarithmic scale.

$$\mathcal{P}_l(\%) \approx 100\,\frac{3.03 \times 10^{-4} A^2 T^{3/2}}{-\Pi_x U_b} = -\frac{3.03 \times 10^{-2} A^2 T^{3/2}}{\Pi_x U_b}. \tag{4.35}$$

Expression (4.35) is plotted in figure 4.3 together with the values obtained via the laminar simulations. Figure 4.3 shows that the mean advective terms and the viscous diffusion along x have a small impact on $\mathcal{P}_l$.

Chapter 5

Controlled channel with bars

In this chapter, the flow introduced in section 3.3 of chapter 3 is controlled via a spanwise oscillating pressure gradient $\Pi_z^* = A^* \cos(2\pi t^*/T^*)$, where A^* and T^* are the amplitude and the period scaled as $A = A^* \, \delta^* / \left(\rho^* U_p^{*2}\right)$ and $T = T^* U_p^* / \delta^*$ respectively. We introduce the parameters necessary to evaluate the performance of the control in terms of drag reductions percentages and net power saved. Then, we briefly present results on the canonical flow without control and in the following sections the effects of the oscillating pressure gradients are discussed.

5.1 Parameters defining the actuation performance

We define a percentage reduction for each drag coefficient. For instance, the percentage reduction of $C_{f,ca}$ is defined

$$\mathcal{R}_{ca}(\%) = 100 \left(1 - \frac{C_{f,ca_o}}{C_{f,ca}}\right), \tag{5.1}$$

where $C_{f,ca}$ and C_{f,ca_o} are the uncontrolled and controlled values, respectively. The total drag reduction $\mathcal{R}(\%)$ is defined as

$$\mathcal{R}(\%) = 100 \left(1 - \frac{C_{f_o} + C_{p_o}}{C_f + C_p}\right). \tag{5.2}$$

As we study an active technique, the power $\mathcal{P}(\%)$ supplied to the fluid is

$$\mathcal{P}(\%) = \frac{100}{\Pi_x U_b (t_f - t_i)} \int_{t_i}^{t_f} \Pi_z(t) \, W_b(t) \, \mathrm{d}t, \tag{5.3}$$

expressed as percentage of the power used to drive the fluid along the streamwise direction. In (5.3) Π_x is the mean pressure gradient driving the flow along x in the uncontrolled case, U_b is the constant streamwise bulk velocity $U_b = 1/V_F \int_{V_F} u(x,y,z,t)\,\mathrm{d}V$, $W_b(t)$ is the spanwise bulk velocity due to the control, $W_b = 1/V_F \int_{V_F} w(x,y,z,t)\,\mathrm{d}V$, and V_F is the fluid volume. Appendix E presents the derivation for the power used to drive fluid along x.

The percentage of power saved is defined as

$$\mathcal{P}_{sav}(\%) = 100\left(1 - \frac{-\Pi_{xo}U_b}{-\Pi_x U_b}\right), \tag{5.4}$$

where $-\Pi_{xo}U_b$ and $-\Pi_x U_b$ are the powers for driving the flow along x with and without control, respectively. As $-\Pi_x L_y = C_f + C_p$ and $-\Pi_{xo} L_y = C_{f_o} + C_{p_o}$ (refer to appendix B), it follows that

$$\mathcal{P}_{sav}(\%) = 100\left(1 - \frac{\Pi_{xo}}{\Pi_x}\right) = 100\left(1 - \frac{C_{f_o} + C_{p_o}}{C_f + C_p}\right) = \mathcal{R}(\%). \tag{5.5}$$

The balance between the control power supplied to the system and the power saved $\mathcal{P}_{sav}(\%)$ reads:

$$\mathcal{P}_{net}(\%) = \mathcal{R}(\%) - \mathcal{P}(\%). \tag{5.6}$$

5.2 Uncontrolled flow

The mean-flow streamlines in the region surrounding the bar in the uncontrolled flow case are depicted in figure 5.1. The separation zone is occupied by three recirculating areas: A and B areas are adjacent to the vertical edges of the bar and have size comparable with the bar height. Area C extends for about a length of five bar heights along the streamwise direction and also covers the crest where a mild separation occurs. Vortices A and C rotate clockwise, while vortex B rotates anticlockwise. Sufficiently far from the bar ($x < 3$ and $x > 6$) the flow is not influenced by the obstacle and the lines become straight and aligned to the streamwise direction.

Figure 5.2 shows the spanwise and time averaged pressure for the uncontrolled flow. The pressure reaches its maximum along the left edge of the bar where the vortex A occurs, and high values of pressure are also obtained for $x < 3.9$, where the flow is

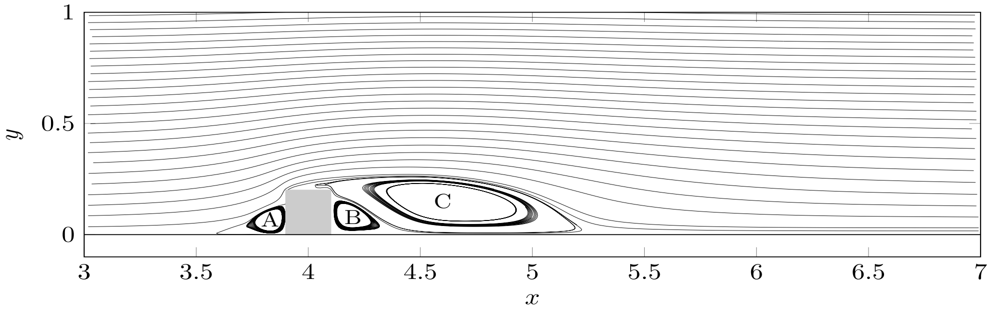

Figure 5.1: Time and z averaged streamlines for the flow without control. The bar is indicated by the grey square. Only the area which extends from $x = 3$ and $x = 7$ and from $y = 0$ and $y = L_y/2 = 1.2$ is represented. Vortices are indicated by letters A, B and C.

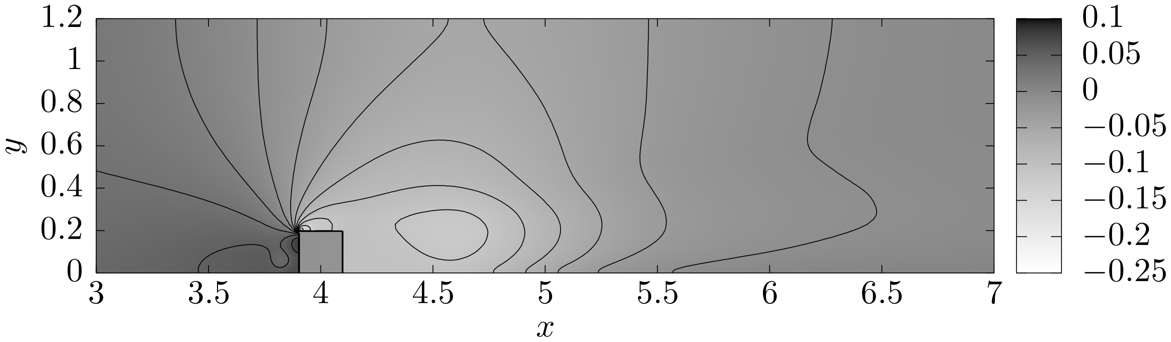

Figure 5.2: Color map and contours of the mean pressure without control. The bar is indicated by a grey square centered at $x = 4.0$. Only the area which extends from $x = 3$ and $x = 7$ and from $y = 0$ and $y = L_y/2 = 1.2$ is represented. The isolines values are spaced at intervals of 0.02 in the range $[-0.25, 0.1]$.

attached. The center of area C, located approximately at $x = 4.6$, is characterized by a low level of pressure.

5.3 Drag and flux coefficients

The effect of the control on the drag coefficients for the case with maximum drag reduction is presented in figure 5.3 where the control is activated at $t = 150$. The control with $T = 2.3$ guarantees a substantial reduction of total drag $C_p + C_f$ thanks to the reduction of of both C_p and C_f. The coefficient of flux of $p\,\mathbf{i}$ (refer to section 3.3.2) C_{pr} decreases more than C_{pl} because of the action of the control. The skin-friction reduction is mostly due to the decrease of the cavity contribution as $C_{f,cr}$ experiences a small variation. This is in contrary to most of traditional separation control methods (vortex generators, jets) which introduce a viscous drag penalty due

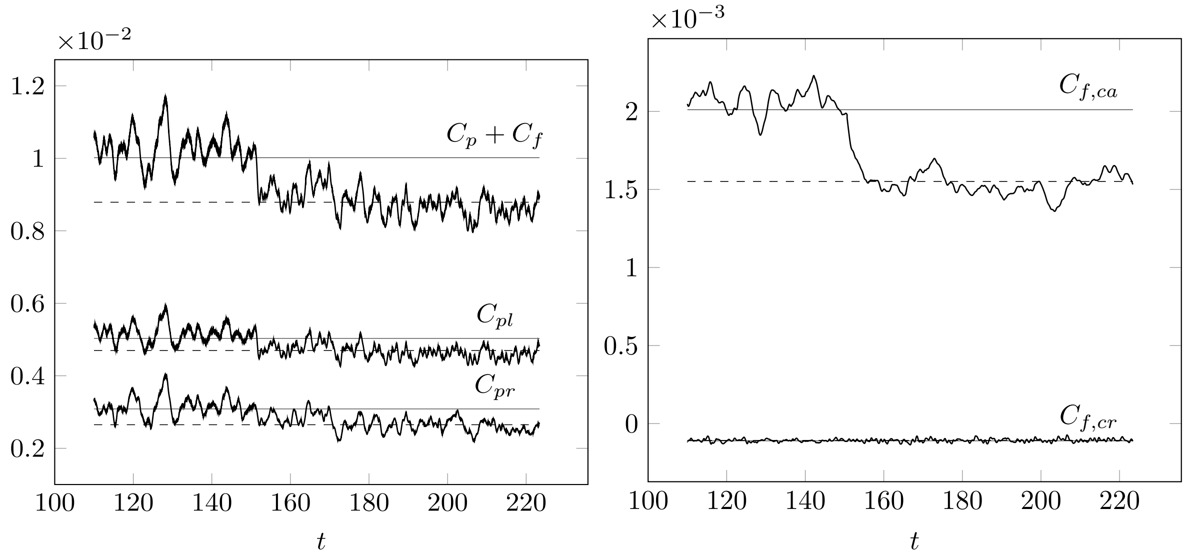

Figure 5.3: Left: Time evolution of the mean drag coefficient $C_p + C_f$ and the pressure flux coefficients C_{pl} and C_{pr}. Right: Time evolution of $C_{f,cr}$ and $C_{f,ca}$. The control is activated at $t = 150$ (denoted by black circle) with $A = 3$ and $T = 2.3$. The horizontal solid and dashed lines indicate the mean value of each coefficient without and with control respectively.

to the enhanced flow mixing. The time averaged coefficients are computed after the end of the transient phase estimated at $t = 170$, when the coefficients reach a new statistical steady state. C_{pl}, C_{pr} and $C_{f,ca}$ decrease below the the uncontrolled values during actuation, while $C_{f,cr}$ remains almost unaffected.

Table 5.1 shows the values of the coefficients as a function of T and A for the analyzed cases and table 5.2 presents the computed percentage variations of the drag and flux coefficients. We note that the computed reductions are affected by errors due to the finite time-averaging and the grid resolution. In appendix D a conservative estimation of the uncertainty only for the best controlled case ($A = 3.0$, $T = 2.3$) is performed as the main results are related to this case. This analysis shows that $\mathcal{R}(\%)$ can be determined within an error of order ±1% therefore $\mathcal{R}(\%)$ with small T cannot be estimated reliably but are presented for completeness. Drag reductions occur at large periods ($T = 1.1, 2.3$) where all the coefficients decrease below their uncontrolled values. The maximum reductions are obtained for $T = 2.3$ and tripling the amplitude raises $\mathcal{R}(\%)$, $\mathcal{R}_p(\%)$, $\mathcal{R}_f(\%)$ by a factor of three.

T	A	$C_{f,cr_o}(10^{-4})$	$C_{f,ca_o}(10^{-3})$	$C_{pl_o}(10^{-3})$	$C_{pr_o}(10^{-3})$	$-\Pi_{xo}L_y(10^{-3})$
0.2	0.1	-1.08	2.04	5.02	3.04	9.99
0.2	0.5	-1.08	1.94	4.98	3.08	9.90
0.2	1.0	-1.09	2.02	5.00	3.06	9.96
0.2	2.2	-1.08	2.03	5.09	3.14	10.1
0.2	10.0	-1.09	2.04	4.98	3.03	9.94
0.5	1.0	-1.10	2.03	5.04	3.11	10.1
1.1	0.5	-1.08	1.95	4.90	2.99	9.74
1.1	1.0	-1.09	1.91	4.95	3.06	9.81
2.3	1.0	-1.10	1.84	4.87	2.95	9.56
2.3	3.0	-1.08	1.55	4.70	2.65	8.79

Table 5.1: Mean drag and flux coefficients after the control is turned on. The order of magnitude of the coefficients in terms of power of ten is indicated in round brackets.

T	A	$\mathcal{R}_{cr}(\%)$	$\mathcal{R}_{ca}(\%)$	$\mathcal{R}_{f}(\%)$	$\mathcal{R}_{pl}(\%)$	$\mathcal{R}_{pr}(\%)$	$\mathcal{R}_{p}(\%)$	$\mathcal{R}(\%)$
0.2	0.1	2.4	-1.3	-1.6	0.2	1.5	0.7	0.2
0.2	0.5	2.6	3.2	3.3	0.9	0.1	0.6	1.1
0.2	1.0	1.5	-0.3	-0.4	0.7	0.8	0.7	0.5
0.2	2.2	2.2	-0.8	-1.0	-1.1	-1.7	-1.3	-1.2
0.2	10.0	1.8	-1.3	-1.5	0.9	1.8	1.2	0.7
0.5	1.0	0.4	-0.7	-0.8	-0.2	-0.7	-0.4	-0.4
1.1	0.5	2.2	3.1	3.2	2.5	3.0	2.7	2.7
1.1	1.0	1.2	4.8	5.0	1.6	0.9	1.3	2.0
2.3	1.0	0.4	8.3	8.8	3.1	4.2	3.5	4.5
2.3	3.0	2.6	22.8	24.0	6.6	14.1	9.4	12.2

Table 5.2: Percentage variations of drag and pressure flux coefficients after the control is activated. Positive values indicate reductions, negative stem for increases. The values are obtained by $\mathcal{R}(\%) = 100\,(1 - C_o/C)$. Where C is any of the drag coefficients and C_o the value after the control is turned on. None of the percentage variations may be obtained as the sum of other two.

5.4 Mean flow

Figure 5.4 compares the mean streamlines of the uncontrolled flow with the controlled streamlines. Although the forcing slightly reduces the size of recirculation areas B and C this effect is too small to be considered significant from a drag reduction point of view. Interestingly, a displacement of the separation point upstream of the area A occurs and a tiny vortex lying on the cavity with core at $x \approx 3.72$ is created. It is interesting to note that if the flow was steady the Batchelor model characterized by a closed recirculation area behind the bars would apply. This model predicts a null drag (d'Alembert paradox) as $Re \rightarrow +\infty$ because the flow would be solenoidal and inviscid outside the area composed of the recirculation area and the body (Batchelor, 1956).

The spanwise and time averaged pressure after the activation of the control is shown in the contour plot of figure 5.5. The structure of p_m is similar to the one of the uncontrolled pressure with the high and low pressures regions near the left and right vertical edges of the bar and the minimum absolute located at the left top corner on the crest. The control decreases the pressure in the region of $x < 3.9$, while moving the isoline of maximum pressure toward the cavity. The pressure increases in the region of $x > 4.1$ lifting the low pressure contours that connect the left top corner of the bar and the right side of the cavity.

Figure 5.6 depicts the mean pressure and shear stress at wall with and without control to elucidate the origin of the pressure and skin-friction drag reduction. The spanwise oscillating forcing reduces the pressure on the left edge and increases it on the right side. As $P_d^* = \int_{S_l^*} \overline{p^*} \, \mathrm{d}S - \int_{S_r^*} \overline{p^*} \, \mathrm{d}S$ (refer to section 5.1) it follows that the first integral decreases and the latter increases reducing the pressure drag. We also note the negative pressure peak at $s = 1.1$ indicating the singularity at the left top corner of the bar. The two profiles tend to overlap for $x > 3.5$ showing a small effect of the control on the pressure in this region. The wall-shear stress decreases along the major part of the cavity area where the flow is attached ($s < 0.5$ and $s > 2.7$) and increases near the left edge of the bar ($0.45 < s < 0.9$) as shown in figure where the negative skin-friction peak at $s \approx 0.9$ is moved upward. Both $C_{f,cr}$ and C_{ca} decrease giving a reduction on the skin-friction coefficient C_f.

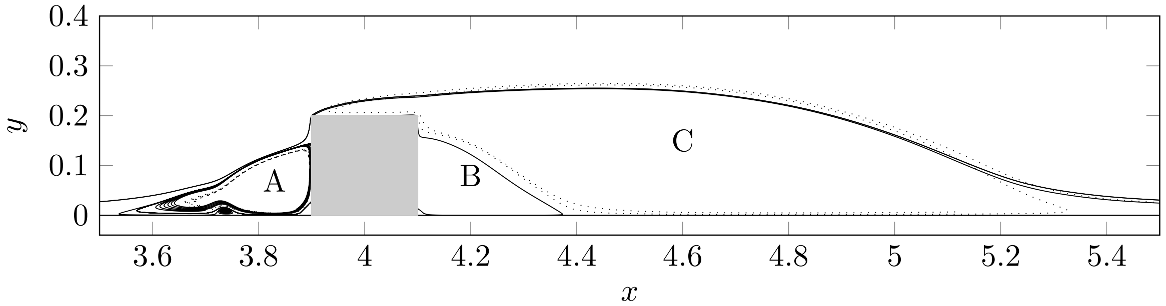

Figure 5.4: Effect of the control on the separation area. Dotted and solid lines indicate the z and time averaged streamlines for the uncontrolled and controlled flow respectively.

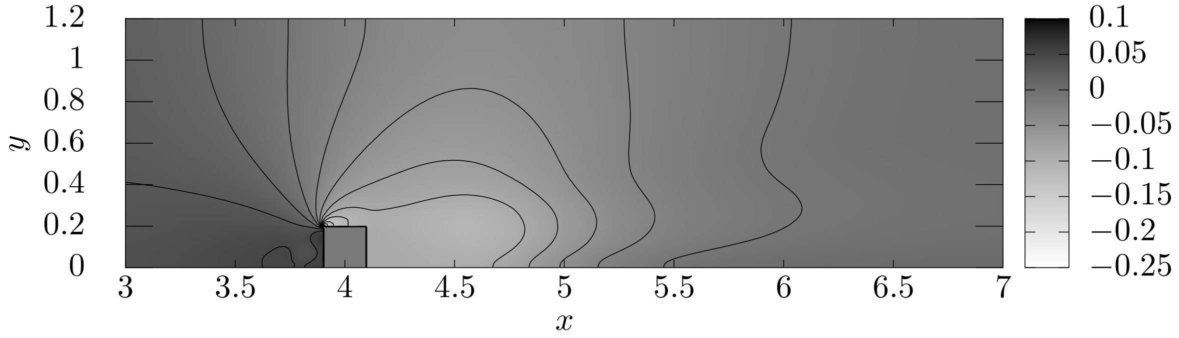

Figure 5.5: Color map and contours of the mean pressure with control. The bar is indicated by a grey square centered at $x = 4.0$. Only the area which extends from $x = 3.0$ and $x = 7.0$ and from $y = 0.0$ and $y = L_y/2 = 1.2$ is represented. The isolines values are spaced at intervals of 0.02 in the range $[-0.25, 0.1]$.

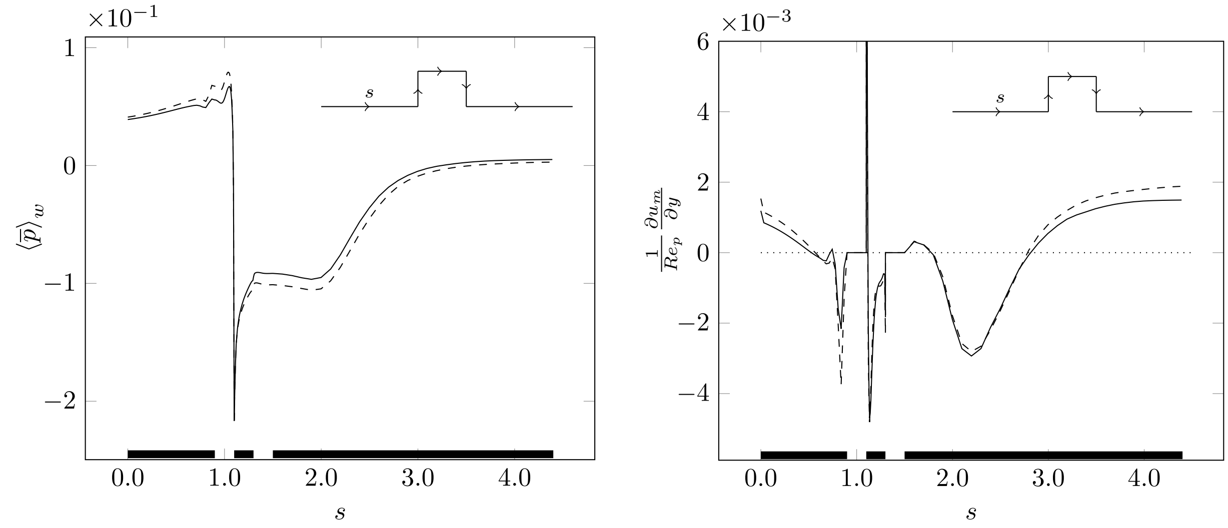

Figure 5.6: Left: spanwise and time averaged pressure at the wall. Right: shear stress at wall. Solid and dashed lines represent the profile with and without control, respectively. Control parameters are $T = 2.3$ and $A = 3$. s is the arc length running on the wall surface as depicted at the top of each figure. Note that the origin of s is placed at point $(3, 0)$. The ticker black lines at the bottom of the figures indicates the range of s where the wall surface is horizontal.

5.5 Turbulent and laminar spanwise velocity

Figure 5.7 depicts the comparisons between $\langle \widehat{w} \rangle$ and w_l for $\tau = 0, T/4, T/2, 3/4T$ at different x stations. The laminar solution w_l matches perfectly $\langle \widehat{w} \rangle$ outside the separation area ($x = 3$ and $x = 7$) for $\tau = T/4, \tau = 3/4T$. When $\tau = 0, T/2$ a good agreement far from the bar and near the cavity ($x = 3, 7$, $y < 0.05$) is obtained, but w_l tends to be null for $y > 0.05$ contrarily to $\langle \widehat{w} \rangle$. The profiles at the vertical edges of the bar ($x = 3.9, 4.1$) indicate that the laminar simulation is able to recover the value of $\langle \widehat{w} \rangle$ far from the cavity ($y > 0.3$) and only for $\tau = T/4$ and $\tau = 3/4T$. A partial agreement between the phase and spanwise averaged velocity $\langle \widehat{w} \rangle$ and w_l is observed here. The differences between the laminar and turbulent flows are due to the transverse Reynolds stresses $-\partial \langle \widehat{u_t w_t} \rangle / \partial x$ and $-\partial \langle \widehat{v_t w_t} \rangle / \partial y$ in eq. (4.4) and to the differences between $\langle \widehat{u} \rangle$ and $\langle \widehat{v} \rangle$ and the uncontrolled velocities as stated in chapter 4. Overall, the turbulent velocity $\langle \widehat{w} \rangle$ shows an acceptable agreement with w_l, proving that the analysis of chapter 4 gives a relevant physical model of the transverse oscillating mean flow obtained from DNS.

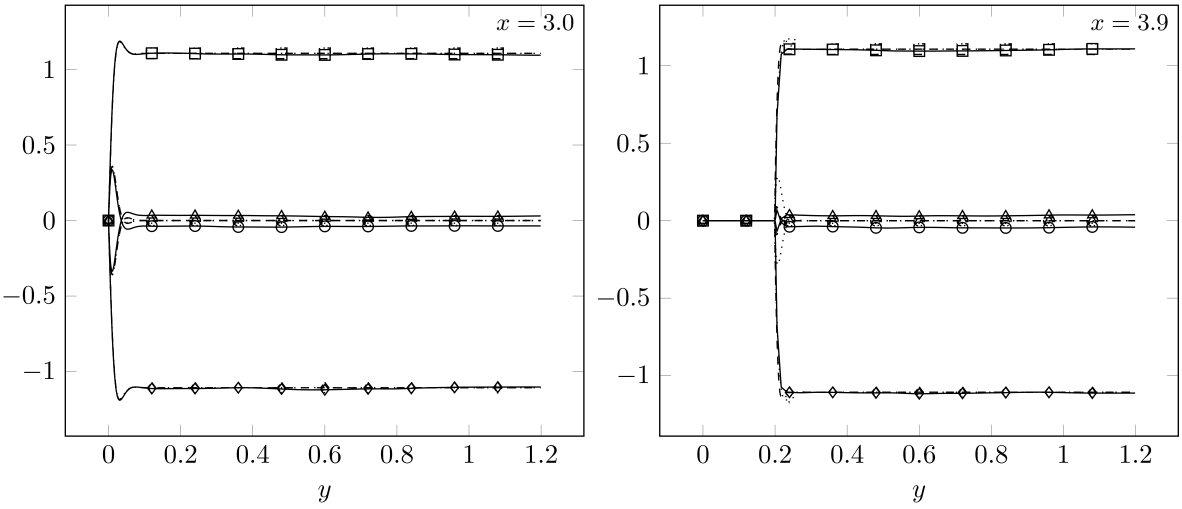

Figure 5.7: Continue in the next page

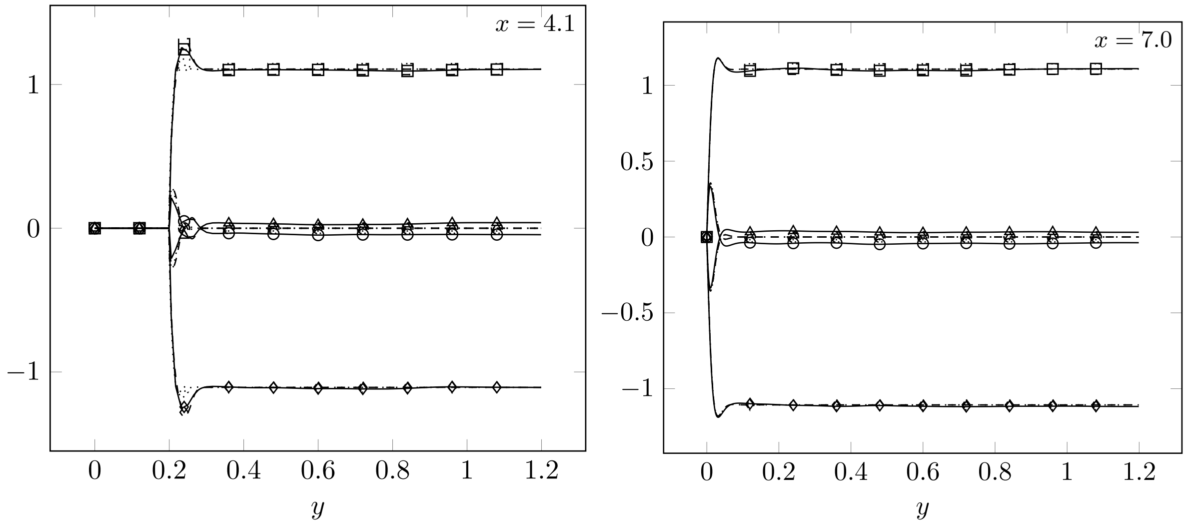

Figure 5.7: Comparison between $\langle \widehat{w} \rangle$ (solid) and w_l obtained via eq. 4.5 with (dashed) and without (dotted) the last term on the right hand side. Profiles are taken at $\tau = 0$ (circle), $T/4$ (square), $T/2$ (triangle), $3/4T$ (diamond). The x location where the curves are depicted is indicated on the top right corner of each figure.

T	A	$\mathcal{R}(\%)$	$\mathcal{P}(\%)$	$\mathcal{P}_l(\%)$	$\mathcal{P}_{net}(\%)$
0.2	0.1	0.2	0.0	0.0	0.2
0.2	0.5	1.1	0.3	0.3	0.7
0.2	1.0	0.5	1.4	1.4	-0.9
0.2	2.2	-1.2	7.3	7.3	-8.6
0.2	10.0	0.7	145.2	145.5	-144.5
0.5	1.0	-0.4	5.7	5.7	-6.2
1.1	0.5	2.7	4.1	4.0	-1.3
1.1	1.0	2.0	16.2	16.2	-14.2
2.3	1.0	4.5	46.4	46.0	-41.9
2.3	3.0	12.2	418.0	414.1	-405.7

Table 5.3: Turbulent power $\mathcal{P}(\%)$, net turbulent power $\mathcal{P}_{net}(\%)$ and laminar power $\mathcal{P}_l(\%)$ as a function of the control parameters A and T.

5.6 Power spent and net power saved

Tab. 5.3 illustrates the balance between the energy saved ($\mathcal{R}(\%)$) and the energy spent to activate the control ($\mathcal{P}(\%)$), and the laminar power for any couple of parameters (T, A). Appreciable drag reductions occur at the expense of an high consumption of energy giving no savings in terms of $\mathcal{P}_{net}(\%)$. Figure 5.8 shows the values of $\mathcal{P}(\%)$ obtained via DNS against their laminar P_l. The laminar power $P_l(\%)$ gives an excellent approximation of $\mathcal{P}(\%)$ for all the A and T considered except for $(T, A) = (0.2, 0.1)$ where $P_l(\%)$ is lower than its turbulent value. The laminar solution found in section 4.4 is therefore able to predict the turbulent power spent very well.

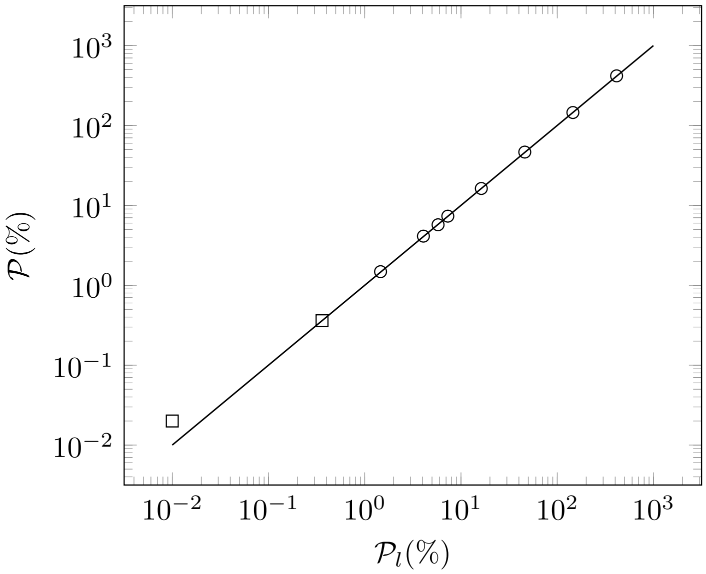

Figure 5.8: Turbulent power spent $\mathcal{P}(\%)$ vs its laminar $\mathcal{P}_l(\%)$. The solid line indicates the function $\mathcal{P}(\%) = \mathcal{P}_l(\%)$. Squares and circles represent the points with positive and negative $\mathcal{P}_{net}(\%)$ respectively.

5.7 Statistics

Figure 5.9 depicts the spanwise and phase averaged velocity components at different streamwise locations and phase of oscillation. The velocities $\langle\widehat{u}\rangle$ and $\langle\widehat{v}\rangle$ do not depend on τ and overlap with their time averaged velocities u_m and v_m showing a similar behavior to the channel with an oscillating wall (Jung et al., 1992). The velocity $\langle\widehat{v}\rangle$ is smaller than $\langle\widehat{u}\rangle$ for every x and τ and negligible outside recirculation areas ($x = 7$). In general, $\langle\widehat{v}\rangle$ increases until an absolute maximum is obtained then the curves tend monotonically to zero at $y = 1.2$. Both $\langle\widehat{u}\rangle$ and $\langle\widehat{v}\rangle$ increase steeply from zero to a maximum at the left edge of the bar ($x = 3.9$) due to intense gradients and the singularity at the left top corner of the bar. The spanwise components $\langle\widehat{w}\rangle$ at $\tau = 0$ and $\tau = T/4$ are 90 degrees out of phase with the curves at $\tau = T/2$ and $\tau = 3/4T$. This results in $\langle\overline{w}\rangle$ profiles much smaller than their phase averaged values. Near the cavity and for all phases, the velocity $\langle\widehat{w}\rangle$ shows an overshoot before reaching its value at the channel midline ($y = 1.2$).

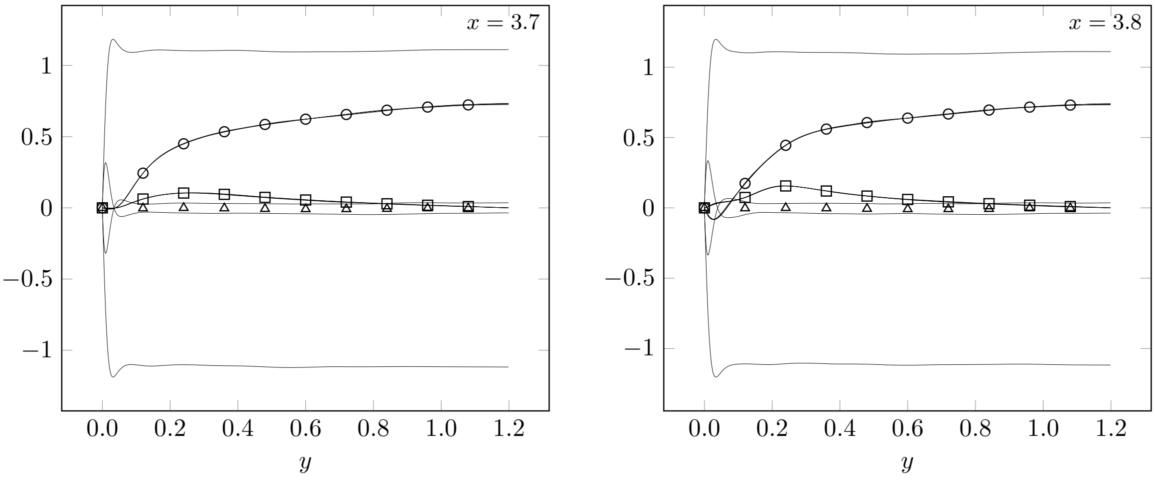

Figure 5.9: Continue in the next page

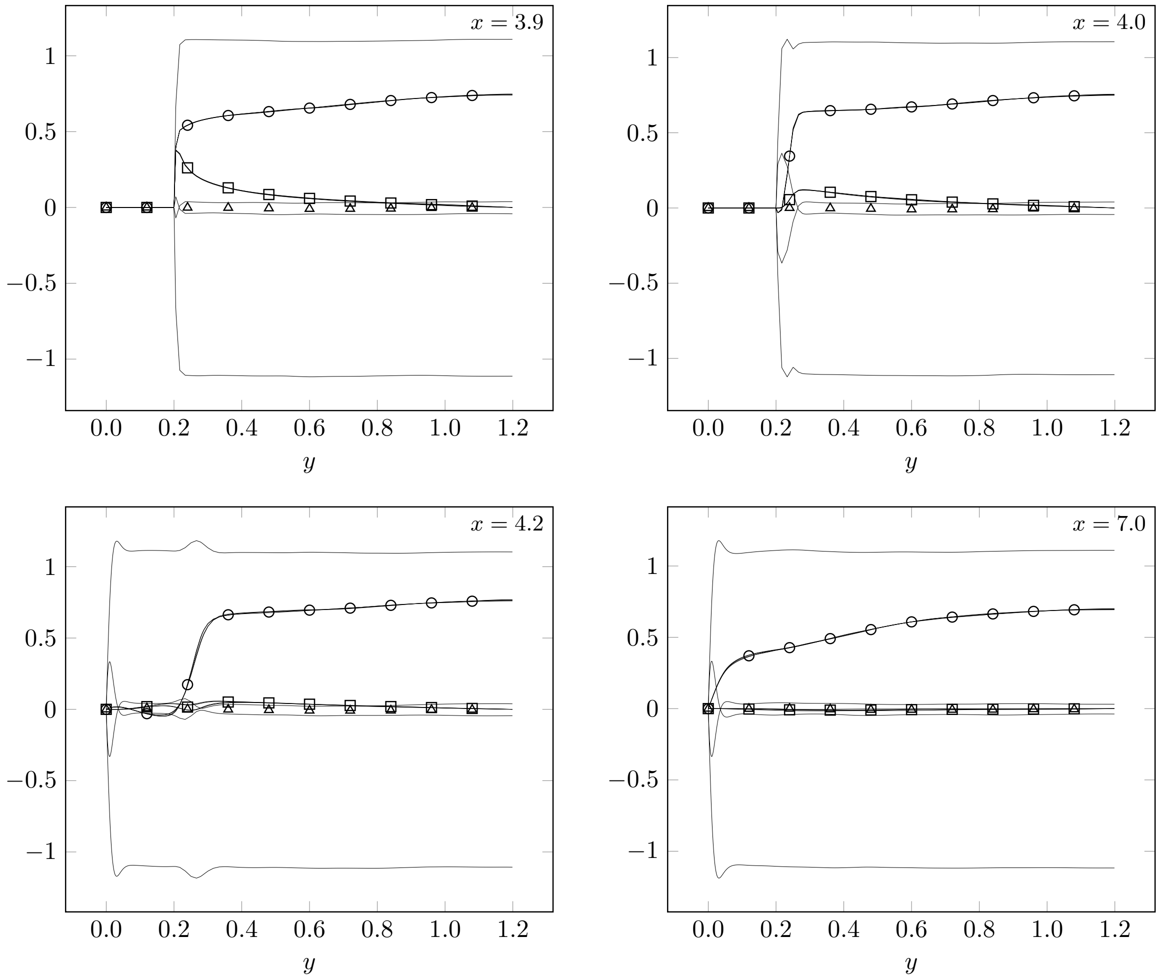

Figure 5.9: Phase and z averaged velocities $\langle\widehat{u}\rangle$, $\langle\widehat{v}\rangle$ and $\langle\widehat{w}\rangle$ against y at different x locations and oscillations phases (solid lines). Circles, squares and triangles indicate the spanwise and time averaged velocities $\langle\overline{u}\rangle$, $\langle\overline{v}\rangle$ and $\langle\overline{w}\rangle$ for the controlled flow.

The turbulence intensities $\langle\widehat{u_t u_t}\rangle$, $\langle\widehat{v_t v_t}\rangle$ and $\langle\widehat{w_t w_t}\rangle$ are shown with $\langle\overline{u_t u_t}\rangle$, $\langle\overline{v_t v_t}\rangle$ and $\langle\overline{w_t w_t}\rangle$ in figure 5.10. The turbulent intensities are higher at the edges of the bar where peaks of $\langle\widehat{u_t u_t}\rangle$ and $\langle\overline{u_t u_t}\rangle$ represent values two and four times higher than the values far from separation ($x = 3, 7$). The profiles of $\langle\widehat{u_t u_t}\rangle$ and $\langle\overline{u_t u_t}\rangle$ show two local maximum far from the bar with the global maximum occurring at $y = 0.1$ for $x = 3$ and $y = 0.5$ for $x = 7$. The streamwise turbulence intensity (circle) is dominant for both flows except for $x = 3.9$ where both $\langle\widehat{w_t w_t}\rangle$ and $\langle\overline{w_t w_t}\rangle$ show a peak around $y \approx 0.2$ for every τ. All turbulent intensities are reduced for any τ and x because of the control.

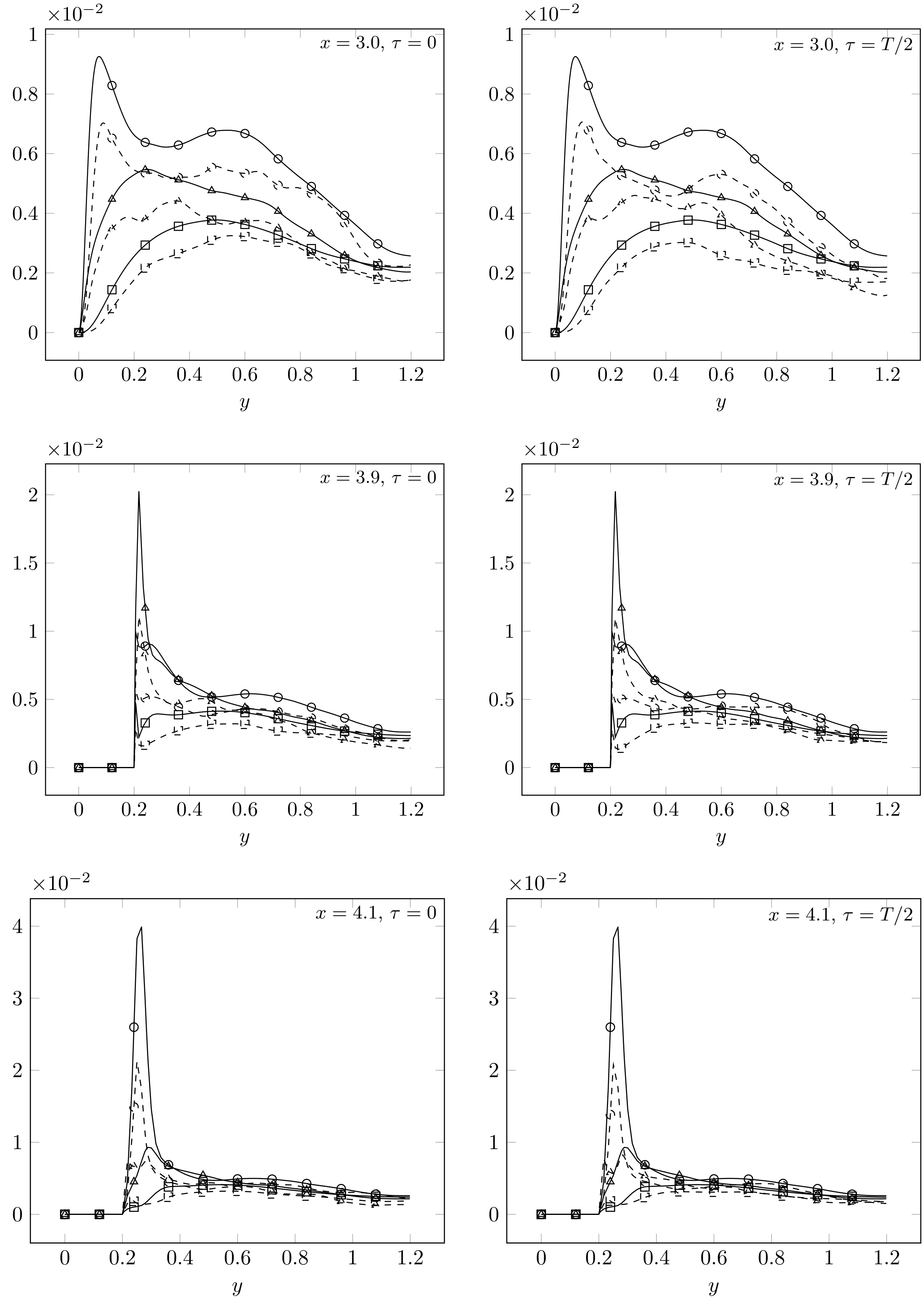

Figure 5.10: Refer to next page for caption.

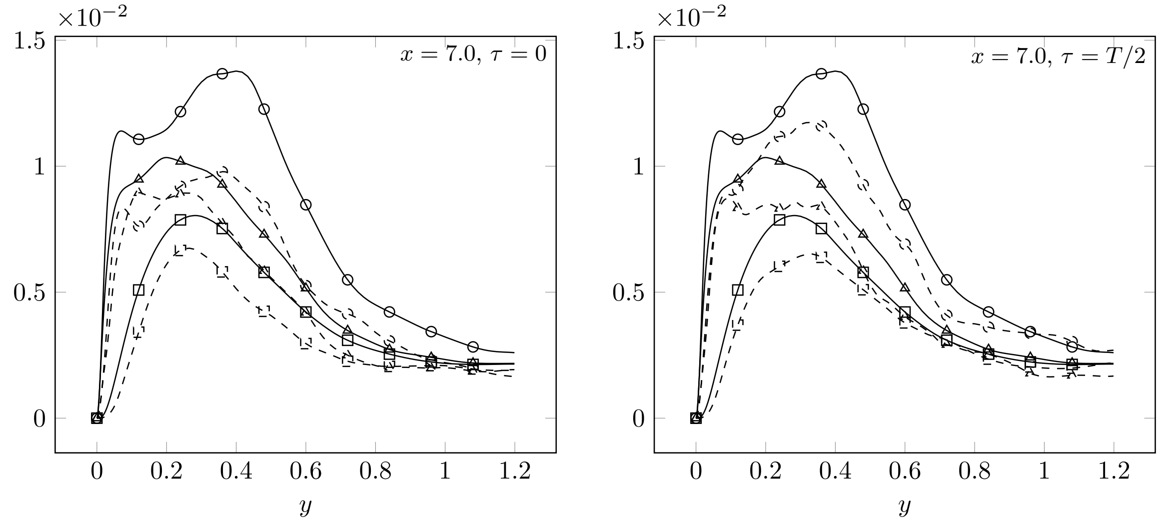

Figure 5.10: $\langle \widehat{u_t u_t} \rangle$ (circle), $\langle \widehat{v_t v_t} \rangle$ (square), $\langle \widehat{w_t w_t} \rangle$ (triangle) at different x stations and τ (dashed lines) and the uncontrolled flow statistics $\langle \overline{u_t u_t} \rangle$ (circle), $\langle \overline{v_t v_t} \rangle$ (square), $\langle \overline{w_t w_t} \rangle$ (triangle) at the same x (solid).

Figure 5.11 compares the opposite of the Reynolds stresses of the uncontrolled flow with those with actuation. The Reynolds stress $|\,\langle \widehat{u_t v_t} \rangle\,|$ is dominant over the other two and decreases under the level of $|\,\langle \overline{u_t v_t} \rangle\,|$ for almost every y at any x and τ similarly to Jung et al. (1992), but the opposite behavior happens for $|\,\langle \overline{u_t w_t} \rangle\,|$ and $|\,\langle \overline{v_t w_t} \rangle\,|$.

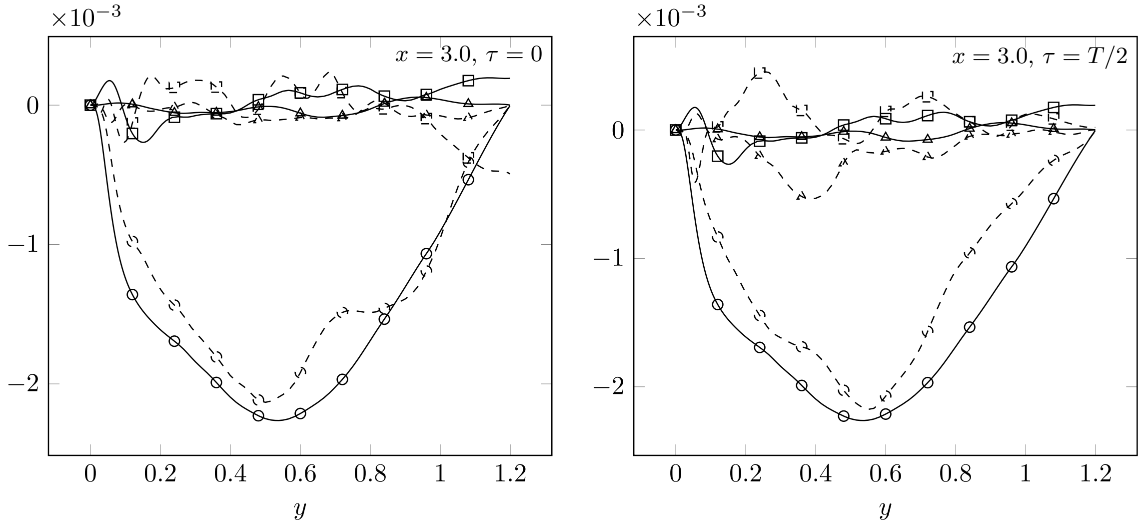

Figure 5.11: Continue in the next page.

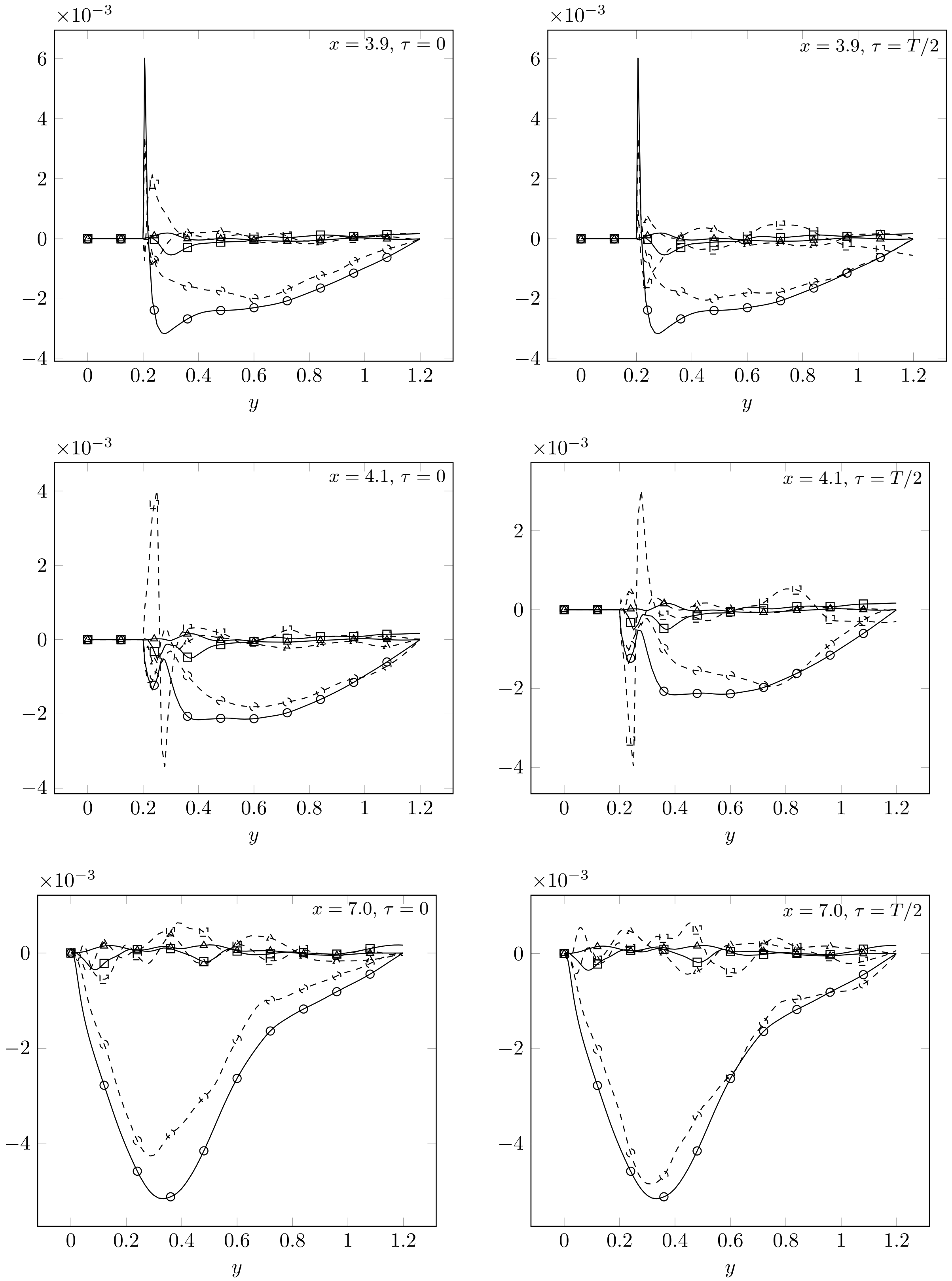

Figure 5.11: $\langle\widehat{u_t v_t}\rangle$ (circle), $\langle\widehat{u_t w_t}\rangle$ (square), $\langle\widehat{v_t w_t}\rangle$ (triangle) at different x stations and τ (dashed lines) and the uncontrolled flow statistics $\langle\overline{u_t v_t}\rangle$ (circle), $\langle\overline{u_t w_t}\rangle$ (square), $\langle\overline{v_t w_t}\rangle$ (triangle) at the same x (solid). The values of x and τ are indicated at the right top corner of each figure.

5.8 Drag reduction mechanism

5.8.1 Pressure drag reduction

The momentum balance for the separation area delimited by the dividing streamlines gives (refer to appendix F.1)

$$\begin{aligned}\widehat{C}_p =& \frac{2}{L_x}\int_{l_s}\frac{1}{|\widehat{\mathbf{U}}|}\left(\langle\widehat{v}\rangle\langle\widehat{u_t u_t}\rangle - \langle\widehat{u}\rangle\langle\widehat{u_t v_t}\rangle\right)\mathrm{d}l + \frac{2}{L_x}\int_{l_s}\frac{\langle\widehat{p}\rangle\langle\widehat{v}\rangle}{|\widehat{\mathbf{U}}|}\mathrm{d}l \\ &+ \frac{2}{L_x Re_p}\int_{l_s}\frac{\partial|\widehat{\mathbf{U}}|}{\partial y}\mathrm{d}l - \frac{2}{L_x Re_p}\left(\int_{x_s}^{x_a}\frac{\partial\langle\widehat{u}\rangle}{\partial y}\Big|_0\mathrm{d}x + \int_{x_b}^{x_r}\frac{\partial\langle\widehat{u}\rangle}{\partial y}\Big|_0\mathrm{d}x\right).\end{aligned} \tag{5.7}$$

Equation (5.7) shows that the pressure drag is related to the Reynolds stress $\left(\langle\widehat{v}\rangle\langle\widehat{u_t u_t}\rangle - \langle\widehat{u}\rangle\langle\widehat{u_t v_t}\rangle\right)/|\widehat{\mathbf{U}}|$, $\langle\widehat{p}\rangle\langle\widehat{v}\rangle/|\widehat{\mathbf{U}}|$, the gradient of the velocity magnitude $\partial|\widehat{\mathbf{U}}|/\partial y$ at the dividing streamline and the shear stress at the cavity wall $1/Re_p\partial\langle\widehat{u}\rangle/\partial y|_0$. The comparison of (5.7) with its uncontrolled version (obtained by substituting the phase average with the time average) gives some insight into the pressure drag reduction.

Figure 5.12 depicts the terms of (5.7) at different phases τ and their uncontrolled values. The pressure drag is mainly due to the sum of the Reynolds stress term $\frac{2}{L_x}\int_{l_s}\frac{1}{|\widehat{\mathbf{U}}|}\left(\langle\widehat{v}\rangle\langle\widehat{u_t u_t}\rangle - \langle\widehat{u}\rangle\langle\widehat{u_t v_t}\rangle\right)\mathrm{d}l$ and the pressure term $\frac{2}{L_x}\int_{l_s}\frac{\langle\widehat{p}\rangle\langle\widehat{v}\rangle}{|\widehat{\mathbf{U}}|}\mathrm{d}l$ while the last two terms due to viscous effects are smaller.

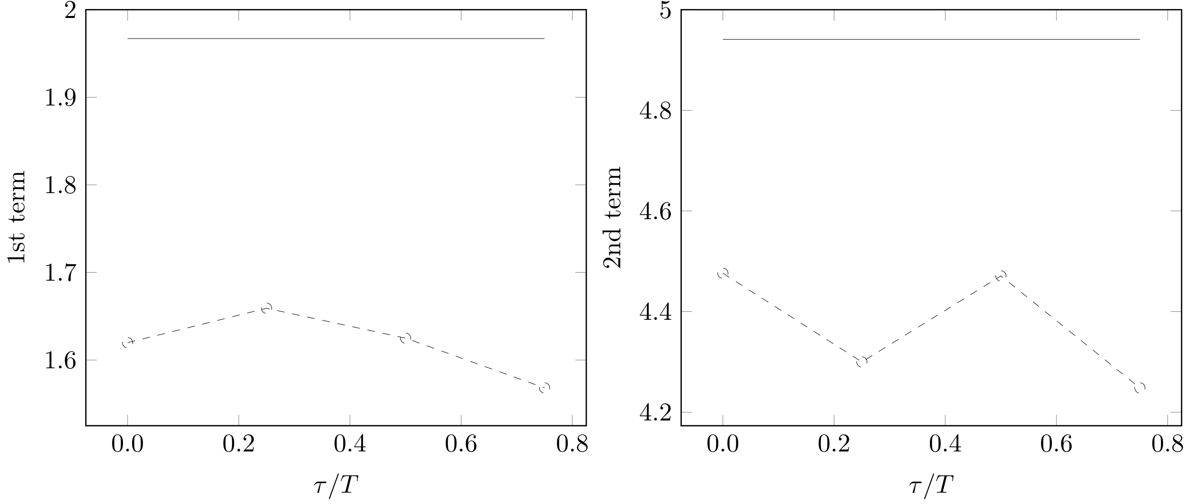

Figure 5.12: Continue in the next page

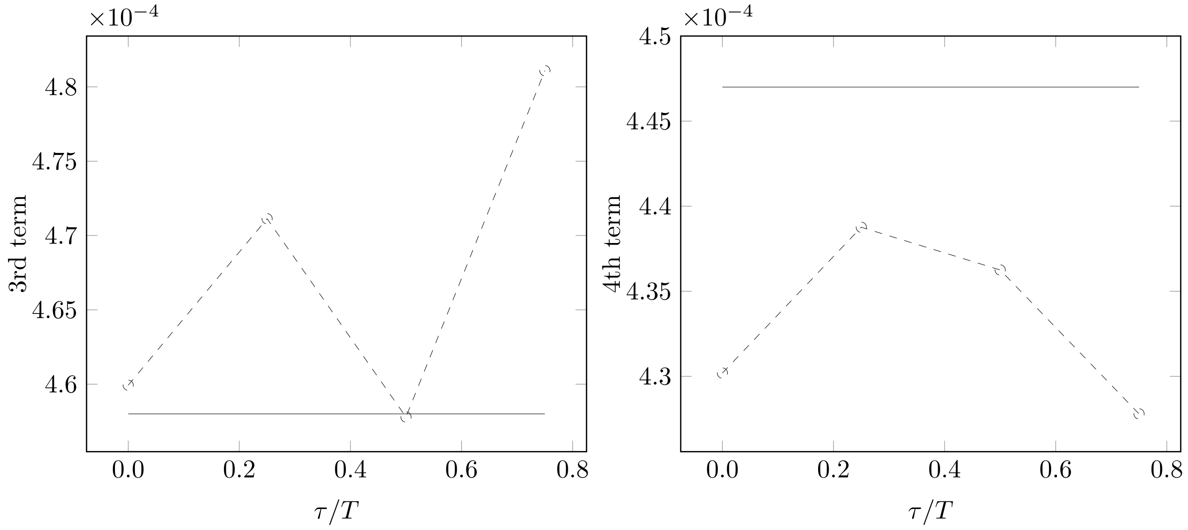

Figure 5.12: Terms of pressure drag equation (5.7) at different oscillation phases. Dashed line represents the controlled values for $\tau = 0$, $\tau = T/4$, $\tau = T/2$, $\tau = 3/4T$ while the solid line indicates the uncontrolled value.

The combined reductions of the first two terms in (5.7) causes the pressure drag reduction. As stated in section 5.4 the control does not affect significantly the shape of the dividing streamline and the velocities $\langle \widehat{u} \rangle$ and $\langle \widehat{v} \rangle$ along it. Hence, the reduction of $\frac{2}{L_x} \int_{l_s} \frac{1}{|\widehat{\mathbf{U}}|} \left(\langle \widehat{v} \rangle \langle \widehat{u_t u_t} \rangle - \langle \widehat{u} \rangle \langle \widehat{u_t v_t} \rangle \right) \mathrm{d}l$ and $\int_{l_s} \frac{\langle \widehat{p} \rangle \langle \widehat{v} \rangle}{|\widehat{\mathbf{U}}|} \mathrm{d}l$ is caused by the effect of the control on the Reynolds stress and the pressure along the dividing streamline respectively.

5.8.2 Total drag reduction

The time ensemble average of the total drag for the controlled flow is related to the product $\langle \widehat{u} \rangle \langle \widehat{v} \rangle$, the Reynolds stress $- \langle \widehat{u_t v_t} \rangle$ and $\frac{1}{Re_p} \frac{\partial \langle \widehat{u} \rangle}{\partial y} \Big|_h$ at $y = h$ via the following equation (refer to appendix F)

$$C_p(\tau) + C_f(\tau) \approx -\frac{L_y}{L_x} \int_{l_m} \langle \widehat{u} \rangle \langle \widehat{v} \rangle \, \mathrm{d}x - \frac{L_y}{L_x} \int_{l_m} \langle \widehat{u_t v_t} \rangle \, \mathrm{d}x + \frac{L_y}{L_x} \int_{l_m} \frac{1}{Re_p} \frac{\partial \langle \widehat{u} \rangle}{\partial y} \mathrm{d}x, \quad (5.8)$$

where l_m is the horizontal line connecting the crests of two consecutive bars along the same wall.

Figure 5.13 depicts the terms of (5.8) at different phases of the oscillation to highlight the origin of the total drag reduction. The first term is negative for both uncontrolled and controlled flow. The third term is due to viscous effects and gives a

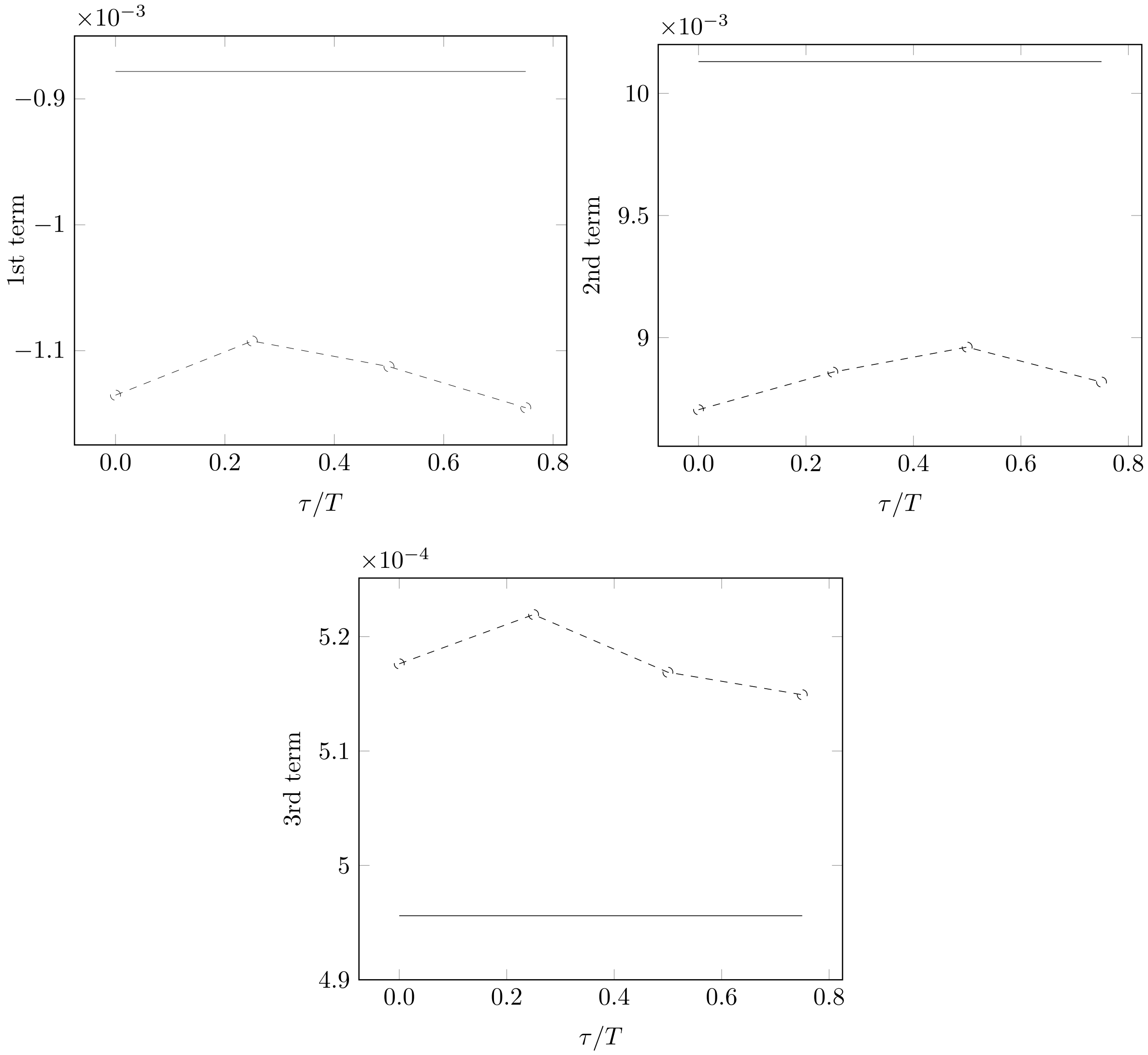

Figure 5.13: Terms of total drag equation (5.8) at different oscillation phases. Dashed line represents the controlled values for $\tau = 0$, $\tau = T/4$, $\tau = T/2$, $\tau = 3/4T$ while the solid line indicates the uncontrolled value.

negligible drag increase as it is small compared to the other terms. It is clear that the reduction of $-L_y/L_x \int_{l_m} \langle \widehat{u_t v_t} \rangle \, \mathrm{d}x$ is one order of magnitude larger than the one of $-\frac{L_y}{L_x} \int_{l_m} \langle \widehat{u} \rangle \langle \widehat{v} \rangle \, \mathrm{d}x$ thus confirming that the total drag reduction is mostly caused by a reduction of the Reynolds stress along l_m.

Chapter 6

Conclusions

A drag reduction study on a channel with square bars located on each wall has been conducted using direct numerical simulations. The flow is controlled via a spanwise oscillating pressure gradient. A maximum drag reduction of 12% was achieved. For the first time, we proved that a reduction of both pressure and skin-friction drag is possible contrariwise to vortex generators and jets that energize the fluid and increase skin-friction to control form drag.

The skin-friction drag is reduced because the shear stress along the cavity wall is decreased. This phenomenon takes place because the length of the cavity is large and the flow is able to reattach and, in this reattachment area, the mechanics of the drag reduction is similar to the one of a channel without bars.

The pressure drag reduction occurs because the control decreases the Reynolds stress and the pressure along the dividing streamline delimiting the separation area as proved by momentum conservation arguments.

It is also shown that the global drag reduction can be related to the alteration of the Reynolds stress along the horizontal line connecting the crests of the bars located on the same wall.

The power to control the flow has been quantified and compared with the drag reduction to find the net energy saved. Small energy savings were obtained. It is discovered that, for the amplitudes and periods considered, the solution of a related laminar flow gives an excellent prediction to the turbulent power spent. Further studies are necessary to determine if some combinations of parameters that reduce drag and minimize the control power do exist.

This technique is promising because, for the first time, it is shown that reduction of both pressure and skin-friction drag is possible, paving the way to more effective types of separation control. Future work should certainly be directed at improving the power balance to obtain a measurable net power saved. It is known that a travelling wave forcing is more efficient than spanwise oscillation (Quadrio et al., 2009) in reducing positive skin-friction. A possibility could be a spanwise pressure gradient of the form $\Pi_z(x,t) = A(x)\sin(k_x x - \omega_T t)$, where the function $A(x)$ would be constant far from the separation area and giving an effect similar to the one obtained by Quadrio et al. (2009). Recently, a paper of Banchetti et al. (2020) showed that travelling waves are able to reduce the drag around a curved wall giving a positive net energy balance. Their bump has a smooth shape and induces a mild separation downhill therefore differs from the present configuration where three large recirculation regions are created by intense separation.

Appendix A

Kim Moin method

The advection term is discretized using a second order Adam-Bashforth method while the viscous term is approximated via a Crank Nicholson scheme. In this section, we present an analysis performed by Shen (1991). The first fractional step is

$$\frac{\breve{\mathbf{U}} - \mathbf{U}^k}{\Delta t} = -\frac{3}{2}\left(\mathbf{U}^k \cdot \nabla\right)\mathbf{U}^k + \frac{1}{2}\left(\mathbf{U}^{k-1} \cdot \nabla\right)\mathbf{U}^{k-1} + \frac{1}{2Re}\left(\nabla^2 \breve{\mathbf{U}} + \nabla^2 \mathbf{U}^k\right). \tag{A.1}$$

The projection step can be written as

$$\breve{\mathbf{U}} = \mathbf{U}^{k+1} + \Delta t \nabla \phi^{k+1}. \tag{A.2}$$

By substituting (A.2) into (A.1) we get

$$\begin{aligned}\frac{\mathbf{U}^{k+1} - \mathbf{U}^k}{\Delta t} =& -\frac{3}{2}\left(\mathbf{U}^k \cdot \nabla\right)\mathbf{U}^k + \frac{1}{2}\left(\mathbf{U}^{k-1} \cdot \nabla\right)\mathbf{U}^{k-1} + \frac{1}{2Re}\left(\nabla^2 \mathbf{U}^{k+1} + \nabla^2 \mathbf{U}^k\right) \\ & - \nabla \phi^{k+1} - \frac{\Delta t}{2Re}\nabla^2\left(\nabla \phi^{k+1}\right).\end{aligned} \tag{A.3}$$

The substitution of the identity (**i**,**j**,**k** are the unit vectors in the x, y, z directions)

$$\begin{aligned}\nabla^2\left(\nabla \phi^{k+1}\right) &= \nabla^2\left(\frac{\partial \phi^{k+1}}{\partial x}\right)\mathbf{i} + \nabla^2\left(\frac{\partial \phi^{k+1}}{\partial y}\right)\mathbf{j} + \nabla^2\left(\frac{\partial \phi^{k+1}}{\partial z}\right)\mathbf{k} \\ &= \frac{\partial}{\partial x}\nabla^2 \phi^{k+1}\,\mathbf{i} + \frac{\partial}{\partial y}\nabla^2 \phi^{k+1}\,\mathbf{j} + \frac{\partial}{\partial z}\nabla^2 \phi^{k+1}\,\mathbf{k} = \nabla\left(\nabla^2 \phi^{k+1}\right)\end{aligned} \tag{A.4}$$

into (A.3) gives

$$\begin{aligned}\frac{\mathbf{U}^{k+1}-\mathbf{U}^{k}}{\Delta t} =& -\frac{3}{2}\left(\mathbf{U}^{k}\cdot\nabla\right)\mathbf{U}^{k}+\frac{1}{2}\left(\mathbf{U}^{k-1}\cdot\nabla\right)\mathbf{U}^{k-1}+\frac{1}{2Re}\left(\nabla^2\mathbf{U}^{k+1}+\nabla^2\mathbf{U}^{k}\right)\\ &-\nabla\phi^{k+1}-\frac{\Delta t}{2Re}\nabla\left(\nabla^2\phi^{k+1}\right)\end{aligned} \tag{A.5}$$

The Navier Stokes equations discretized read

$$\begin{aligned}\frac{\mathbf{U}^{k+1}-\mathbf{U}^{k}}{\Delta t} =& -\frac{3}{2}\left(\mathbf{U}^{k}\cdot\nabla\right)\mathbf{U}^{k}+\frac{1}{2}\left(\mathbf{U}^{k-1}\cdot\nabla\right)\mathbf{U}^{k-1}+\frac{1}{2Re}\left(\nabla^2\mathbf{U}^{k+1}+\nabla^2\mathbf{U}^{k}\right)\\ &-\nabla p^{k+1}\end{aligned} \tag{A.6}$$

By comparing (A.6) and (A.5) we obtain the pressure equation

$$p^{k+1}=\phi^{k+1}+\frac{\Delta t}{2Re}\left(\nabla^2\phi^{k+1}\right). \tag{A.7}$$

Appendix B

Drag components for a channel

The non-dimensional streamwise momentum equation in conservative form is

$$\frac{\partial u}{\partial t} + \nabla \cdot (u\,\mathbf{U}) = -\nabla \cdot (p\,\mathbf{i}) + \frac{1}{Re}\nabla \cdot (\nabla u)\,. \tag{B.1}$$

The integration of eq. B.1 on the fluid volume V_F and application of the divergence leads to

$$\frac{\partial}{\partial t}\int_{V_F} u\,\mathrm{d}V + \int_{S_F} u\,\mathbf{U}\,\cdot\mathbf{n}\,\mathrm{d}S = -\int_{S_F} p\,\mathbf{i}\,\cdot\mathbf{n}\,\mathrm{d}S + \frac{1}{Re}\int_{S_F} \nabla u\,\cdot\mathbf{n}\,\mathrm{d}S \tag{B.2}$$

The volume integral in (B.2) is null if simulations are performed at constant streamwise bulk velocity U_b (refer to C). The second integral can be split into contributions over boundary surfaces S_{xi}, S_{xf}, S_{wi}, S_{wf},S_{zi} and S_{zf} (refer to fig.B.1):

$$\begin{aligned}\int_{S_F} u\,\mathbf{U}\,\cdot\mathbf{n}\,\mathrm{d}S = &\int_{S_{xi}} u\,\mathbf{U}\,\cdot\mathbf{n}\,\mathrm{d}S + \int_{S_{xf}} u\,\mathbf{U}\,\cdot\mathbf{n}\,\mathrm{d}S + \int_{S_{zi}} u\,\mathbf{U}\,\cdot\mathbf{n}\,\mathrm{d}S + \\ &+ \int_{S_{zf}} u\,\mathbf{U}\,\cdot\mathbf{n}\,\mathrm{d}S + \int_{S_{wi}} u\,\mathbf{U}\,\cdot\mathbf{n}\,\mathrm{d}S + \int_{S_{wf}} u\,\mathbf{U}\,\cdot\mathbf{n}\,\mathrm{d}S.\end{aligned} \tag{B.3}$$

The sum of the first four terms in (B.3) is null because the flow is periodic over x and z, the last two are zero because of the no-penetration condition $\mathbf{U}\cdot\mathbf{n} = 0$.

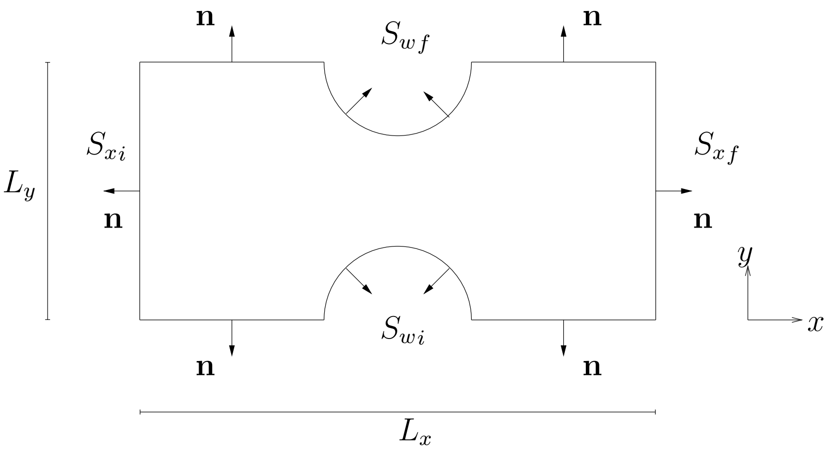

Figure B.1: Sketch for definition of drag components. S_{xi}, S_{xf}, S_{wi}, S_{wf} are boundary surfaces of the computational domain. L_x, L_y and L_z are the size of the computational box on x, y and z. $\mathbf{n}$ is the local normal unit vector pointing outside the domain. Boundary surfaces S_{zi}, S_{zf} lying in the plane x-y are not shown.

S_{xi}, S_{xf}, S_{wi} and S_{wf} are the only surfaces with a non-zero component of normal vector along x ($\mathbf{i} \cdot \mathbf{n} \neq 0$) hence the pressure integral in (B.2) is

$$\begin{aligned} -\int_{S_F} p\,\mathbf{i} \cdot \mathbf{n}\,\mathrm{d}S = & \int_{S_{xi}} p\,\mathrm{d}S - \int_{S_{xf}} p\,\mathrm{d}S + \\ & - \int_{S_{wi}} p\,\mathbf{i} \cdot \mathbf{n}\,\mathrm{d}S - \int_{S_{wf}} p\,\mathbf{i} \cdot \mathbf{n}\,\mathrm{d}S = \\ & - \Pi_x(t)\, L_x\, L_y\, L_z - \int_{S_{wi}} p\,\mathbf{i} \cdot \mathbf{n}\,\mathrm{d}S - \int_{S_{wf}} p\,\mathbf{i} \cdot \mathbf{n}\,\mathrm{d}S, \end{aligned} \tag{B.4}$$

where the definition of the pressure $p = \phi + \Pi_x x + \Pi_z z$ has been used to simplify the first two integrals. The last term in eq. B.2 is written as

$$\begin{aligned} \frac{1}{Re}\int_{S_F} \nabla u \cdot \mathbf{n}\,\mathrm{d}S = & -\frac{1}{Re}\int_{S_{xi}} \frac{\partial u}{\partial x}\,\mathrm{d}S + \frac{1}{Re}\int_{S_{xf}} \frac{\partial u}{\partial x}\,\mathrm{d}S - \frac{1}{Re}\int_{S_{zi}} \frac{\partial u}{\partial z}\,\mathrm{d}S + \\ & + \frac{1}{Re}\int_{S_{zf}} \frac{\partial u}{\partial z}\,\mathrm{d}S + \frac{1}{Re}\int_{S_{wi}} \frac{\partial u}{\partial \mathbf{n}}\,\mathrm{d}S + \frac{1}{Re}\int_{S_{wf}} \frac{\partial u}{\partial \mathbf{n}}\,\mathrm{d}S. \end{aligned} \tag{B.5}$$

where only the last two integrals give a nonzero contribution because of the same reasons of (B.3). The final streamwise momentum balance is then

$$- \Pi_x(t)\, L_x\, L_y\, L_z - \int_{S_w} P\,\mathbf{i} \cdot \mathbf{n}\,\mathrm{d}S + \frac{1}{Re}\int_{S_w} \frac{\partial u}{\partial \mathbf{n}}\,\mathrm{d}S = 0. \tag{B.6}$$

The surface S_w is defined as the union of the bottom (S_{wi}) and top (S_{wf}) wall surfaces. Eq. (B.6) represents the balance of forces acting on the fluid volume and drag components are the part of them exerted on walls changed of sign. Equation (B.6) is written as

$$C_p(t) + C_f(t) = -\Pi_x(t)\, L_y \tag{B.7a}$$

$$C_p(t) = \frac{1}{L_x\, L_z} \int_{S_w} p\, \mathbf{i} \cdot \mathbf{n}\, \mathrm{d}S, \qquad C_f(t) = -\frac{1}{L_x\, L_z} \int_{S_w} \frac{1}{Re} \frac{\partial u}{\partial \mathbf{n}}\, \mathrm{d}S, \tag{B.7b}$$

where pressure and skin-friction drag coefficients $C_p(t)$ and $C_f(t)$ are defined.

Channel with smooth walls

A channel with smooth walls has zero pressure drag because the unit vector normal at walls is on the y direction ($\mathbf{n} = \mp\mathbf{j}$) while skin-friction drag is

$$C_f(t) = \frac{1}{L_x\, L_z} \int_0^{L_x} \int_0^{L_z} \frac{1}{Re} \left(\left.\frac{\partial u}{\partial y}\right|_{y=0} - \left.\frac{\partial u}{\partial y}\right|_{y=2} \right) \mathrm{d}x\mathrm{d}z \tag{B.8}$$

Channel with square bars

For the channel with square bars pressure drag is due to vertical surfaces of the bars

$$C_p(t) = \frac{1}{L_x\, L_z} \sum_{i=1}^{N_{bars}} \left(\int_0^{h} \int_0^{L_z} \Delta p_i\, \mathrm{d}y\, \mathrm{d}z + \int_{2+h}^{2+2h} \int_0^{L_z} \Delta p_i\, \mathrm{d}y\, \mathrm{d}z \right) \tag{B.9}$$

where Δp_i is the difference between pressures at $x = x_a$ and $x = x_b$ (see fig. B.2). The skin-friction, obtained by integrating the shear stress over horizontal surfaces, can be split into a crest contribution ($x_a \leq x \leq x_b$, $y =h$, $2 + h$)

$$C_{f,cr}(t) = \frac{1}{L_x\, L_z} \sum_{i=1}^{N_{bars}} \int_{x_a}^{x_b} \int_0^{L_z} \frac{1}{Re} \left(\left.\frac{\partial u}{\partial y}\right|_{y=h} - \left.\frac{\partial u}{\partial y}\right|_{y=2+h} \right) \mathrm{d}x\, \mathrm{d}z, \tag{B.10}$$

and cavity one ($x_s \leq x \leq x_a$, $x_b \leq x \leq x_e$, $y =0$, $2 + 2h$)

$$\begin{aligned} C_{f,ca}(t) = \frac{1}{L_x\, L_z} \sum_{i=1}^{N_{bars}} \int_{x_s}^{x_a} \int_0^{L_z} \frac{1}{Re} \left(\left.\frac{\partial u}{\partial y}\right|_{y=0} - \left.\frac{\partial u}{\partial y}\right|_{y=2+2h} \right) \mathrm{d}x\, \mathrm{d}z + \\ + \int_{x_b}^{x_e} \int_0^{L_z} \frac{1}{Re} \left(\left.\frac{\partial u}{\partial y}\right|_{y=0} - \left.\frac{\partial U}{\partial y}\right|_{y=2+2h} \right) \mathrm{d}x\, \mathrm{d}z, \end{aligned} \tag{B.11}$$

and the global skin-friction coefficient is defined as $C_f(t) = C_{f,cr}(t) + C_{f,ca}(t)$.

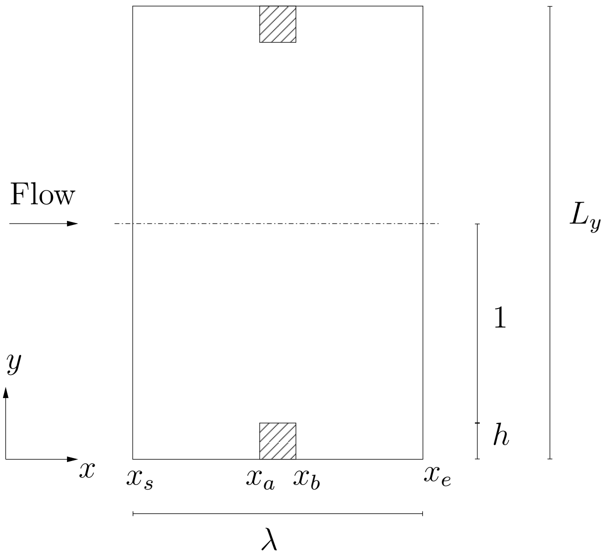

Figure B.2: Configuration of the channel with bars. Only one bar section of length $\lambda = L_x/N_{bars}$ is depicted. h is the height of the square bar. The coordinates x_a and x_b indicate the streamwise locations of the left and right vertical sides of the bar. The coordinates x_s and x_e delimit the section defined by one bar.

Appendix C

Bulk velocities and mass flow rate

Integrating the equation of conservation of mass over the volume $V_F(x)$ depicted in fig. C.1 and using the divergence theorem gives

$$\int_{V_F(x)} \nabla \cdot \mathbf{U} \, \mathrm{d}V = \int_{S_F(x)} \mathbf{U} \cdot \mathbf{n} \, \mathrm{d}S = 0. \tag{C.1}$$

Equation C.1 can be split over the boundary surfaces S_{xi}, $S_x(x)$, $S_{wi}(x)$, $S_{wf}(x)$, $S_{zi}(x)$ and $S_{zf}(x)$to obtain

$$\begin{aligned} \int_{S_F(x)} \mathbf{U} \cdot \mathbf{n} \, \mathrm{d}S = & \int_{S_x(x)} u \, \mathrm{d}S - \int_{S_{xi}} u \, \mathrm{d}S + \int_{S_{wf}(x)} \mathbf{u} \cdot \mathbf{n} \, \mathrm{d}S - \int_{S_{wi}(x)} \mathbf{u} \cdot \mathbf{n} \, \mathrm{d}S + \\ & + \int_{S_{zf}(x)} w \, \mathrm{d}S - \int_{S_{zi}(x)} w \, \mathrm{d}S = 0 \end{aligned} \tag{C.2}$$

The third and fourth integral in (C.2) are null because of the no-penetration condition $\mathbf{U} \cdot \mathbf{n} = 0$. The difference of the last two integrals is zero because w is a periodic function of z and we get

$$\int_{S_x(x)} u \, \mathrm{d}S = \int_{S_{xi}} u \, \mathrm{d}S. \tag{C.3}$$

The surface $S_x(x)$ is generic thus the integral of the streamwise velocity on section of normal $\mathbf{i}$ has the same value for every x, i.e.

$$\int_{S_x(x)} u \, \mathrm{d}S = \int_{S_{xi}} u \, \mathrm{d}S = \int_{S_{xf}} u \, \mathrm{d}S. \tag{C.4}$$

We define the streamwise bulk velocity as the average of u over the fluid volume V_F in fig. B.1:

$$U_b = \frac{1}{V_F}\int_{V_F} u\,\mathrm{d}V = \frac{1}{V_F}\int_0^{L_x}\mathrm{d}x\int_{S_x(x)} u\,\mathrm{d}S = \frac{L_x}{V_F}\int_{S_{xf}} u\,\mathrm{d}S \tag{C.5}$$

Equation (C.5) is a statement of conservation of mass in integral form. If we consider the definition of non-dimensional mass flow rate

$$\dot{m} = \frac{\dot{m}^*}{\rho^*\,U_p^*\,{\delta^*}^2} = \frac{\int_{S_{xf}^*}\rho^* u^* \mathrm{d}\sigma^*}{\rho^*\,U_p^*\,{\delta^*}^2} = \int_{S_{xf}} u\,\mathrm{d}S \tag{C.6}$$

we can write eq. (C.5) as

$$U_b = \frac{U_b^*}{U_p^*} = \frac{L_x}{V_F}\,\dot{m} = \frac{L_x^*}{V_F^*}\,\frac{\dot{m}^*}{\rho^* U_p^*}. \tag{C.7}$$

If the whole fluid volume V_F is split with a plane of normal $\mathbf{k}$ to create the volume $V_F(z)$ then the previous procedure indicates that the integral of the spanwise velocity w over any section of normal $\mathbf{k}$ is the same for any z

$$\int_{S_z(z)} w\,\mathrm{d}S = \int_{S_{zi}} w\,\mathrm{d}S = \int_{S_{zf}} w\,\mathrm{d}S, \tag{C.8}$$

and we define a spanwise bulk velocity as the average of w over V_F

$$W_b = \frac{1}{V_F}\int_{V_F} w\,\mathrm{d}V = \frac{1}{V_F}\int_0^{L_z}\mathrm{d}z\int_{S_z(z)} w\,\mathrm{d}S = \frac{L_z}{V_F}\int_{S_{zf}} w\,\mathrm{d}S \tag{C.9}$$

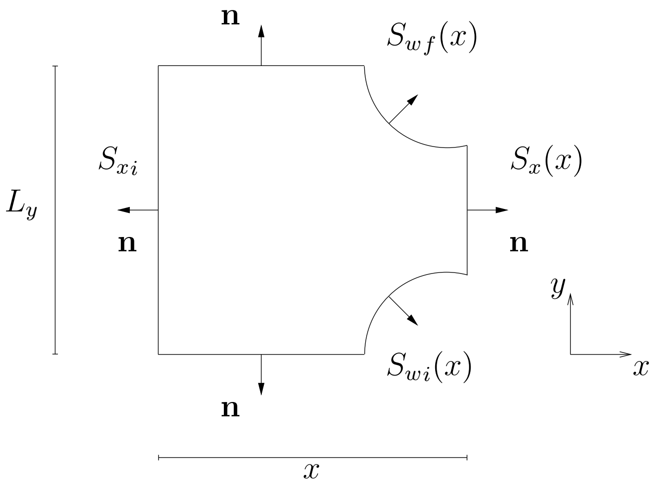

Figure C.1: Fluid domain $V_F(x)$ obtained by splitting the one of fig. B.1 with a vertical plane. S_{xi}, $S_x(x)$, $S_{wi}(x)$, $S_{wf}(x)$ are boundary surfaces. L_x, L_y and L_z are the size on x, y and z axis. $\mathbf{n}$ is the local normal unit vector pointing outside the domain. Boundary surfaces $S_{zi}(x)$, $S_{zf}(x)$ belonging to the planes x-y are not shown.

Appendix D

Error estimation of the coefficients

The computed reductions of drag and pressure flux coefficients (refer to section 3.3.2) are affected by the time-averaging error due to a finite number of time samplings used and the error due to the grid resolution. This analysis is performed only for the case giving the largest drag reduction ($A = 3.0$, $T = 2.3$) because the main results of this work are related to this case and because the simulations are computationally expensive.

Tab. D.1 shows the time averaging error as function of the time window NT used for the average computation. Each error is determined by comparing the reduction computed by averaging for a time NT and the reduction presented in tab. 5.2. A time window of $4T$ is enough to obtain time averaging errors less than 1%, in particular the global drag reduction $R(\%)$ shows a negligible time-averaging error (0.03%).

N	$\mathcal{E}_t C_{f,cr}(\%)$	$\mathcal{E}_t C_{f,ca}(\%)$	$\mathcal{E}_t C_f(\%)$	$\mathcal{E}_t C_{pl}(\%)$	$\mathcal{E}_t C_{pr}(\%)$	$\mathcal{E}_t C_p(\%)$	$\mathcal{E}_t R(\%)$
1	1.19	6.22	6.65	2.08	5.85	3.51	1.58
2	0.35	3.67	3.90	0.88	3.69	1.95	0.85
3	0.91	1.84	1.89	0.81	0.17	0.44	0.71
4	0.47	0.95	0.98	0.08	0.59	0.27	0.03

Table D.1: Estimated time-averaging error as function of the time window used for the average. The error of each percentage variation of the drag coefficients are computed. N is the number of periods and NT is the time average window.

Tab. D.2 shows the percentage of drag reductions as function of the grid resolution.

Each percentage is computed by comparing the related controlled and uncontrolled drag component at the same resolution.

lx	$\mathcal{R}_{cr}(\%)$	$\mathcal{R}_{ca}(\%)$	$\mathcal{R}_{f}(\%)$	$\mathcal{R}_{pl}(\%)$	$\mathcal{R}_{pr}(\%)$	$\mathcal{R}_{p}(\%)$	$\mathcal{R}(\%)$
6	2.64	22.84	24.02	6.64	14.10	9.48	12.26
8	5.18	19.09	19.92	5.45	14.28	8.80	10.89
10	3.59	20.38	21.37	6.81	15.83	10.25	12.32

Table D.2: Drag reductions as function of the number of GLL the points lx along any side of a spectral element.

Tab. D.3 presents the estimated error due to the grid resolution identified by the equation $\mathcal{E}_{lx,g}(\%) = \max\{|\mathcal{R}_8(\%) - \mathcal{R}_6(\%)|, |\mathcal{R}_{10}(\%) - \mathcal{R}_6(\%)|\}$, where $\mathcal{E}_{lx,g}(\%)$ is the error, $\mathcal{R}_6(\%)$, $\mathcal{R}_8(\%)$ and $\mathcal{R}_{10}(\%)$ are the reductions of a generic drag coefficient computed using 6, 8 and 10 GLL points along the edge of any spectral element, respectively.

$\mathcal{E}_{lx,cr}(\%)$	$\mathcal{E}_{lx,ca}(\%)$	$\mathcal{E}_{lx,f}(\%)$	$\mathcal{E}_{lx,pl}(\%)$	$\mathcal{E}_{lx,pr}(\%)$	$\mathcal{E}_{lx,p}(\%)$	$\mathcal{E}_{lx}(\%)$
2.54	3.75	4.10	1.19	1.72	0.77	1.37

Table D.3: Estimated grid resolution error for the percentages of drag reductions.

Tab. D.4 shows a conservative estimate of the total error due the time-averaging and to the grid resolution. Each value is computed by adding the related values of the last row of tab. D.1 and those of tab. D.3.

$\mathcal{E}_{cr}(\%)$	$\mathcal{E}_{ca}(\%)$	$\mathcal{E}_{f}(\%)$	$\mathcal{E}_{pl}(\%)$	$\mathcal{E}_{pr}(\%)$	$\mathcal{E}_{p}(\%)$	$\mathcal{E}(\%)$
3.01	4.7	5.08	1.27	2.31	1.04	1.4

Table D.4: Estimated grid resolution error for the percentages of drag reductions.

Appendix E

Energy to drive the flow along the streamwise and spanwise directions

The energy per unit of mass to move the fluid along the streamwise direction can be calculated using the first term of eq. 1-108 in Hinze (1975) averaged over the fluid volume V_F

$$\mathrm{E}_x = \frac{1}{V_F}\int_{V_F} -\frac{\partial}{\partial x}\,(up)\;\mathrm{d}V = -\frac{1}{V_F}\int_{V_F} \nabla\cdot(up\,\mathbf{i})\;\mathrm{d}V. \tag{E.1}$$

Applying the divergence theorem to (E.1) we get

$$\mathrm{E}_x = -\frac{1}{V_F}\int_{S_F} up\,\mathbf{i}\,\cdot\mathbf{n}\,\mathrm{d}S. \tag{E.2}$$

The boundary surfaces for which $\mathbf{i}\cdot\mathbf{n}\neq 0$ are S_{xi}, S_{xf}, $S_w = S_{wi}\cup S_{wf}$ (refer to fig. B.1) and

$$\mathrm{E}_x = -\frac{1}{V_F}\left(\int_{S_{xf}} up\,\mathrm{d}S - \int_{S_{xi}} up\,\mathrm{d}S + \int_{S_w} up\,\mathbf{i}\,\cdot\mathbf{n}\,\mathrm{d}S\right). \tag{E.3}$$

The difference of the integrals over S_{xf} and S_{xi} in (E.3), evaluated by using the pressure expression $p=\phi+\Pi_x\,x+\Pi_z\,z$, is

$$\begin{aligned}\int_{S_{xf}} up\,\mathrm{d}S - \int_{S_{xi}} up\,\mathrm{d}S = \int_{S_{xf}} u\phi\,\mathrm{d}S - \int_{S_{xi}} u\phi\,\mathrm{d}S + \Pi_x\,L_x\int_{S_{xf}} u\,\mathrm{d}S+\\ -\,\Pi_x\,0\int_{S_{xi}} u\,\mathrm{d}S + \Pi_z\int_{S_{xf}} u\,z\,\mathrm{d}S - \Pi_z\int_{S_{xi}} u\,z\,\mathrm{d}S.\end{aligned} \tag{E.4}$$

The difference of the first two and last two terms (E.4) are zero because u and ϕ are periodic along x (note that $x = 0$ at S_{xi} and $x = L_x$ at S_{xf}) and

$$\int_{S_{xf}} up \, \mathrm{d}S - \int_{S_{xi}} up \, \mathrm{d}S = \Pi_x \, L_x \int_{S_{xf}} u \, \mathrm{d}S. \tag{E.5}$$

Equation (E.5) can be written in terms of the streamwise bulk velocity U_b using eq. (C.5)

$$\int_{S_{xf}} up \, \mathrm{d}S - \int_{S_{xi}} up \, \mathrm{d}S = \Pi_x \, U_b \, V_F. \tag{E.6}$$

By substituting eq. (E.6) into eq. (E.3) gives:

$$\mathrm{E}_x = -\Pi_x \, U_b - \frac{1}{V_F} \int_{S_w} up \, \mathbf{i} \cdot \mathbf{n} \, \mathrm{d}S \tag{E.7}$$

For a channel with smooth walls the normal vector at S_w is oriented along the y direction ($\mathbf{n} = \mathbf{j}$), a channel with bars has zero velocities at S_w: in either cases the integral in eq. (E.7) vanishes. The energy to move the flow along the streamwise direction is therefore

$$\mathrm{E}_x = -\Pi_x \, U_b. \tag{E.8}$$

The power P_x to drive the flow over x is the time average of equation (E.8)

$$\mathrm{P}_x = \frac{1}{t_f - t_i} \int_{t_i}^{t_f} \mathrm{E}_x(t) \mathrm{d}t = -\frac{U_b}{t_f - t_i} \int_{t_i}^{t_f} \Pi_x(t) \mathrm{d}t = -\Pi_x U_b, \tag{E.9}$$

where U_b does not depend on t because we perform simulations at constant streamwise bulk velocity.

The energy per unit of mass made by the spanwise pressure gradient can be evaluated in a analogous manner E_x

$$\mathrm{E}_z = -\frac{1}{V_F} \int_{S_F} wp \, \mathbf{k} \cdot \mathbf{n} \, \mathrm{d}S. \tag{E.10}$$

The only boundary surfaces with normal parallel to the spanwise direction are S_{zi} and S_{zf} hence (E.10) is simplified as

$$\mathrm{E}_z = -\frac{1}{V_F} \left(\int_{S_{zf}} wp \, \mathrm{d}S - \int_{S_{zi}} wp \, \mathrm{d}S \right). \tag{E.11}$$

The difference of integrals over S_{zf} and S_{zi} in (E.11) is evaluated by using the pressure expression $p = \phi + \Pi_x\, x + \Pi_z\, z$ to obtain

$$\begin{aligned}\int_{S_{zf}} wp\,\mathrm{d}S - \int_{S_{zi}} wp\,\mathrm{d}S = \int_{S_{zf}} p\phi\,\mathrm{d}S - \int_{S_{zi}} w\phi\,\mathrm{d}S + \Pi_z\, L_z \int_{S_{zf}} w\,\mathrm{d}S + \\ - \Pi_z\, 0 \int_{S_{xi}} w\,\mathrm{d}S + \Pi_x \int_{S_{zf}} w\,x\,\mathrm{d}S - \Pi_x \int_{S_{zi}} w\,x\,\mathrm{d}S.\end{aligned} \tag{E.12}$$

The difference of the first two and last two terms in (E.12) are zero because w and ϕ are periodic along z (note that $z = 0$ at S_{zi} and $z = L_z$ at S_{zf}) and

$$\int_{S_{zf}} wp\,\mathrm{d}S - \int_{S_{zi}} wp\,\mathrm{d}S = \Pi_z\, L_z \int_{S_{xf}} w\,\mathrm{d}S. \tag{E.13}$$

Equation (E.13) can be written in terms of the spanwise bulk velocity W_b by using eq. (C.9)

$$\int_{S_{zf}} wp\,\mathrm{d}S - \int_{S_{zi}} wp\,\mathrm{d}S = \Pi_z\, W_b\, V_F \tag{E.14}$$

By substituting eq. (E.14) into eq. (E.11) gives

$$\mathrm{E}_z = -\Pi_z\, W_b \tag{E.15}$$

The power P_z to drive the flow over z is the time average of equation (E.15)

$$\mathrm{P}_z = \frac{1}{t_f - t_i} \int_{t_i}^{t_f} \mathrm{E}_z(t)\mathrm{d}t = -\frac{1}{t_f - t_i} \int_{t_i}^{t_f} \Pi_z(t) W_b(t)\mathrm{d}t \tag{E.16}$$

Appendix F

Drag dependence on Reynolds stress

Inspired by the paper of Gharib and Roshko (1987) we consider the time ensemble and z averaged streamwise momentum equation (note that $\frac{\partial \langle \widehat{u} \rangle}{\partial \tau} = 0$ as shown by fig. 5.9)

$$\frac{\partial \langle \widehat{uu} \rangle}{\partial x} + \frac{\partial \langle \widehat{uv} \rangle}{\partial y} = -\frac{\partial \langle \widehat{p} \rangle}{\partial x} + \frac{1}{Re_p} \left(\frac{\partial^2 \langle \widehat{u} \rangle}{\partial x^2} + \frac{\partial^2 \langle \widehat{u} \rangle}{\partial y^2} \right). \tag{F.1}$$

By defining the vector $\langle \widehat{uu} \rangle \, \mathbf{i} + \langle \widehat{uv} \rangle \, \mathbf{j}$ and noticing that $\frac{\partial \langle \widehat{p} \rangle}{\partial x} = \nabla \cdot (\langle \widehat{p} \rangle \, \mathbf{i})$ and $\frac{\partial^2}{\partial x^2} + \frac{\partial^2}{\partial y^2} = \nabla \cdot \nabla$ we can write (F.1) as

$$\nabla \cdot (\langle \widehat{uu} \rangle \, \mathbf{i} + \langle \widehat{uv} \rangle \, \mathbf{j}) = \nabla \cdot (- \langle \widehat{p} \rangle \, \mathbf{i} + \frac{1}{Re_p} \nabla \langle \widehat{u} \rangle). \tag{F.2}$$

The integration of (F.2) on a generic surface S_z with boundary ∂S_z lying on the plane $x - y$ and the application of the divergence theorem leads to

$$\int_{\partial S_z} (\langle \widehat{uu} \rangle \, \mathbf{i} + \langle \widehat{uv} \rangle \, \mathbf{j}) \cdot \mathbf{n} \, \mathrm{d}l = - \int_{\partial S_z} \langle \widehat{p} \rangle \, \mathbf{i} \cdot \mathbf{n} \, \mathrm{d}l + \int_{\partial S_z} \frac{1}{Re_p} \nabla \langle \widehat{u} \rangle \cdot \mathbf{n} \, \mathrm{d}l. \tag{F.3}$$

F.1 Pressure drag

In order to quantify the downstream and upstream contribution to the pressure drag of the vertical surfaces of the bar we consider the two recirculation areas depicted in figure F.1. The first one is delimited by the dividing streamline from the corner to $x = x_r$ while the last one is enclosed by the streamline from $x = x_s$ to the bar corner.

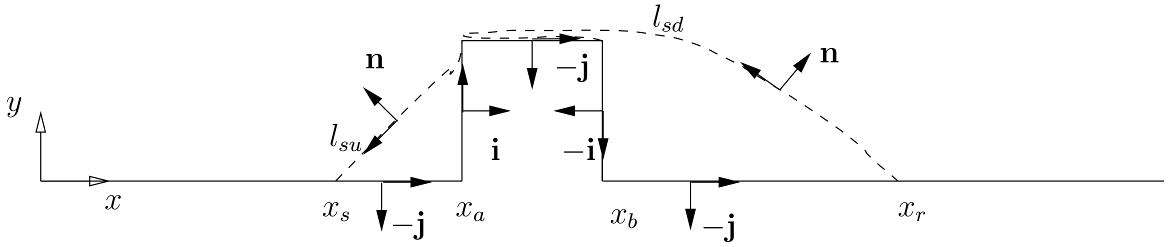

Figure F.1: Sketch of the separation area. The dividing streamlines are indicated by the dashed lines. l_{su} and l_{sd} are the portions of the streamline upstream and downstream the bar respectively.

Downstream recirculation area

The equation (F.3) is written as

$$\begin{aligned}\int_{l_{sd}} \left(\langle\widehat{uu}\rangle\,\mathbf{i} + \langle\widehat{uv}\rangle\,\mathbf{j}\right)\cdot\mathbf{n}\,\mathrm{d}l = \int_0^h \langle\widehat{p}\rangle\big|_{x_b}\mathrm{d}y - \int_{l_{sd}}\langle\widehat{p}\rangle\,\mathbf{i}\cdot\mathbf{n}\,\mathrm{d}l + \int_{l_{sd}}\frac{1}{Re_p}\nabla\langle\widehat{u}\rangle\cdot\mathbf{n}\,\mathrm{d}l \\ + \int_0^h \frac{1}{Re_p}\frac{\partial\langle\widehat{u}\rangle}{\partial x}\Big|_{x_b}\mathrm{d}y - \int_{x_b}^{x_r}\frac{1}{Re_p}\frac{\partial\langle\widehat{u}\rangle}{\partial y}\Big|_0\mathrm{d}x,\end{aligned} \tag{F.4}$$

where l_{sd} indicates the dividing streamline delimiting the downstream recirculation area. A streamline is by definition a line whose unit tangent vector is parallel to the velocity vector, therefore the tangent and normal unit vectors are

$$\mathbf{t} = -\frac{\langle\widehat{u}\rangle\,\mathbf{i} + \langle\widehat{v}\rangle\,\mathbf{j}}{\sqrt{\langle\widehat{u}\rangle^2 + \langle\widehat{v}\rangle^2}}, \qquad \mathbf{n} = \frac{-\langle\widehat{v}\rangle\,\mathbf{i} + \langle\widehat{u}\rangle\,\mathbf{j}}{\sqrt{\langle\widehat{u}\rangle^2 + \langle\widehat{v}\rangle^2}}. \tag{F.5}$$

Note that the minus in the first of (F.5) is due to the flow direction along the streamline being opposite to the direction of the tangent vector used for the divergence theorem and depicted in fig. F.1.

The components of **n** along the x and y axes are therefore

$$\mathbf{i}\cdot\mathbf{n} = -\frac{\langle\widehat{v}\rangle}{\sqrt{\langle\widehat{u}\rangle^2 + \langle\widehat{v}\rangle^2}} = -\frac{\langle\widehat{v}\rangle}{|\widehat{\mathbf{U}}|}, \qquad \mathbf{j}\cdot\mathbf{n} = \frac{\langle\widehat{u}\rangle}{\sqrt{\langle\widehat{u}\rangle^2 + \langle\widehat{v}\rangle^2}} = \frac{\langle\widehat{u}\rangle}{|\widehat{\mathbf{U}}|}, \tag{F.6}$$

where the modulo $|\widehat{\mathbf{U}}| = \sqrt{\langle\widehat{u}\rangle^2 + \langle\widehat{v}\rangle^2}$ of the vector $\widehat{\mathbf{U}} = -\langle\widehat{v}\rangle\,\mathbf{i} + \langle\widehat{u}\rangle\,\mathbf{j}$ has been introduced to simplify the notation. By considering (F.6) and applying the Reynolds decomposition we obtain

$$\left\langle \widehat{uu} \right\rangle \mathbf{i} \cdot \mathbf{n} = -\frac{1}{|\widehat{\mathbf{U}}|} \left(\left\langle \widehat{v} \right\rangle \left\langle \widehat{u} \right\rangle^2 + \left\langle \widehat{v} \right\rangle \left\langle \widehat{u_t u_t} \right\rangle \right), \quad \left\langle \widehat{uv} \right\rangle \mathbf{j} \cdot \mathbf{n} = \frac{1}{|\widehat{\mathbf{U}}|} \left(\left\langle \widehat{v} \right\rangle \left\langle \widehat{u} \right\rangle^2 + \left\langle \widehat{u} \right\rangle \left\langle \widehat{u_t v_t} \right\rangle \right), \tag{F.7}$$

and the first term of (F.4) reads

$$\int_{l_{sd}} \left(\left\langle \widehat{uu} \right\rangle \mathbf{i} + \left\langle \widehat{uv} \right\rangle \mathbf{j} \right) \cdot \mathbf{n} \, \mathrm{d}l = -\int_{l_{sd}} \frac{1}{|\widehat{\mathbf{U}}|} \left(\left\langle \widehat{v} \right\rangle \left\langle \widehat{u_t u_t} \right\rangle - \left\langle \widehat{u} \right\rangle \left\langle \widehat{u_t v_t} \right\rangle \right) \mathrm{d}l. \tag{F.8}$$

The second term on the right hand side of (F.4) is

$$-\int_{l_{sd}} \left\langle \widehat{p} \right\rangle \mathbf{i} \cdot \mathbf{n} \, \mathrm{d}l = \int_{l_{sd}} \frac{\left\langle \widehat{p} \right\rangle \left\langle \widehat{v} \right\rangle}{|\widehat{\mathbf{U}}|} \mathrm{d}l. \tag{F.9}$$

The third term on the right hand side of (F.4) is simplified by taking into account (F.7) and continuity in the following way

$$\begin{aligned}
\int_{l_{sd}} \frac{1}{Re_p} \nabla \left\langle \widehat{u} \right\rangle \cdot \mathbf{n} \, \mathrm{d}l &= \frac{1}{Re_p} \int_{l_{sd}} \left(\frac{\partial \left\langle \widehat{u} \right\rangle}{\partial x} \mathbf{i} + \frac{\partial \left\langle \widehat{u} \right\rangle}{\partial y} \mathbf{j} \right) \cdot \mathbf{n} \, \mathrm{d}l = \\
&= \frac{1}{Re_p} \int_{l_{sd}} \frac{1}{|\widehat{\mathbf{U}}|} \left(-\left\langle \widehat{v} \right\rangle \frac{\partial \left\langle \widehat{u} \right\rangle}{\partial x} + \left\langle \widehat{u} \right\rangle \frac{\partial \left\langle \widehat{u} \right\rangle}{\partial y} \right) \mathrm{d}l = \\
&= \frac{1}{Re_p} \int_{l_{sd}} \frac{1}{|\widehat{\mathbf{U}}|} \left(\left\langle \widehat{v} \right\rangle \frac{\partial \left\langle \widehat{v} \right\rangle}{\partial y} + \left\langle \widehat{u} \right\rangle \frac{\partial \left\langle \widehat{u} \right\rangle}{\partial y} \right) \mathrm{d}l = \\
&= \frac{1}{Re_p} \int_{l_{sd}} \frac{1}{2|\widehat{\mathbf{U}}|} \frac{\partial}{\partial y} \left(\left\langle \widehat{u} \right\rangle^2 + \left\langle \widehat{v} \right\rangle^2 \right) \mathrm{d}l = \\
&= \frac{1}{Re_p} \int_{l_{sd}} \frac{1}{2|\widehat{\mathbf{U}}|} \frac{\partial |\widehat{\mathbf{U}}|^2}{\partial y} \mathrm{d}l = \frac{1}{Re_p} \int_{l_{sd}} \frac{\partial |\widehat{\mathbf{U}}|}{\partial y} \mathrm{d}l.
\end{aligned} \tag{F.10}$$

The fourth term on the right hand side of (F.4) is zero because of continuity $\frac{\partial \left\langle \widehat{u} \right\rangle}{\partial x} = -\frac{\partial \left\langle \widehat{v} \right\rangle}{\partial y}$ and the no-slip condition. By considering (F.8)-(F.10) we obtain the final momentum balance

$$\begin{aligned}
-\int_0^h \left\langle \widehat{p} \right\rangle \big|_{x_b} \mathrm{d}y = &\int_{l_{sd}} \frac{1}{|\widehat{\mathbf{U}}|} \left(\left\langle \widehat{v} \right\rangle \left\langle \widehat{u_t u_t} \right\rangle - \left\langle \widehat{u} \right\rangle \left\langle \widehat{u_t v_t} \right\rangle \right) \mathrm{d}l + \int_{l_{sd}} \frac{\left\langle \widehat{p} \right\rangle \left\langle \widehat{v} \right\rangle}{|\widehat{\mathbf{U}}|} \mathrm{d}l \\
&+ \frac{1}{Re_p} \int_{l_{sd}} \frac{\partial |\widehat{\mathbf{U}}|}{\partial y} \mathrm{d}l - \int_{x_b}^{x_r} \frac{1}{Re_p} \frac{\partial \left\langle \widehat{u} \right\rangle}{\partial y} \Big|_0 \mathrm{d}x.
\end{aligned} \tag{F.11}$$

Upstream recirculation area

The equation (F.3) is written as

$$
\begin{aligned}
\int_{l_{su}} \left(\langle \widehat{uu} \rangle \mathbf{i} + \langle \widehat{uv} \rangle \mathbf{j} \right) \cdot \mathbf{n} \, \mathrm{d}l = & - \int_0^h \langle \widehat{p} \rangle \big|_{x_a} \mathrm{d}y - \int_{l_{su}} \langle \widehat{p} \rangle \, \mathbf{i} \cdot \mathbf{n} \, \mathrm{d}l + \int_{l_{su}} \frac{1}{Re_p} \nabla \langle \widehat{u} \rangle \cdot \mathbf{n} \, \mathrm{d}l \\
& + \int_0^h \frac{1}{Re_p} \frac{\partial \langle \widehat{u} \rangle}{\partial x} \Big|_{x_a} \mathrm{d}y \; - \int_{x_s}^{x_a} \frac{1}{Re_p} \frac{\partial \langle \widehat{u} \rangle}{\partial y} \Big|_0 \mathrm{d}x.
\end{aligned}
\tag{F.12}
$$

By reasoning as the previous section we obtain the momentum balance

$$
\begin{aligned}
\int_0^h \langle \widehat{p} \rangle \big|_{x_a} \mathrm{d}y = & + \int_{l_{su}} \frac{1}{|\widehat{\mathbf{U}}|} \left(\langle \widehat{v} \rangle \langle \widehat{u_t u_t} \rangle - \langle \widehat{u} \rangle \langle \widehat{u_t v_t} \rangle \right) \mathrm{d}l + \int_{l_{su}} \frac{\langle \widehat{p} \rangle \langle \widehat{v} \rangle}{|\widehat{\mathbf{U}}|} \mathrm{d}l \\
& + \frac{1}{Re_p} \int_{l_{su}} \frac{\partial |\widehat{\mathbf{U}}|}{\partial y} \mathrm{d}l - \int_{x_s}^{x_a} \frac{1}{Re_p} \frac{\partial \langle \widehat{u} \rangle}{\partial y} \Big|_0 \mathrm{d}x.
\end{aligned}
\tag{F.13}
$$

Pressure drag balance

By summing (F.11) and (F.13) and dividing by L_x we obtain the pressure drag balance

$$
\begin{aligned}
\frac{1}{L_x} \int_0^h \langle \widehat{p} \rangle \big|_{x_a} - \langle \widehat{p} \rangle \big|_{x_b} \mathrm{d}y = & \frac{1}{L_x} \int_{l_s} \frac{1}{|\widehat{\mathbf{U}}|} \left(\langle \widehat{v} \rangle \langle \widehat{u_t u_t} \rangle - \langle \widehat{u} \rangle \langle \widehat{u_t v_t} \rangle \right) \mathrm{d}l + \frac{1}{L_x} \int_{l_s} \frac{\langle \widehat{p} \rangle \langle \widehat{v} \rangle}{|\widehat{\mathbf{U}}|} \mathrm{d}l \\
& + \frac{1}{L_x Re_p} \int_{l_s} \frac{\partial |\widehat{\mathbf{U}}|}{\partial y} \mathrm{d}l - \frac{1}{L_x Re_p} \int_{x_s}^{x_a} \frac{\partial \langle \widehat{u} \rangle}{\partial y} \Big|_0 \mathrm{d}x \\
& - \frac{1}{L_x Re_p} \int_{x_b}^{x_r} \frac{\partial \langle \widehat{u} \rangle}{\partial y} \Big|_0 \mathrm{d}x,
\end{aligned}
\tag{F.14}
$$

where l_s indicates the whole dividing streamline, i.e $l_s = l_{su} \cup l_{sd}$. Equation (F.14) represents only half of the pressure drag as only the bottom wall is taken into account therefore

$$
\begin{aligned}
\widehat{C}_p = & \frac{2}{L_x} \int_{l_s} \frac{1}{|\widehat{\mathbf{U}}|} \left(\langle \widehat{v} \rangle \langle \widehat{u_t u_t} \rangle - \langle \widehat{u} \rangle \langle \widehat{u_t v_t} \rangle \right) \mathrm{d}l + \frac{2}{L_x} \int_{l_s} \frac{\langle \widehat{p} \rangle \langle \widehat{v} \rangle}{|\widehat{\mathbf{U}}|} \mathrm{d}l \\
& + \frac{2}{L_x Re_p} \int_{l_s} \frac{\partial |\widehat{\mathbf{U}}|}{\partial y} \mathrm{d}l - \frac{2}{L_x Re_p} \left(\int_{x_s}^{x_a} \frac{\partial \langle \widehat{u} \rangle}{\partial y} \Big|_0 \mathrm{d}x + \int_{x_b}^{x_r} \frac{\partial \langle \widehat{u} \rangle}{\partial y} \Big|_0 \mathrm{d}x \right).
\end{aligned}
\tag{F.15}
$$

F.2 Total drag

As the flow is periodic along x it is possible to consider as S_z the rectangular area between two bars depicted in fig. F.2 and apply (F.3) to get

$$\begin{aligned}\int_{x_b}^{x_a+L_x} \langle\widehat{uv}\rangle\Big|_h \mathrm{d}x = &\int_0^h (\langle\widehat{p}\rangle\Big|_{x_b} - \langle\widehat{p}\rangle\Big|_{x_a+L_x})\,\mathrm{d}y+\\ &-\int_0^h \frac{1}{Re_p}\frac{\partial\langle\widehat{u}\rangle}{\partial x}\Big|_{x_b}\mathrm{d}y - \int_{x_b}^{x_a+L_x}\frac{1}{Re_p}\frac{\partial\langle\widehat{u}\rangle}{\partial y}\Big|_0\mathrm{d}x+\\ &+\int_0^h \frac{1}{Re_p}\frac{\partial\langle\widehat{u}\rangle}{\partial x}\Big|_{x_a+L_x}\mathrm{d}y + \int_{x_b}^{x_a+L_x}\frac{1}{Re_p}\frac{\partial\langle\widehat{u}\rangle}{\partial y}\Big|_h\mathrm{d}x\end{aligned} \tag{F.16}$$

The terms in (F.16) involving $\frac{\partial\langle\widehat{u}\rangle}{\partial x}$ are null because of continuity $\frac{\partial\langle\widehat{u}\rangle}{\partial x} = -\frac{\partial\langle\widehat{v}\rangle}{\partial y}$ and no-slip condition therefore

$$\begin{aligned}\int_{x_b}^{x_a+L_x} \langle\widehat{uv}\rangle\Big|_h \mathrm{d}x = &\int_0^h (\langle\widehat{p}\rangle\Big|_{x_b} - \langle\widehat{p}\rangle\Big|_{x_a+L_x})\,\mathrm{d}y - \int_{x_b}^{x_a+L_x}\frac{1}{Re_p}\frac{\partial\langle\widehat{u}\rangle}{\partial y}\Big|_0\mathrm{d}x+\\ &+\int_{x_b}^{x_a+L_x}\frac{1}{Re_p}\frac{\partial\langle\widehat{u}\rangle}{\partial y}\Big|_h\mathrm{d}x\end{aligned} \tag{F.17}$$

By considering the time ensemble and z averaged pressure $\langle\widehat{p}\rangle = \left\langle\widehat{\phi}\right\rangle + \widehat{\Pi}_x x + 1/2\widehat{\Pi}_z L_z$ and that $\left\langle\widehat{\phi}\right\rangle$ is periodic along x with period L_x we obtain

$$\langle\widehat{p}\rangle\Big|_{x_b} - \langle\widehat{p}\rangle\Big|_{x_a+L_x} = \langle\widehat{p}\rangle\Big|_{x_b} - \langle\widehat{p}\rangle\Big|_{x_a} - \widehat{\Pi}_x L_x \tag{F.18}$$

The substitution (F.18) into (F.17) taking into account the Reynolds decomposition $\langle\widehat{uv}\rangle = \langle\widehat{u}\rangle\langle\widehat{v}\rangle + \langle\widehat{u_t v_t}\rangle$ gives

$$\begin{aligned}&\frac{1}{L_x}\int_0^h (\langle\widehat{p}\rangle\Big|_{x_a} - \langle\widehat{p}\rangle\Big|_{x_b})\,\mathrm{d}y + \frac{1}{L_x}\int_{x_b}^{x_a+L_x}\frac{1}{Re_p}\frac{\partial\langle\widehat{u}\rangle}{\partial y}\Big|_0\mathrm{d}x + \widehat{\Pi}_x h = -\frac{1}{L_x}\int_{x_b}^{x_a+L_x}\langle\widehat{u}\rangle\langle\widehat{v}\rangle\Big|_h\mathrm{d}x+\\ &-\frac{1}{L_x}\int_{x_b}^{x_a+L_x}\langle\widehat{u_t v_t}\rangle\Big|_h\mathrm{d}x + \frac{1}{L_x}\int_{x_b}^{x_a+L_x}\frac{1}{Re_p}\frac{\partial\langle\widehat{u}\rangle}{\partial y}\Big|_h\mathrm{d}x\end{aligned} \tag{F.19}$$

The first two terms of (F.19) are half of the ensemble time averaged coefficients $\widehat{C}_{pd}$ and $\widehat{C}_{ca}$ as we considered only the bottom surface of the channel therefore (F.19) reads

$$\begin{aligned}\frac{1}{2}(\widehat{C}_{pd} + \widehat{C}_{ca}) + \widehat{\Pi}_x h = &-\frac{1}{L_x}\int_{x_b}^{x_a+L_x}\langle\widehat{u}\rangle\langle\widehat{v}\rangle\Big|_h\mathrm{d}x - \frac{1}{L_x}\int_{x_b}^{x_a+L_x}\langle\widehat{u_t v_t}\rangle\Big|_h\mathrm{d}x\\ &+\frac{1}{L_x}\int_{x_b}^{x_a+L_x}\frac{1}{Re_p}\frac{\partial\langle\widehat{u}\rangle}{\partial y}\Big|_h\mathrm{d}x\end{aligned} \tag{F.20}$$

As in Gharib and Roshko (1987) the crest skin-friction is two order of magnitude lower that the total drag $-\widehat{\Pi}_x L_y = \widehat{C}_{pd} + \widehat{C}_{ca} + \widehat{C}_{cr} \approx \widehat{C}_{pd} + \widehat{C}_{ca}$. Hence (F.20) can be written as

$$- \widehat{\Pi}_x L_y \approx -\frac{L_y}{L_x}\int_{l_m} \langle \widehat{u} \rangle \langle \widehat{v} \rangle \,\mathrm{d}x - \frac{L_y}{L_x}\int_{l_m} \langle \widehat{u_t v_t} \rangle \,\mathrm{d}x + \frac{L_y}{L_x}\int_{l_m} \frac{1}{Re_p}\frac{\partial \langle \widehat{u} \rangle}{\partial y}\mathrm{d}x \qquad \text{(F.21)}$$

Equation (F.21) shows that the time ensemble average of the total drag $(-\widehat{\Pi}_x L_y)$ is due to the product $\langle \widehat{u} \rangle \langle \widehat{v} \rangle$, the Reynolds stress and the friction along the mouth of the cavity.

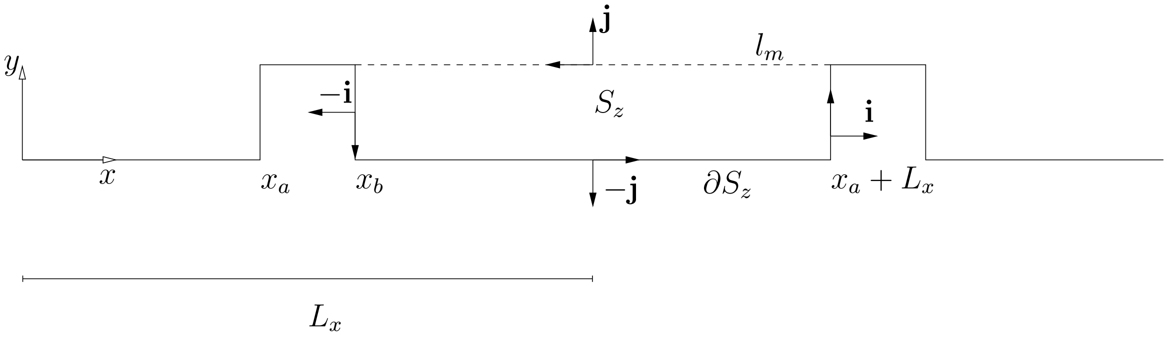

Figure F.2: Sketch of the rectangle S_z of boundary ∂S_z used for eq. F.16. The tangent and normal unit vectors to ∂S_z are depicted as arrows with full tip. Only the normal unit vector is indicated. The system of coordinate is plot at the left of the figure. x_a and x_b are the abscissas of the left and right vertical edge of the bar. The dashed line indicates the mouth of the cavity located at $y = h$. Only the bottom wall is shown.

Appendix G

Biharmonic equation

We consider the spanwise and time ensemble averaged continuity, streamwise and spanwise momentum equations

$$\frac{\partial \left\langle \widehat{u} \right\rangle}{\partial x} + \frac{\partial \left\langle \widehat{v} \right\rangle}{\partial y} = 0 \tag{G.1a}$$

$$\frac{\partial \left\langle \widehat{u} \right\rangle}{\partial \tau} = \frac{1}{Re_p} \left(\frac{\partial^2 \left\langle \widehat{u} \right\rangle}{\partial x^2} + \frac{\partial^2 \left\langle \widehat{u} \right\rangle}{\partial y^2} \right) - \left(\frac{\partial \left\langle \widehat{uu} \right\rangle}{\partial x} + \frac{\partial \left\langle \widehat{uv} \right\rangle}{\partial y} \right) - \frac{\partial \left\langle \widehat{p} \right\rangle}{\partial x} \tag{G.1b}$$

$$\frac{\partial \left\langle \widehat{v} \right\rangle}{\partial \tau} = \frac{1}{Re_p} \left(\frac{\partial^2 \left\langle \widehat{v} \right\rangle}{\partial x^2} + \frac{\partial^2 \left\langle \widehat{v} \right\rangle}{\partial y^2} \right) - \left(\frac{\partial \left\langle \widehat{uv} \right\rangle}{\partial x} + \frac{\partial \left\langle \widehat{vv} \right\rangle}{\partial y} \right) - \frac{\partial \left\langle \widehat{p} \right\rangle}{\partial y}. \tag{G.1c}$$

The left hand sides of equations (G.1b) and (G.1c) are null by assuming that pressure gradients and boundary conditions are steady. By introducing a streamfunction satisfying equation (G.1a)

$$\frac{\partial \psi}{\partial y} = \left\langle \widehat{u} \right\rangle, \qquad \frac{\partial \psi}{\partial x} = -\left\langle \widehat{v} \right\rangle, \tag{G.2}$$

and subtracting eq. (G.1b) differentiated on y by eq. (G.1c) differentiated on x we obtain

$$\nabla^4 \psi = Re_p \left(\frac{\partial \psi}{\partial y} \frac{\partial \nabla^2 \psi}{\partial x} - \frac{\partial \psi}{\partial x} \frac{\partial \nabla^2 \psi}{\partial y} \right) \tag{G.3}$$

where ∇^2 and $\nabla^4 = \nabla^2 \nabla^2$ are the Laplace and biharmonic operators respectively. The boundary conditions for (G.3) are

$$\psi\left(0, y\right) = \psi\left(h, y\right) = 0, \qquad 0 \le y \le h, \tag{G.4a}$$

$$\psi\left(x, h\right) = 0, \qquad 0 \le x \le h, \tag{G.4b}$$

$$\psi\left(x,0\right)=0, \qquad h\leq x\leq L_x, \tag{G.4c}$$

$$\frac{\partial\psi}{\partial x}\left(0,y\right)=\frac{\partial\psi}{\partial x}\left(h,y\right)=0, \qquad 0\leq y\leq h, \tag{G.4d}$$

$$\frac{\partial\psi}{\partial y}\left(x,h\right)=0, \qquad 0\leq x\leq h, \tag{G.4e}$$

$$\frac{\partial\psi}{\partial y}\left(x,0\right)=0, \qquad h\leq x\leq L_x, \tag{G.4f}$$

$$\frac{\partial\left\langle\widehat{u}\right\rangle}{\partial y}\left(x,1+h\right)=\frac{\partial^2\psi}{\partial y^2}\left(x,1+h\right)=0, \qquad 0\leq x\leq L_x, \tag{G.4g}$$

$$\psi\left(0,y\right)=\psi\left(L_x,y\right), \qquad \frac{\partial\psi}{\partial x}\left(0,y\right)=\frac{\partial\psi}{\partial x}\left(L_x,y\right), \qquad 0\leq y\leq 1+h, \tag{G.4h}$$

$$\psi\left(1+h\right)=1. \tag{G.4i}$$

Conditions (G.4a)-(G.4c) indicate that ψ is constant and set to zero at the wall as $\mathrm{d}\psi=\partial\psi/\partial x\,\mathrm{d}x+\partial\psi/\partial y\,\mathrm{d}y=-\left\langle\widehat{v}\right\rangle\mathrm{d}x+\left\langle\widehat{u}\right\rangle\mathrm{d}y=0$. Equations (G.4d)-(G.4f) give a null value to the component of velocity normal to the wall. The symmetry of the velocity $\left\langle\widehat{u}\right\rangle$ about the midline ($y=1+h$) is imposed via (G.4g) while periodicity along x is enforced via (G.4h). The streamfunction value at centerline (equation (G.4i)) is obtained by requiring that the mass flow rate is $\dot{m}=1$, namely

$$\psi\left(1+h\right)=\int_h^{1+h}u\left(y\right)\mathrm{d}y=1. \tag{G.5}$$

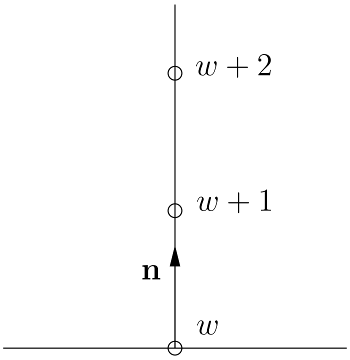

Figure G.1: Right: Sketch of the normal direction to the surface. **n** is the normal unit vector, subscripts w, $w+1$ and $w+2$ stem for the point at wall, the first and second point along the normal direction respectively.

Numerical procedure for the biharmonic equation

An attempt to solve the biharmonic equation (G.3) by discretizing the ∇^4 operator via a thirteen points stencil formula (Bjorstad, 1980) has been made. The resulting iterative method diverged despite the use of small under-relaxation factors and even for the 'creeping' flow case for which Re_p and the advective terms vanish.

We employed a procedure used by previous authors (Pan and Acrivos, 1967; Burggraf, 1966; Kawaguti, 1961) which splits eq. (G.3) into two equations for ψ and ω. The vorticity vector has only one non-zero component $\omega = \frac{\partial \langle \widehat{v} \rangle}{\partial x} - \frac{\partial \langle \widehat{u} \rangle}{\partial y}$ which can be written as $\omega = -\nabla^2 \psi$, therefore we solve the system

$$\begin{cases} \nabla^2 \omega = Re_p \left(\frac{\partial \psi}{\partial y} \frac{\partial \omega}{\partial x} - \frac{\partial \psi}{\partial x} \frac{\partial \omega}{\partial y} \right) \\ \nabla^2 \psi = -\omega. \end{cases} \tag{G.6}$$

The system (G.6) is discretized via centered finite differences

$$\left. \frac{\partial^2 \psi}{\partial x^2} \right|_{a,b} \approx \frac{\Psi_{a+1,b} - 2\Psi_{a,b} + \Psi_{a-1,b}}{\Delta x^2}, \qquad \left. \frac{\partial^2 \psi}{\partial y^2} \right|_{a,b} \approx \frac{\Psi_{a,b+1} - 2\Psi_{a,b} + \Psi_{a,b-1}}{\Delta y^2}, \tag{G.7a}$$

$$\left. \frac{\partial \psi}{\partial x} \right|_{a,b} \approx \frac{\Psi_{a+1,b} - \Psi_{a-1,b}}{2\Delta x}, \qquad \left. \frac{\partial \psi}{\partial y} \right|_{a,b} \approx \frac{\Psi_{a,b+1} - \Psi_{a,b-1}}{2\Delta y}, \tag{G.7b}$$

that give the approximation

$$\begin{aligned} & L\left[\omega_{a+1,b} + \omega_{a-1,b}\right] + M\left[\omega_{a,b+1} + \omega_{a,b-1}\right] + P\left(\psi_{a+1,b} - \psi_{a-1,b}\right)\left(\omega_{a,b+1} - \omega_{a,b-1}\right) + \\ & - P\left(\psi_{a,b+1} - \psi_{a,b-1}\right)\left(\omega_{a+1,b} - \omega_{a-1,b}\right) = \omega_{a,b}, \end{aligned} \tag{G.8a}$$

$$L\left[\psi_{a+1,b} + \psi_{a-1,b}\right] + M\left[\psi_{a,b+1} + \psi_{a,b-1}\right] + N\omega_{a,b} = \psi_{a,b}, \tag{G.8b}$$

where

$$\begin{aligned} L &= \frac{\frac{1}{\Delta x^2}}{2\left(\frac{1}{\Delta x^2} + \frac{1}{\Delta y^2}\right)}, \quad & M &= \frac{\frac{1}{\Delta y^2}}{2\left(\frac{1}{\Delta x^2} + \frac{1}{\Delta y^2}\right)}, \\ N &= L\Delta x^2, & P &= \frac{\frac{Re_p}{4\Delta x \Delta y}}{2\left(\frac{1}{\Delta x^2} + \frac{1}{\Delta y^2}\right)}. \end{aligned} \tag{G.9}$$

These two equations are solved iteratively via a method suggested by Burggraf (1966). First the residuals

$$r^{\omega}_{a,b} = L\left[\omega_{a+1,b} + \omega_{a-1,b}\right] + M\left[\omega_{a,b+1} + \omega_{a,b-1}\right] + P\left(\psi_{a+1,b} - \psi_{a-1,b}\right)\left(\omega_{a,b+1} - \omega_{a,b-1}\right) + \\ - P\left(\psi_{a,b+1} - \psi_{a,b-1}\right)\left(\omega_{a+1,b} - \omega_{a-1,b}\right) - \omega_{a,b}, \tag{G.10a}$$

$$r^{\psi}_{a,b} = L\left[\psi_{a+1,b} + \Psi_{a-1,b}\right] + M\left[\psi_{a,b+1} + \psi_{a,b-1}\right] + N\omega_{a,b} - \psi_{a,b} \tag{G.10b}$$

are defined, then the updated values of ω and ψ are obtained by using

$$\omega^{new}_{a,b} = \omega_{a,b} + \alpha\, r^{\omega}_{a,b}, \qquad \psi^{new}_{a,b} = \psi_{a,b} + \alpha\, r^{\psi}_{a,b}. \tag{G.11}$$

The parameter α controls the convergence of the algorithm: α should be in the range $1 < \alpha \leq 2$ for stable iterations in order to increase the convergence rate otherwise α should be in $0 < \alpha < 1$ to increase the numerical stability. The values of $\omega_{a,b}$ and $\psi_{a,b}$ are used as soon as they are available. The vorticity $\omega^{new}_{a,b}$ and $\psi^{new}_{a,b}$ are calculated considering points ordered along horizontal rows and then moving to the next row until the the top boundary has been reached. In equation (G.11) first $\omega^{new}_{a,b}$ is computed all over the domain and then the iteration of $\psi^{new}_{a,b}$ can begin. The initial values of ψ and ω should be chosen with common sense for high Re_p as, in this case, the problem is strongly nonlinear and a bad first guess could not guarantee the stability of the algorithm even for low values of α. We found out that using the solution of the problem with a lower Re_p furnished an acceptable first attempt to obtain a converged solution. The algorithm convergence is checked by monitoring the residual norms $\left\|r^{\Omega}_{a,b}\right\| = \sqrt{\sum_{a=1}^{n_x-1}\sum_{b=1}^{n_y} r^{\omega}_{a,b}\, r^{\omega}_{a,b}}$ and $\left\|r^{\Psi}_{a,b}\right\| = \sqrt{\sum_{a=1}^{n_x-1}\sum_{b=1}^{n_y} r^{\psi}_{a,b}\, r^{\psi}_{a,b}}$ at each iteration.

Vorticity-streamfunction boundary conditions

The boundary conditions are (refer to fig. 4.1 in chapter 4)

$$\psi_{1,b} = \psi_{l,b} = 0, \qquad 1 \leq b \leq m, \tag{G.12a}$$

$$\psi_{a,m} = 0, \qquad 1 \leq a \leq l, \tag{G.12b}$$

$$\psi_{a,1} = 0, \qquad l \leq a \leq n_x, \tag{G.12c}$$

$$\psi_{a,n_y} = 1, \qquad 1 \leq a \leq n_x, \tag{G.12d}$$

$$\begin{aligned} &\psi_{nx,b} = \Psi_{1,b}, \quad \psi_{0,b} = \psi_{n_x-1,b}, \quad \omega_{nx,b} = \omega_{1,b}, \\ &\omega_{0,b} = \omega_{n_x-1,b}, \qquad 1 \leq b \leq n_y, \end{aligned} \tag{G.12e}$$

$$\psi_{a,b} = 0, \quad 2 \leq a \leq l-1, \quad 2 \leq b \leq m-1, \tag{G.12f}$$

$$\omega_{a,ny} = 0, \qquad 1 \leq a \leq n_x. \tag{G.12g}$$

Conditions (G.12a)-(G.12c) indicate the streamfunction value at wall, condition (G.12d) specifies ψ at the channel centerline, periodicity along x is expressed via (G.12e), equation (G.12e) set $\psi = 0$ inside the bar. Condition (G.12g) gives a zero value to the vorticity at the centerline because $\frac{\partial^2 \psi}{\partial y^2}(x, 1+h) = 0$, $\psi(1+h) = 1$ and from (G.6) we have that $\omega(x, 1+h) = -\nabla^2 \psi(x, 1+h) = 0$.

The system (G.3) needs two boundary conditions on the value of ψ and its normal gradient at solid walls but no conditions on vorticity are specified. We adopt the interior constraint method (Huang and Seymour, 1995) which does not require any wall vorticity condition and it is suitable to solve our problem because of the vorticity singularities at corners (Gupta et al., 1981; Moffatt, 1964). By considering the unit vector normal to the wall (refer to fig. G.1) we obtain the two boundary conditions

$$\psi_w = 0, \qquad \left[\frac{\partial \psi}{\partial \mathbf{n}}\right]_w \approx \frac{-3\psi_w + 4\Psi_{w+1} - \psi_{w+2}}{2\Delta n} = 0, \tag{G.13}$$

where a second order forward finite difference is used to approximate the normal gradient of the streamfunction to the wall. By combining the previous two equations we obtain the two conditions for points w and $w+1$

$$\psi_w = 0 \qquad \psi_{w+1} = \frac{1}{4}\psi_{w+2}. \tag{G.14}$$

Each point in the computational domain (included boundary points) needs two equations for generating a solvable system: for all interior points we have one equation for ψ and one for ω except for points $w+1$ for which we have condition (G.14) and $\omega_{w+1} = -\nabla^2 \psi\Big|_{w+1}$. This makes the system complete without the need for a vorticity condition as the unknown wall vorticity ω_w appears only if $\nabla^2 \omega = Re_p \left(\frac{\partial \psi}{\partial y}\frac{\partial \omega}{\partial x} - \frac{\partial \psi}{\partial x}\frac{\partial \omega}{\partial y}\right)$ is discretized at points $w+1$.

The following conditions are therefore employed

$$\psi_{a,2} = \frac{1}{4}\psi_{a,3}, \qquad l+2 \leq a < n_x - 1, \tag{G.15a}$$

$$\psi_{l+1,b} = \frac{1}{4}\psi_{l+2,b}, \qquad \psi_{nx-1,b} = \frac{1}{4}\psi_{nx-2,b}, \qquad 3 \leq b \leq m, \tag{G.15b}$$

$$\Psi_{a,m+1} = \frac{1}{4}\psi_{a,m+2}, \qquad 1 \leq a \leq l, \tag{G.15c}$$

ψ value at point $(l+1,2)$ is set to zero because it is not clear if using $\Psi_{l+1,2} = \frac{1}{4}\Psi_{l+2,2}$ or $\Psi_{l+1,2} = \frac{1}{4}\Psi_{l+1,3}$ and the same applies for point $(n_x - 1, 2)$: this is equivalent to use the forward first order scheme $\left[\frac{\partial \psi}{\partial \mathbf{n}}\right]_w \approx \frac{\psi_{w+1} - \psi_w}{\Delta n} = 0$.

A null value is given to wall vorticity and inside the bar only for convenience as it does not take part in the algorithm

$$\omega_{a,1} = 0, \quad l+1 \leq a \leq n_x, \tag{G.16a}$$

$$\omega_{a,b} = 0, \quad 1 \leq a \leq l \quad 1 \leq b \leq m. \tag{G.16b}$$

Numerical results

Fig. G.3 shows the streamlines for the Stokes flow ($Re_p = 0$) from the experiment of Taneda (1979) and the numerical result obtained by solving the system (G.3) in order to validate the developed code. The streamlines tend to be horizontal moving upward toward the centerline of the channel located at $y = 1+h$ and show two vortices near the edges of the bar. We tried to compute the solution of the system (G.3) at $Re_p = 4200$ using as the solution of the problem at a lower Reynolds number as initial guess for the SOR method. We have been able to solve only the problem up to a to $Re_p = 300$ because code diverges for higher Re_p the despite the usage of a very small under-relaxation factor.

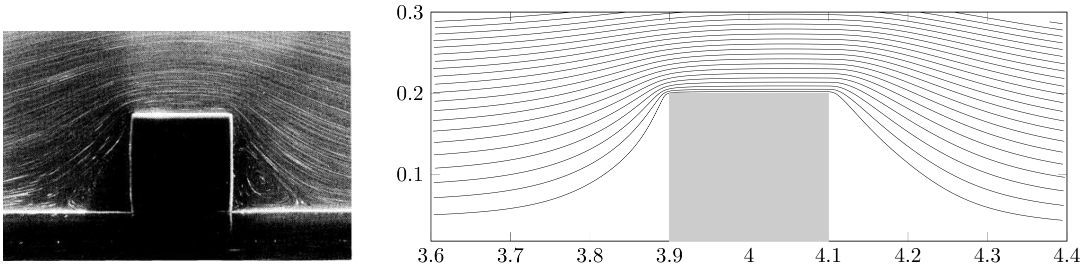

Figure G.2: Left: Stokes flow around a square bar. Adapted from Taneda (1979). Right: Streamlines obtained by solving the system (G.3). Only the streamlines near the bar are shown.

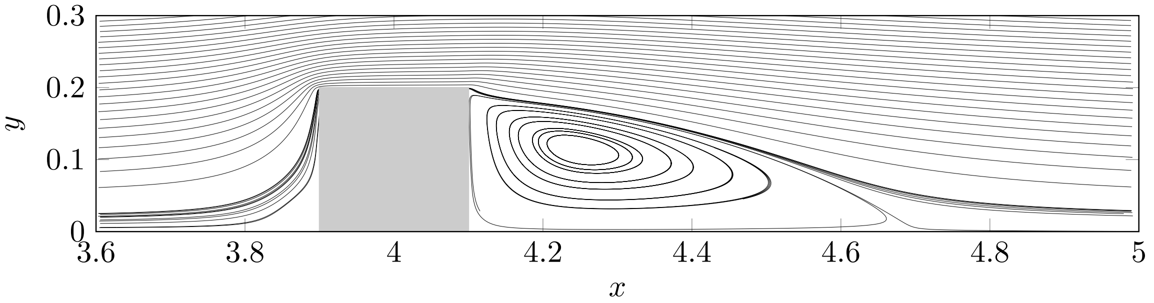

Figure G.3: Left: Streamlines obtained by solving the system (G.3) for $Re_p = 300$. Only the streamlines near the bar are shown.

European Drag Reduction and Flow Control Meeting – EDRFCM 2019
March 26–29 2019, Bad Herrenalb, Germany

SEPARATION DRAG REDUCTION IN A ROUGH CHANNEL VIA A SPANWISE OSCILLATING PRESSURE GRADIENT

Gianluca Pironti & Vinh-Tan Nguyen
Institute of High Performance Computing, 1 Fusionopolis Way, Singapore

Pierre Ricco
Department of Mechanical Engineering, The University of Sheffield, Sheffield, UK

INTRODUCTION

In this work we study the effect of a spanwise oscillating pressure gradient $\Pi_z\,(t) = A\,\cos\,(2\pi\,t/T)$ on the pressure drag induced by large scale separation behind square bars aligned along the spanwise direction, as shown in fig. 1. This technique takes inspiration from the method of spanwise wall oscillation employed widely to reduce turbulent friction drag [2, 4]. To the best of our knowledge, this is the first time that large scale spanwise forcing has been utilized to control a separated flow. The main novelty of this approach is the possibility to decrease the form drag without the introduction of an undesired friction drag penalty which is a common feature shared by traditional separation control techniques, such as vortex generators [1]. We also observe the further beneficial outcome of reduction of skin-friction drag.

NUMERICAL PROCEDURES

We simulate the flow by means of the DNS code Incompact3d [3] using an immersed boundary method to model the square bars. We use periodic boundary conditions along the streamwise (x) and the spanwise (z) directions while the no-slip condition is enforced over the solid walls. All the variables are scaled by the distance δ^* defined in fig. 1 and the centerline velocity U_p^* of a Poiseuille flow with the same mass flow rate. The Reynolds number is $Re_p = U_p^*\,\delta^*/\nu^* = 4200$.

The computational box has dimensions $L_x = 8$, $L_y = 2.4$, $L_z = \pi$. The grid is homogeneous along x and z and stretched along y with a total of $1600 \times 241 \times 192$ points. Ten bars of square section and height $h = 0.2$ are located over the two channel walls at $y = 0$ and $y = L_y = 2\,(1+h)$. The simulations are performed at constant mass flow rate. The non-dimensional amplitude and period of the oscillation for the controlled flow are $A = A^*\,\delta^*/\left(\rho^* U_p^{*2}\right) = 0.71$ and $T = T^* U_p^*/\delta^* = 7.1$.

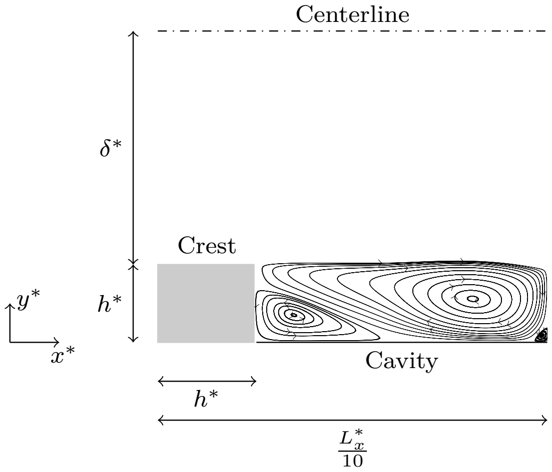

Figure 1: Sketch of the channel configuration. Only one bar (grey rectangle) is depicted. The coordinate x indicates the streamwise direction. The channel is symmetric about the centerline (dashdotted line).

PERFORMANCE PARAMETERS

For a separated flow the drag is composed of a form drag and a skin-friction drag. In our case, the form drag is due to the difference of the integrals of pressure along the vertical sides of the bars, while the friction drag is computed by integrating the viscous stress on the horizontal surfaces, i.e. over the crests and the cavities, shown in fig. 1. For each component of the drag we define a percentage reduction. For example the total drag percentage reduction $\mathcal{R}(\%)$ is defined as:

$$\mathcal{R}(\%) = 100\left(1 - \frac{C_{f_o} + C_{pd_o}}{C_f + C_{pd}}\right), \tag{1}$$

where C_f and C_{pd} are the friction and pressure drag coefficient for the flow without control and the subscript o indicates values when Π_z is activated. As we deal with an active technique, power $\mathcal{P}(\%)$ is supplied to the fluid:

$$\mathcal{P}(\%) = \frac{100}{\Pi_x U_b}\,\frac{1}{t_f - t_i}\int_{t_i}^{t_f} \Pi_z(t)\;W_b(t)\;\mathrm{d}t, \tag{2}$$

where t_i and t_f are the initial and final times used for time averaging, Π_x is the mean pressure gradient driving the flow along x in the uncontrolled case, U_b is the constant streamwise bulk velocity: $W_b(t)$ is the spanwise bulk velocity due to the control and defined as $W_b = 1/V_F\,\int_{V_F} W(x,y,L_z,t)\,\mathrm{d}x\,\mathrm{d}y\,\mathrm{d}z$

where V_F is the fluid volume and $W(x,y,L_z,t)$ the spanwise velocity at $z = L_z$ created by the application of the spanwise oscillating pressure gradient. The balance between the control power supplied to the system and the power saved (equal to $\mathcal{R}(\%)$) reads:

$$\mathcal{P}_{net}(\%) = \mathcal{R}(\%) - \mathcal{P}(\%). \qquad (3)$$

RESULTS AND DISCUSSION

The pressure and friction drag coefficients for the flow without control are $C_{pd} = P_d^* / \left(\rho^* U_p^{*2} L_x^* L_z^*\right) = 6.45 \times 10^{-3}$ and $C_f = F^* / \left(\rho^* U_p^{*2} L_x^* L_z^*\right) = 5.26 \times 10^{-4}$ with P_d^* and F^* pressure and friction drag. The friction drag coefficient on the crest is $C_{cr} = 1.18 \times 10^{-3}$ while that on the cavity is $C_{ca} = -6.60 \times 10^{-4}$. We define an effective velocity $u_e = \sqrt{C_{pd} + C_f} = 8.35 \times 10^{-2}$ and a Reynolds number $Re_e = u_e^* \, \delta^* / \nu^* \approx 351$ that give $A^+ = A / \left(Re_e \, u_e^2\right) = 2.89 \times 10^{-4}$ and $T^+ = T \, u_e \, Re_e \approx 208$ in wall units.

Fig. 2 and 3 depict the pressure drag and friction coefficients as a function of t: after a transient all curves oscillate periodically due to the control.

Tab. 1 presents the percentage variations of all the drag components: all the drag components decrease because of the action of the control except for the friction drag at the cavity. Friction drag at the crest is positive because the flow is attached to the surface while inside the cavity the flow separates with a negative and positive friction coefficient. The total friction (crest and cavity contributions together) decreases thanks to the spanwise oscillating pressure gradient hence both pressure and friction drag reduction occur.

We also find that $\mathcal{P}(\%) = 129.8\%$: control power overcomes the benefit of a reduced drag and $\mathcal{P}_{net}(\%) = -123.5\%$.

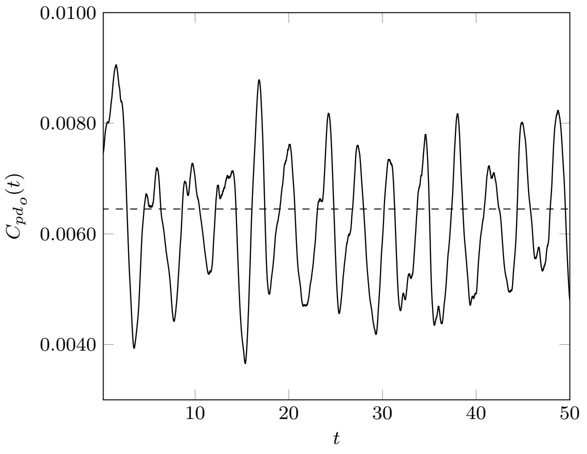

Figure 2: Pressure drag coefficient $C_{pd_o}(t)$ history since the activation of the control. The dashed line indicates the time averaged value C_{pd} of the base flow.

$\mathcal{R}C_{pd}(\%)$	$\mathcal{R}C_{ca}(\%)$	$\mathcal{R}C_{cr}(\%)$	$\mathcal{R}C_f(\%)$	$\mathcal{R}(\%)$
6.3%	−6.9%	6.7%	7.6%	6.4%

Table 1: Percentage variations of C_{pd}, C_{ca}, C_{cr}, C_f, $C_{pd}+C_f$ after the control is activated. Positive values indicate drag reduction, negative stem for drag increase. The values are obtained using the equation $\mathcal{R}Q(\%) = 100\,(1 - Q_o/Q)$. Where Q is any of C_{pd}, C_{ca}, C_{cr}, C_f, $C_{pd} + C_f$ and Q_o the value after the control is turned on.

CONCLUSIONS

A drag reduction study on a rough channel has been conducted: we proved that it is possible to decrease both pressure and friction drag. The power to control the flow has been quantified and compared with drag reduction showing no net saving of energy for the chosen amplitude and period. Further studies are necessary to determine if some combinations of parameters that reduce drag and minimize the control power do exist.

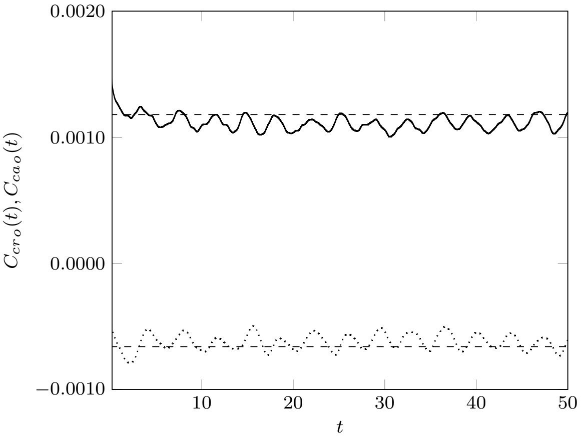

Figure 3: Friction coefficient at the crest of the bar $C_{cr_o}(t)$ (solid) and at the bottom of the cavity $C_{ca_o}(t)$ (dotted) as a function of time. The dashed line stem for the time averaged values of the uncontrolled flow C_{cr} and C_{ca}.

ACKNOWLEDGEMENTS

We would like to thank the Department of Mechanical Engineering at the University of Sheffield and the Agency for Science, Technology and Research (A*STAR) of Singapore for funding this research. We would like to express gratitude towards the A*STAR Computational Resource Centre for their kind assistance with providing high performance computing resource for the current work.

REFERENCES

[1] G. Godard and M. Stanislas. Control of a decelerating boundary layer. part 1: Optimization of passive vortex generators. *Aerospace Science and Technology*, 10(3):181–191, 2006.

[2] W.J. Jung, N. Mangiavacchi, and R. Akhavan. Suppression of turbulence in wall-bounded flows by high-frequency spanwise oscillations. *Physics of Fluids A: Fluid Dynamics*, 4(8):1605–1607, 1992.

[3] S. Laizet and E. Lamballais. High-order compact schemes for incompressible flows: A simple and efficient method with quasi-spectral accuracy. *Journal of Computational Physics*, 228(16):5989–6015, 2009.

[4] M. Quadrio and P. Ricco. Critical assessment of turbulent drag reduction through spanwise wall oscillations. *Journal of Fluid Mechanics*, 521:251–271, 2004.

Bibliography

M. Amitay and A. Glezer. Aerodynamic flow control using synthetic jet actuators. *Control of Fluid Flow*, pages 45–73, 2006.

J. Banchetti, P. Luchini, and M. Quadrio. Turbulent drag reduction over curved walls. *J. Fluid Mech.*, 896, 2020.

A. Baron and M. Quadrio. Turbulent drag reduction by spanwise wall oscillations. *Appl. Sc. Res.*, 55:311–326, 1996.

G.K. Batchelor. A proposal concerning laminar wakes behind bluff bodies at large reynolds number. *J. Fluid Mech.*, 1(4):388–398, 1956.

D.W. Bechert and M. Bertenwerfer. The viscous flow on surfaces with longitudinal ribs. *J. Fluid Mech.*, 206:105–209, 1989.

D.W. Bechert, M. Bruse, W. Hage, J.G.T. Van der Hoeven, and G. Hoppe. Experiments on drag-reducing surfaces and their optimization with an adjustable geometry. *J. Fluid Mech.*, 338:59–87, 1997.

P. E. Bjorstad. Numerical solution of the biharmonic equation. Technical report, Stanford univ ca dept of computer science, 1980.

R. Bradley and W. Wray. A conceptual study of leading-edge-vortex enhancement by blowing. *J. Aircraft*, 11(1):34–38, 1974.

M.B. Bragg and G.M. Gregorek. Experimental study of airfoil performance with vortex generators. *J. Aircraft*, 24(5):305–309, 1987.

M. Breuer, N. Peller, C. Rapp, and M. Manhart. Flow over periodic hills–numerical and experimental study in a wide range of reynolds numbers. *Comp. Fluids*, 38(2): 433–457, 2009.

P. Burda, J. Novotny, and J. Vsistek. Analytical solution of stokes flow near corners and applications to numerical solution of navier-stokes equations with high precision. *Appl. Math.*, pages 43–54, 2012.

O. R. Burggraf. Analytical and numerical studies of the structure of steady separated flows. *JFM*, 24(1):113–151, 1966.

W. Calarese and W.P. Crisler. Aim-85-0354 afterbody drag reduction by vortex generators. 1985.

P.K. Chang. *Separation of flow*. Elsevier, 2014.

T.L. Chng, A. Rachman, H.M. Tsai, and G. Zha. Flow control of an airfoil via injection and suction. *J. Aircraft*, 46(1):291–300, 2009.

H. Choi, P. Moin, and J. Kim. Direct numerical simulation of turbulent flow over riblets. *J. Fluid Mech.*, 255:503–539, 1993.

J-I. Choi, C-X. Xu, and H. J. Sung. Drag reduction by spanwise wall oscillation in wall-bounded turbulent flows. *AIAA J.*, 40(5):842–850, 2002.

K.-S. Choi. Near-wall structure of a turbulent boundary layer with riblets. *J. Fluid Mech.*, 208:417–458, 1989.

K-S. Choi and M. Graham. Drag reduction of turbulent pipe flows by circular-wall oscillation. *Phys. Fluids*, 10(1):7–9, 1998.

K.S. Choi, G.E. Gadd, H.H. Pearcey, A.M. Savill, and S. Svensson. Tests of drag-reducing polymer coated on a riblet surface. *Appl. Sc. Res.*, 46(3):209–216, 1989.

A.J. Chorin. Numerical solution of the Navier-Stokes equations. *Math. comput.*, 22 (104):745–762, 1968.

S. Chun, I. Lee, and H. J. Sung. Effect of spanwise-varying local forcing on turbulent separated flow over a backward-facing step. *Experiments in Fluids*, 26(5):437–440, 1999.

T. C. Corke, E. J. Jumper, M. L Post, D. Orlov, and T. E. McLaughlin. Application of weakly-ionized plasmas as wing flow-control devices. *AIAA paper*, 350:2002, 2002.

M. O. Deville, P. F. Fischer, E.H. Mund, et al. *High-order methods for incompressible fluid flow*, volume 9. Cambridge university press, 2002.

Y. Du, V. Symeonidis, and G.E. Karniadakis. Drag reduction in wall-bounded turbulence via a transverse travelling wave. *J. Fluid Mech.*, 457:1–4, 2002.

M. Gad-el Hak, A. Pollard, and J.P. Bonnet. *Flow control: fundamentals and practices.* Springer, 1998.

R. Gautier, S. Laizet, and E. Lamballais. A dns study of jet control with microjets using an immersed boundary method. *Int. J. Comp. Fluid Dyn.*, 28(6-10):393–410, 2014.

M Gharib and A Roshko. The effect of flow oscillations on cavity drag. *JFM*, 177: 501–530, 1987.

D. Goldstein, R. Handler, and L. Sirovich. Modeling a no-slip flow boundary with an external force field. *J. Comp. Phys.*, 105(2):354–366, 1993.

D. Greenblatt, K.B. Paschal, C.S. Yao, J. Harris, N.W. Schaeffler, and A. E. Washburn. Experimental investigation of separation control. Part 1: Baseline and steady suction. *AIAA J.*, 44(12):2820–2830, 2006.

R. Grüneberger, F. Kramer, E. Wassen, W. Hage, R. Meyer, and F. Thiele. Influence of wave-like riblets on turbulent friction drag. In *Nature-Inspired Fluid Mechanics*, pages 311–329. Springer, 2012.

M. M. Gupta, R. P. Manohar, and B. Noble. Nature of viscous flows near sharp corners. *Computers & Fluids*, 9(4):379–388, 1981.

W. Hage, D.W. Bechert, and M. Bruse. Artificial shark skin on its way to technical application. In *Science and Art Symposium 2000*, pages 169–175. Springer, 2000.

W. Hage, D.W. Bechert, and M. Bruse. Yaw angle effects on optimized riblets. In *Aerodynamic Drag Reduction Technologies*, pages 278–285. Springer, 2001.

J.O. Hinze. *Turbulence.* McGraw Hill, Inc. – Second Edition, 1975.

A. Hooshmand, R. Youngs, J.M. Wallace, and J.L. Balint. An experimental study of changes in the structure of a turbulent boundary layer due to surface geometry changes. *AIAA Paper*, pages 83–0230, 1983.

H. Huang and B. R. Seymour. A finite difference method for flow in a constricted channel. *Computers & fluids*, 24(2):153–160, 1995.

J. Huang, T. C. Corke, and F. O. Thomas. Plasma actuators for separation control of low-pressure turbine blades. *AIAA J.*, 44(1):51–57, 2006.

T.N. Jukes and K.S. Choi. Dielectric-barrier-discharge vortex generators: characterisation and optimisation for flow separation control. *Exp. Fluids*, 52(2):329–345, 2012.

W.J. Jung, N. Mangiavacchi, and R. Akhavan. Suppression of turbulence in wall-bounded flows by high-frequency spanwise oscillations. *Phys. Fluids A*, 4(8):1605–1607, 1992.

M. Kawaguti. Numerical solution of the navier-stokes equations for the flow in a two-dimensional cavity. *J. Phys. Soc. Japan*, 16(11):2307–2315, 1961.

L. Keefe. A normal vorticity actuator for near-wall modification of turbulent shear flows. *AIAA Paper*, 97-0547, 1997.

J. Kim and P. Moin. Application of a fractional-step method to incompressible Navier-Stokes equations. *J. Comp. Phys.*, 59:308–323, 1985.

J. Kim, P. Moin, and R. Moser. Turbulence statistics in fully developed channel flow at low Reynolds number. *J. Fluid Mech.*, 177:133–166, 1987.

S. Laizet and E. Lamballais. High-order compact schemes for incompressible flows: A simple and efficient method with quasi-spectral accuracy. *J. Comp. Phys.*, 228: 5989–6015, 2009.

E. Lamballais and J.H. Silvestrini. Direct numerical simulation of interactions between a mixing layer and a wake around a cylinder.

M. Lee and R.D. Moser. Direct numerical simulation of turbulent channel flow up to $\mathrm{Re}_\tau \approx 5200$. *J. Fluid Mech.*, 774:395–415, 2015.

S.K. Lele. Compact finite difference schemes with spectral-like resolution. *J. Comp. Phys.*, 103:16–42, 1992.

S. Leonardi, P. Orlandi, R.J. Smalley, L. Djenidi, and R.A. Antonia. Direct numerical simulations of turbulent channel flow with transverse square bars on one wall. *J. Fluid Mech.*, 491:229–238, 2003.

J.C. Lin, G.V. Selby, and F.G. Howard. Exploratory study of vortex-generating devices for turbulent flow separation control. *AIAA paper*, 42, 1991.

J.C. Lin, S.K. Robinson, R.J. McGhee, and W.O. Valarezo. Separation control on high-lift airfoils via micro-vortex generators. *J. Aircraft*, 31(6):1317–1323, 1994.

P. Luchini, F. Manzo, and A. Pozzi. Resistance of a grooved surface to parallel flow and cross-flow. *J. Fluid Mech.*, 228:87–109, 1991.

Y. Maday, A. T. Patera, and E. M. Rønquist. An operator-integration-factor splitting method for time-dependent problems: application to incompressible fluid flow. *J. Sci. Comp.*, 5(4):263–292, 1990.

N.N. Mansour, J. Kim, and P. Moin. Reynolds-stress and dissipation-rate budgets in a turbulent channel flow. *J. Fluid Mech.*, 194:15–44, 1988.

J. Meyer and A. Seginer. Effects of periodic spanwise blowing on delta-wing configuration characteristics. *AIAA J.*, 32(4), 1994.

R. Mittal and G. Iaccarino. Immersed boundary methods. *Annu. Rev. Fluid Mech.*, 37:239–261, 2005.

H. K. Moffatt. Viscous and resistive eddies near a sharp corner. *JFM*, 18(1):1–18, 1964.

J. Mohd-Yusof. Combined immersed boundaries/b-splines method for simulations of flows in complex geometries. *CTR Ann. Res. Briefs*, 1997.

R. Moser, J. Kim, and N.N. Mansour. Direct numerical simulation of turbulent channel flow up to $Re_\theta = 590$. *Phys. Fluids*, 11(4):943–945, 1999.

G. Neretti. Active flow control by using plasma actuators. *Recent Progress in Some Aircraft Technologies*, pages 57–76, 2016.

R.J. Nuber and J.R. Needham. Exploratory wind-tunnel investigation of the effectiveness of area suction in eliminating leading-edge separation over an NACA 641A212 airfoil. 1948.

P. Orlandi. *Fluid flow phenomena: a numerical toolkit*, volume 55. Springer Science & Business Media, 2012.

P. Orlandi and M. Fatica. Direct simulations of turbulent flow in a pipe rotating about its axis. *J. Fluid Mech.*, 343:43–72, 1997.

F. Pan and A. Acrivos. Steady flows in rectangular cavities. *JFM*, 28(4):643–655, 1967.

P. Parnaudeau, E. Lamballais, D. Heitz, and J.H. Silvestrini. Combination of the immersed boundary method with compact schemes for dns of flows in complex geometry. In *Direct and Large-Eddy Simulation V*, pages 581–590. Springer, 2004.

Y. Peet, P. Sagaut, and Y. Charron. Turbulent drag reduction using sinusoidal riblets with triangular cross-section. *AIAA Paper*, 2008-3745, 2008.

C. S. Peskin. Flow patterns around heart valves: a numerical method. *J. Comp. Phys.*, 10(2):252–271, 1972.

S.B. Pope. *Turbulent Flows.* Cambridge University Press, 2000.

M.L. Post and T.C. Corke. Separation control on high angle of attack airfoil using plasma actuators. *AIAA J.*, 42(11), 2004.

M.L. Post and T.C. Corke. Separation control using plasma actuators: dynamic stall vortex control on oscillating airfoil. *AIAA J.*, 44(12):3125–3135, 2006.

M. Quadrio and P. Ricco. Critical assessment of turbulent drag reduction through spanwise wall oscillations. *J. Fluid Mech.*, 521:251–271, 2004.

M. Quadrio and P. Ricco. The laminar generalized Stokes layer and turbulent drag reduction. *J. Fluid Mech.*, 667:135–157, 2011.

M. Quadrio and S. Sibilla. Numerical simulation of turbulent flow in a pipe oscillating around its axis. *J. Fluid Mech.*, 424:217–241, 2000.

M. Quadrio, P. Ricco, and C. Viotti. Streamwise-travelling waves of spanwise wall velocity for turbulent drag reduction. *J. Fluid Mech.*, 627:161–178, 2009.

P. Ricco and S. Hahn. Turbulent drag reduction through rotating discs. *J. Fluid Mech.*, 722:267–290, 2013.

P. Ricco and M. Quadrio. Wall-oscillation conditions for drag reduction in turbulent channel flow. *Int. J. Heat Fluid Flow*, 29:601–612, 2008.

A. Seifert and L. G. Pack. Active flow separation control on wall-mounted hump at high Reynolds numbers. *AIAA J.*, 40(7):1363–1372, 2002.

J. Shen. Hopf bifurcation of the unsteady regularized driven cavity flow. *J. Comp. Phys.*, 95(1):228–245, 1991.

B.L. Smith and A. Glezer. Vectoring and small-scale motions effected in free shear flows using synthetic jet actuators. *AIAA paper*, 657:213–241, 1997.

S. Taneda. Visualization of separating stokes flows. *J. Phys. Soc. Japan*, 46(6):1935–1942, 1979.

R. Temam. Remark on the pressure boundary condition for the projection method. *Theor. Comp. Fluid Dyn.*, 3(3):181–184, 1991.

R. Temam. *Navier-Stokes equations: theory and numerical analysis*, volume 343. American Mathematical Soc., 2001.

S.M. Trujillo, D.G. Bogard, and K.S. Ball. Turbulent boundary layer drag reduction using an oscillating wall. *AIAA Paper*, 97-1870, 1997.

C. Viotti, M. Quadrio, and P. Luchini. Streamwise oscillation of spanwise velocity at the wall of a channel for turbulent drag reduction. *Phys. Fluids*, 21(11), 2009.

M.J. Walsh. Turbulent boundary layer drag reduction using riblets. *AIAA Paper No.*, 82-0169, 1982.

M.J. Walsh. Riblets as a viscous drag reduction technique. *AIAA J.*, 21(4):485–486, 1983.

M.J. Walsh and L.M. Weinstein. Drag and heat-transfer characteristics of small longitudinally ribbed surfaces. *AIAA J.*, 17(7):770–771, 1979.

M.J. Walsh, W.L. Sellers III, and C.B. Mcginley. Riblet drag at flight conditions. *J. Aircraft*, 26(6):570–575, 1989.

D.J. Wise and P. Ricco. Turbulent drag reduction through oscillating discs. *J. Fluid Mech.*, 746:536–564, 2014.

D.J. Wise, C. Alvarenga, and P. Ricco. Spinning out of control: Wall turbulence over rotating discs. *Phys. Fluids*, 26(12):125107, 2014.

C. Wong and K. Kontis. Flow control by spanwise blowing on a naca 0012. *J. Aircraft*, 44(1):337–340, 2007.